Cell

Proteolethargy is a pathogenic mechanism in chronic disease

Graphical abstract

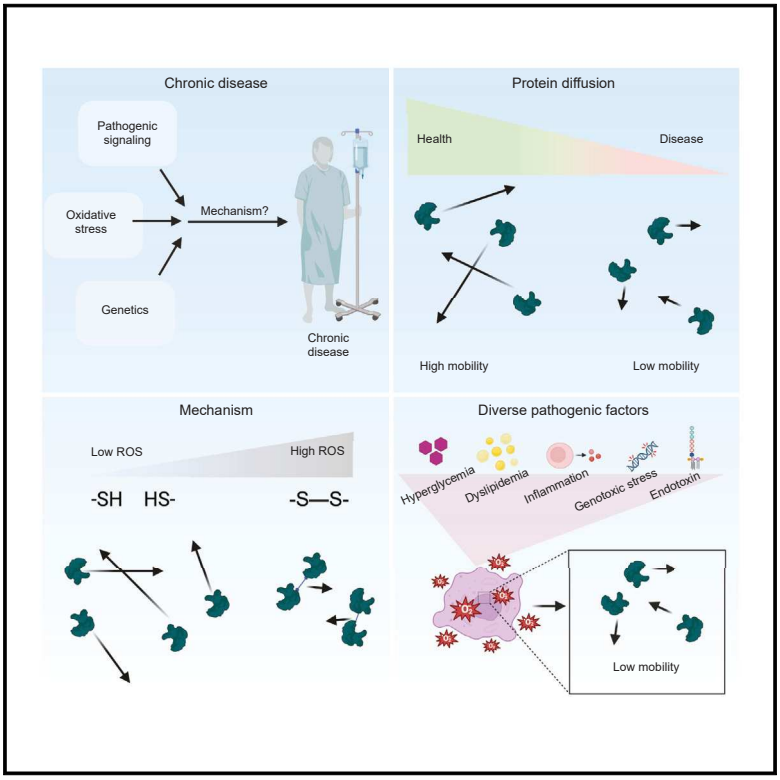

Highlights

- Pathogenic signaling leads to reduced mobility of proteins with diverse functions
- Reduced protein mobility (proteolethargy) is linked to dysregulated redox environments
- Diverse pathogenic stimuli associated with chronic diseases cause proteolethargy
- Proteolethargy may account for diverse cellular phenotypes seen in chronic diseases

Authors

Alessandra Dall'Agnese, Ming M. Zheng, Shannon Moreno, ..., Arup K. Chakraborty, Tong Ihn Lee, Richard A. Young

Correspondence

tlee@wi.mit.edu (T.I.L.), young@wi.mit.edu (R.A.Y.)

In brief

Pathogenic signaling leads to reduced mobility of proteins with diverse functions. This proteolethargy, which is due to increased oxidation of cysteine residues, may account for diverse cellular phenotypes seen in chronic diseases.

Dall'Agnese et al., 2025, Cell *188*, 207–221
January 9, 2025
https://doi.org/10.1016/j.cell.2024.10.051

CellPress

Cell

CellPress

Article

Proteolethargy is a pathogenic mechanism in chronic disease

Alessandra Dall'Agnese,[1,10] Ming M. Zheng,[1,2,10] Shannon Moreno,[1,3,10] Jesse M. Platt,[1,4] An T. Hoang,[1] Deepti Kannan,[2] Giuseppe Dall'Agnese,[1] Kalon J. Overholt,[1,5] Ido Sagi,[1] Nancy M. Hannett,[1] Hailey Erb,[1] Olivia Corradin,[1,3] Arup K. Chakraborty,[2,6,7,8,9] Tong Ihn Lee,[1,*] and Richard A. Young[1,3,11,*]

[1]Whitehead Institute for Biomedical Research, Cambridge, MA 02142, USA
[2]Department of Physics, Massachusetts Institute of Technology, Cambridge, MA 02139, USA
[3]Department of Biology, Massachusetts Institute of Technology, Cambridge, MA 02139, USA
[4]Division of Gastroenterology, Department of Medicine, Massachusetts General Hospital, Boston, MA 02114, USA
[5]Department of Biological Engineering, Massachusetts Institute of Technology, Cambridge, MA 02139, USA
[6]Department of Chemical Engineering, Massachusetts Institute of Technology, Cambridge, MA 02139, USA
[7]Department of Chemistry, Massachusetts Institute of Technology, Cambridge, MA 02139, USA
[8]Institute of Medical Engineering and Science, Massachusetts Institute of Technology, Cambridge, MA 02139, USA
[9]Ragon Institute of Massachusetts General Hospital, Massachusetts Institute of Technology and Harvard University, Cambridge, MA 02139, USA
[10]These authors contributed equally
[11]Lead contact
*Correspondence: tlee@wi.mit.edu (T.I.L.), young@wi.mit.edu (R.A.Y.)
https://doi.org/10.1016/j.cell.2024.10.051

SUMMARY

The pathogenic mechanisms of many diseases are well understood at the molecular level, but there are prevalent syndromes associated with pathogenic signaling, such as diabetes and chronic inflammation, where our understanding is more limited. Here, we report that pathogenic signaling suppresses the mobility of a spectrum of proteins that play essential roles in cellular functions known to be dysregulated in these chronic diseases. The reduced protein mobility, which we call proteolethargy, was linked to cysteine residues in the affected proteins and signaling-related increases in excess reactive oxygen species. Diverse pathogenic stimuli, including hyperglycemia, dyslipidemia, and inflammation, produce similar reduced protein mobility phenotypes. We propose that proteolethargy is an overlooked cellular mechanism that may account for various pathogenic features of diverse chronic diseases.

INTRODUCTION

Diseases associated with chronic or pathogenic signaling are a leading cause of morbidity and mortality.[1] For prevalent syndromes such as diabetes and inflammatory disorders, the pathology typically involves a continuous and/or high-level stimulus but not necessarily a known mutation in a specific gene.[2–7] In contrast with monogenic diseases, where the causal link between gene mutation and disease pathology is evident and the cellular pathways directly impacted are thus defined, in chronic syndromes, causal gene mutations are uncommon, and diverse cellular processes such as gene regulation, ribosome biosynthesis, and metabolic activity are dysregulated.[8–18] Thus, how to define hypotheses that will inform therapeutic development on the basis of such a breadth of cellular dysfunction has long vexed clinicians and research scientists.

The billions of protein molecules produced in cells must leave their site of synthesis and arrive at cellular locations where they carry out their specialized functions.[19–26] In so doing, they will transit through a milieu that is densely packed with biomolecules.[19–24,27] Recently, pathogenic signaling in certain chronic diseases was reported to cause reduced movement of receptor molecules into functional protein assemblies.[28–30] These findings led us to consider the possibility that dysregulated signaling might cause a more general defect in protein mobility in cells and that reduced protein mobility in and of itself might be a pathogenic mechanism shared across these diseases. Biochemical reactions are often collision limited,[31,32] and reduced rates of protein diffusion would therefore be expected to reduce functional outputs.

Here, we show that pathogenic signaling reduces the mobility of key proteins involved in diverse cellular processes and that this reduction in protein mobility, which we call proteolethargy, is associated with a dysregulated redox environment that consequently impacts oxidation-sensitive cysteines. Reduced protein mobility may account for the diversity of dysregulated cellular processes evident in chronic disease. We discuss a therapeutic hypothesis that emerges from these findings, which might prove

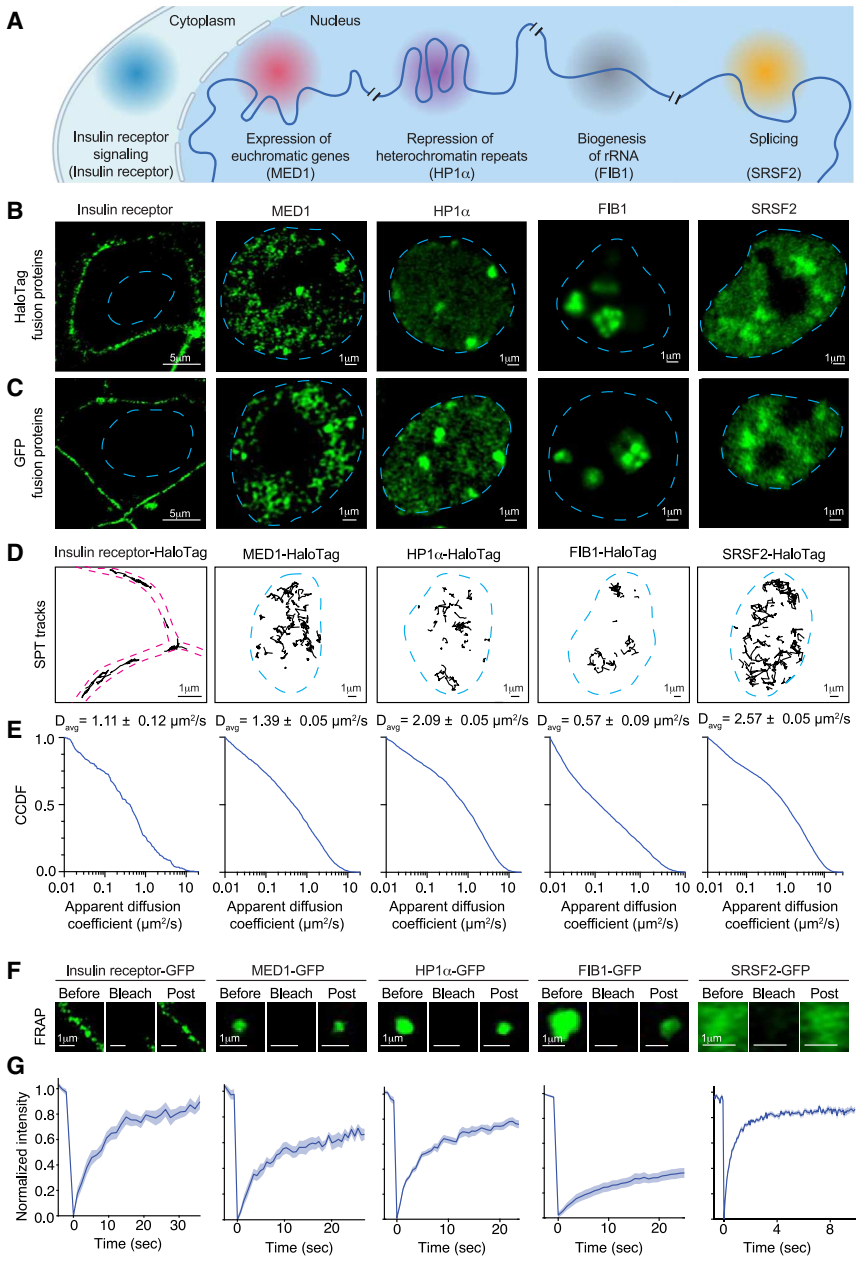

Figure 1. Mobility of diverse proteins in cells

(A) Cellular compartments, biological processes, and proteins examined in this study.

(B and C) Live-cell imaging of HepG2 cells expressing HaloTag (B) or green fluorescent protein (GFP)-tagged (C) versions of the indicated proteins. Dashed lines show outline of nucleus. Scale bars are indicated.

(D) Representative tracks for movement of individual molecules as determined by single-particle tracking (SPT) of HaloTag versions of the indicated proteins. Dashed magenta lines represent outline of the plasma membrane. Dashed blue lines represent outline of the nucleus. Scale bars are indicated.

(E) Complementary cumulative distribution function (CCDF) graphs of apparent diffusion coefficients, as determined by SPT, of the indicated proteins (n = 294, 1,751, 2,591, 2,855, and 5,458 molecules for insulin receptor (IR), MED1, HP1α, FIB1, and SRSF2, respectively).

(F) Representative images of FRAP of HepG2 cells expressing GFP-tagged versions of the indicated proteins. Images before (before), immediately following (bleach), and after recovery (post) are shown. Scale bars are indicated.

(G) Quantification of FRAP experiments of the indicated proteins (n = 10, 11, 15, 15, and 15 cells for IR, MED1, HP1α, FIB1, and SRSF2, respectively). Data shown as mean (blue line) ± standard error of the mean (SEM) (light blue).

See also Figures S1 and S2 and Table S1.

to be applicable in patients with diseases associated with proteolethargy.

RESULTS

Protein mobility in cells

We set out to develop a theoretical and experimental framework that would allow us to measure the mobility of multiple proteins with diverse functions in cells subjected to normal and pathogenic signaling. Single-particle tracking (SPT) and fluorescence recovery after photobleaching (FRAP) allow for the measurement of the kinetics of protein mobility in living cells, and proteins studied with these methods have been reported to have average apparent diffusion coefficients that vary between 0.01 and 30 μm^2/s.[25,26,33–37] This variation is thought to reflect that protein mobility is influenced by diverse factors, ranging from protein size to interaction with various biomolecules.[33] For our study, we selected proteins whose functions are key to cellular processes known to be dysregulated in prevalent syndromes[8–18]: a plasma membrane receptor (insulin receptor, IR), a transcriptional co-factor present at actively transcribed genes (mediator subunit MED1), a regulator of silent genes in heterochromatin (heterochromatin protein HP1α), a component of the nucleolus involved in ribosome biosynthesis (fibrillarin, FIB1) and a subunit of the mRNA splicing apparatus (serine and arginine-rich splicing factor 2, SRSF2) (Figure 1A; STAR Methods). As a cell model, we chose HepG2 cells as they provide a well-established model system representative of human liver cells in healthy and disease states.[28,38–40] To monitor the mobility of each of these proteins, we engineered HepG2 cells to encode the endogenous protein fused with HaloTag or monomeric enhanced green fluorescence protein (GFP) and validated that each fusion protein was produced at normal levels and migrated to the compartment where it is known to function (Figures 1B, 1C, and S1).

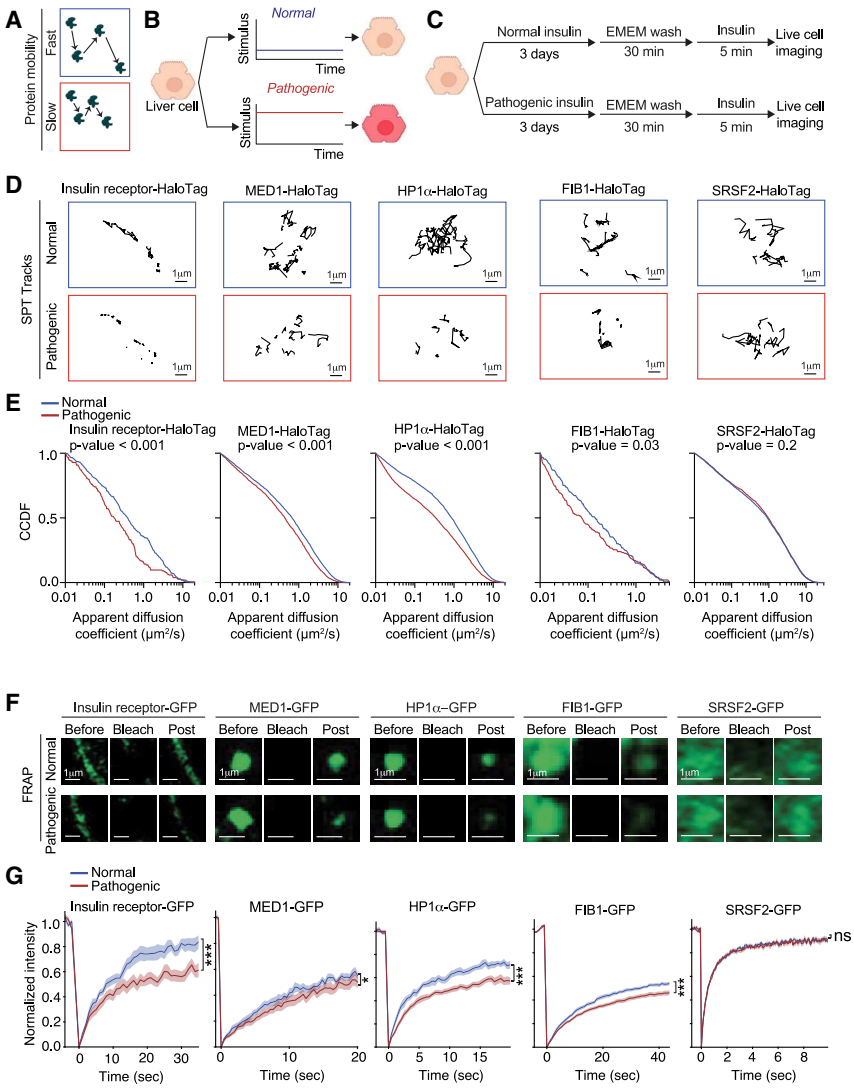

Figure 2. Protein mobility decreases in a model of pathogenic signaling

(A and B) Model for protein mobility in pathogenic signaling; individual molecules move at fast or slow speeds (A), depending on exposure to normal or pathogenic signaling (B).

(C) Schematic representation of cell treatments.

(D) Representative individual protein tracks as determined by SPT for the indicated proteins and experimental treatments. Scale bars are indicated.

(E) CCDF graphs of apparent diffusion coefficients, as determined by SPT, for the indicated proteins and experimental treatments (normal, n = 357, 5,719, 5,199, 153, and 3,399 molecules for IR, MED1, HP1α, FIB1, and SRSF2, respectively; pathogenic, n = 154, 2,227, 3,529, 146, and 2,872 molecules for IR MED1, HP1α, FIB1, and SRSF2, respectively). Mann-Whitney test was used for statistical analysis. p values are reported in the figure.

(F) Representative FRAP images for the indicated proteins and experimental treatments. Images before (before), immediately following (bleach), and after recovery (post) are shown. Scale bars are indicated.

(G) Quantification of FRAP experiments for the indicated proteins and experimental conditions (normal and pathogenic, n = 16, 10, 14, 10, and 20 cells each condition for IR, MED1, HP1α, FIB1, and SRSF2, respectively). Data shown as mean (normal, blue line; pathogenic, red line) ± SEM (normal, light blue; pathogenic, light red). t test was used for statistical analysis. Cohen's d = 0.9, 0.4, 1.2, 0.9, and 0.0 for IR, MED1, HP1α, FIB1, and SRSF2, respectively. * represents p value < 0.05 and *** represents p value < 0.001.

See also Figures S2, S3, and S4 and Tables S2 and S3.

We determined the apparent diffusion coefficients of IR, MED1, HP1α, FIB1, and SRSF2 by SPT, based on the mean-squared displacement of each individual protein molecule's trajectory. For each protein, we measured at least 200 protein trajectories and plotted the distribution of apparent diffusion coefficients (Figures 1D and 1E). As expected, most SPT protein trajectories for IR were contained within the plasma membrane and most SPT protein trajectories for MED1, HP1α, FIB1, and SRSF2 were contained within the nucleus (Figure 1D). The apparent diffusion coefficients ranged from 0.01 to 28 $\mu m^2/s$ (Figure 1E), consistent with diffusion coefficients determined for other human proteins (Table S1), with SRSF2 having the highest average mobility and FIB1 the lowest (Figures 1E and S2A).

We also used FRAP to measure the mobility of proteins in HepG2 cells engineered to express the endogenous protein fused to GFP. Specifically, we bleached a selected region in the cell with a focused laser beam and measured the rate at which the fluorescence intensity recovered at the photobleached region. This fluorescence recovery reflects the average mobility of the bulk population of fluorescent proteins.[41] For all proteins under study, the fluorescence intensity recovered on a timescale of seconds (Figures 1F and 1G), and the relative mobilities of the proteins were in line with those determined using SPT (Figure S2). The mobility of all the proteins measured in these studies was within the range determined previously for other proteins in living cells.[33–36,42–45]

Reduced protein mobility with pathogenic signaling

As an initial test of the hypothesis that protein mobility might be affected in a chronic disease (Figure 2A), we selected insulin signaling, since it is dysregulated in prevalent syndromes such as diabetes, known to be characterized by a range of affected cellular processes, including dysregulated intracellular signaling, gene activity, RNA splicing, and ribosome biosynthesis, among others.[5–12] In fasting healthy individuals, liver cells are normally exposed to low concentrations of insulin (~0.1 nM), whereas after a meal, insulin transiently increases and activates the insulin signaling pathway.[28,46,47] In fasting patients with insulin resistance, liver cells are subject to continuous high concentrations of insulin (~3 nM), and this chronic high level of insulin no longer fully activates the signaling response.[28,46,47] Thus, normal

and pathogenic insulin signaling can be modeled in cell culture by treating liver-derived cells with normal or elevated (pathogenic) concentrations of insulin for prolonged periods of time (Figure 2B).[28,48]

To test the possibility that pathogenic insulin signaling may alter protein mobility, we treated HepG2 cells with normal or pathogenic concentrations of insulin (Figure 2C). SPT analysis revealed that the mobility of IR, MED1, HP1α, and FIB1 was reduced in cells that were treated with pathogenic levels of insulin, whereas that of SRSF2 was unaffected (Figures 2D, 2E, and S2K; Table S2). For example, 50% of IR molecules had an apparent diffusion coefficient greater or equal to 0.4 $\mu m^2/s$ when cells were treated with normal concentrations of insulin, and this percentage decreased by ~20% when cells were treated with pathogenic insulin concentrations (Figures 2D and 2E). FRAP analysis of these proteins indicated a similar effect on this set of proteins; there was a reduction in the recovery of all proteins except SRSF2 (Figures 2F and 2G; Table S3). Taken together, these results suggest that pathogenic insulin signaling leads to a reduction in the mobility of many proteins in cells.

The proteins studied here have been reported to be associated with biomolecular condensates,[28,44,49–52] which are non-stoichiometric assemblies of proteins that share cellular functions.[25,44,53–55] We thus tested whether suppressed protein mobility occurs when proteins are resident within the dense phase of condensates or when they are outside these bodies, using FRAP with the GFP-tagged proteins. For the proteins that could be reliably assigned to be within or outside of condensates during image acquisition (MED1, HP1α, FIB1, and SRSF2), pathogenic signaling was found to produce a similar reduction in mobility for MED1, HP1α, and FIB1, while SRSF2 mobility was unaffected (Figures 2G and S3A; Table S3). Rapid movement of IR condensates prevented reliable assignments. Pathogenic signaling had little effect on condensate number, size, or partition ratio for these proteins, except for a slight decrease in condensate number for IR, as observed previously[28] (Figure S3B). Although there are reports that reactive oxygen species (ROS) can influence the properties of some condensates,[56–58] these results suggest that the effects of pathogenic signaling can produce changes in protein mobility while having a limited impact on condensate properties under the conditions studied here.

Oxidative environment affects protein mobility

Given the broad range of proteins whose mobility was affected by pathogenic insulin signaling, we asked whether changes in cellular viscosity or in the chemical environment might be responsible for the observed changes in protein mobility. To test the effect of pathogenic signaling on cellular viscosity, we monitored the mobility of GFP (not fused to any other protein) by FRAP, which is an established method for such studies,[31,59–61] and the mobility of HaloTag (not fused to any other protein) by SPT. We detected a change in cytoplasmic viscosity but no change in nuclear viscosity (Figures S4A and S4B). These results suggest that altered viscosity could contribute to the mobility phenotype for IR in the plasma membrane but is unlikely to significantly impact the diverse nuclear proteins studied here.

Substantial changes in the chemical environment are known features of chronic diseases such as insulin resistance due to high levels of ROS (Figures 3A and 3B).[28,62] Here, we hypothesize that if an oxidative environment leads to changes in protein mobility, then treating cells with pathologically relevant concentrations of the oxidizing agent H_2O_2 should phenocopy the effects observed in cells treated with pathogenic insulin signaling (Figures 3B and 3C). Indeed, FRAP analysis showed that treatment of cells with H_2O_2 caused reduced mobility of IR, MED1, HP1α, and FIB1 but not of SRSF2 or nuclear GFP (Figures 3D–3F, S4C, and S4D; Table S3).

If high levels of ROS lead to reductions in protein mobility, then treatment with the antioxidant N-acetyl cysteine (NAC) should restore some degree of protein mobility in cells exposed to pathogenic levels of insulin. As expected, FRAP revealed that treating insulin-resistant cells with 1 mM NAC partially rescued the mobility of IR, MED1, HP1α, and FIB1, but it had little effect on the mobility of SRSF2 and nuclear GFP (Figures 3G–3I, S4D, and S4E; Table S3). These results are consistent with the possibility that elevated levels of ROS cause a decrease in the mobility of certain proteins and suggest that the change in protein behavior is caused by an alteration in the oxidative environment.

Mobility of proteins with exposed cysteines

The sensitivity of proteins to the oxidative environment suggests that oxidation-sensitive amino acids might influence protein mobility. When we analyzed amino acid content, we found that the proteins whose mobility was affected by pathogenic insulin signaling and H_2O_2 have cysteines with surface-exposed side chains, whereas this was not the case for the proteins whose mobility was not affected by these pathogenic factors (Figure 4A; Table S4). Surface cysteines create the potential for crosslinking through disulfide bonds, which might reduce the rate of diffusion by diverse mechanisms, including increasing effective protein mass, altering protein conformation, promoting binding to immobile proteins, altering interaction with transporters, and increasing cellular viscosity (Figure 4B).[63–67]

To explore how different oxidative states of the cellular environment might be expected to influence diffusion of proteins with and without cysteines, we developed a physics-based model (Figures 4C and S5; see STAR Methods). In this model, proteins are simulated as spherical particles, half of which have sticky patches on their surfaces, representing surface-exposed cysteine residues, and half of which do not have sticky patches. As the oxidative state of the cellular environment increases, the propensity of interaction between the patches increases, leading to protein crosslinking and formation of protein dimers and multimers (Figure S5). Proteins without surface-exposed cysteines remain in a monomeric state even at higher levels of ROS. As a result, the average diffusion coefficient of proteins containing surface-exposed cysteine decreased more than that of proteins lacking surface-exposed cysteines, owing to dimer and multimer formation (Figures 4C and S5). The mobility of proteins lacking cysteines slightly decreased at higher levels of ROS, due to the increase in effective viscosity caused by the crosslinking of the proteins containing cysteines present in the environment (Figure 4C). This model predicts that increased ROS-driven intermolecular disulfide bond formation will reduce protein mobility due to the increased frequency and lifetime of these bonds. As an initial test of this

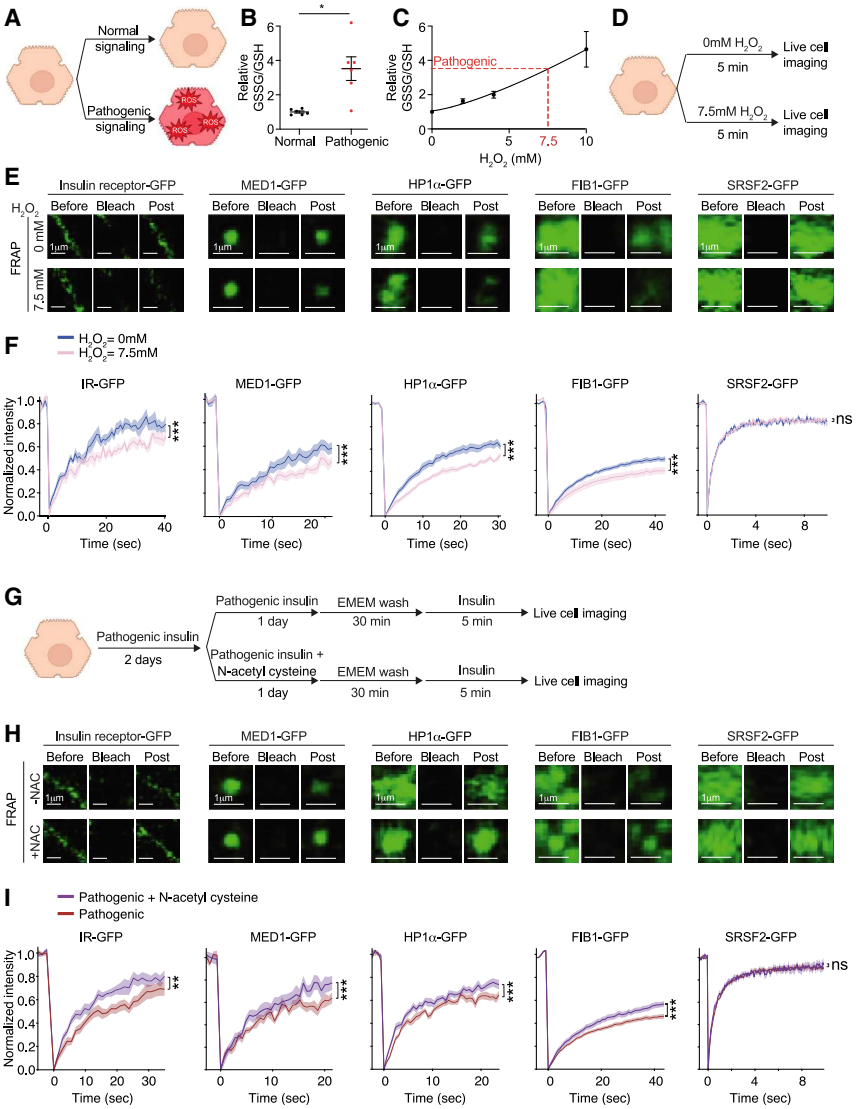

Figure 3. Oxidative environment affects protein mobility

(A) Increased reactive oxygen species (ROS) in pathogenic signaling.

(B) Relative ratio of oxidized to reduced glutathione (GSSG/GSH) in cells treated as indicated. Data shown as mean ± SEM. t test was used for statistical analysis. * represents p value < 0.05.

(C) Relative GSSG/GSH ratio in cells treated with different hydrogen peroxide (H_2O_2) concentrations. Data shown as mean ± SEM. H_2O_2 concentration expected to phenocopy pathogenic signaling is indicated.

(D and G) Schematic representation of cell treatments.

(E and H) Representative FRAP images for the indicated proteins and experimental treatments. Images before (before), immediately following (bleach), and after recovery (post) are shown. Scale bars are indicated.

(F and I) Quantification of FRAP experiments for the indicated proteins and experimental conditions. For (F), 0 and 7.5 mM, n = 10 cells each condition for each protein. Data shown as mean (0 mM, blue line; 7.5 mM, red line) ± SEM (0 mM, light blue; 7.5 mM, light red). For (I), (pathogenic, n = 16, 10, 15, 10, and 20 for IR, MED1, HP1α, FIB1, and SRSF2, respectively; pathogenic + NAC, n = 16, 10, 15, 20, and 20 for IR, MED1, HP1α, FIB1, and SRSF2, respectively. Data shown as mean (pathogenic, red line; pathogenic + NAC, purple line) ± SEM (pathogenic, light red; pathogenic + NAC, light purple). t test was used for statistical analysis (F and I). For (F), Cohen's d = 0.7, 0.7, 1.2, 1.0, and 0.0 for IR, MED1, HP1α, FIB1, and SRSF2, respectively. For (I), Cohen's d = 0.5, 0.8, 0.9, 0.6, and 0.2 for IR, MED1, HP1α, FIB1, and SRSF2, respectively. ** represents p value < 0.01 and *** represents p value < 0.001.

See also Figure S4 and Table S3.

model, we investigated whether treatment of cells with H_2O_2 promotes crosslinking of IR proteins, using western blotting (Figure S6A). These results suggest enhanced formation of intermolecular crosslinking through disulfide bond formation and are consistent with the predictions from the theoretical work.

To further test the model that surface cysteines contribute to reduced protein mobility in an oxidative environment, we asked whether treatment with a thiol-protective agents might preserve protein mobility in a high ROS environment. To prevent cysteine disulfide bond formation, cells were treated with N-ethylmaleimide (NEM), a compound that forms stable, covalent bonds with the thiol group in cysteines. FRAP revealed that treating cells with NEM partially preserved the mobility of IR, MED1, HP1α, and FIB1, but it had little effect on the mobility of SRSF2 in the high ROS condition generated by H_2O_2 (Figure 4D).

If surface cysteines contribute to reduced protein mobility, we might expect that addition of surface cysteines to SRSF2, which normally lacks these residues, would cause reduced mobility of the modified SRSF2 protein in a high ROS environment. We engineered HepG2 cells to express endogenous SRSF2 fused to a rigid linker (to ensure surface exposure) containing multiple cysteine residues (SRSF2-Cys) or, as a control, the same number of serine residues (SRSF2-Ser) (Figures 4E and 4F). Treating HepG2 cells with H_2O_2 or pathogenic insulin concentrations did not affect the mobility of the SRSF2-Ser protein, but it decreased the mobility of SRSF2-Cys protein (Figures 4E and 4F). Taken together, these results indicate that surface-exposed cysteines can affect protein mobility when cells are exposed to oxidative stress and pathogenic signaling.

Next, we asked whether there are reports of any of the proteins studied here having missense mutations resulting in gaining a cysteine and, if so, whether these might affect protein mobility. A tyrosine-to-cysteine mutation (Y1361C) was reported in the IR. This mutation occurs outside of the structured domain and does not appear to decrease protein stability.[68] Modeling indicates that the cysteine gained through this mutation is surface exposed (Figure S6B). We introduced this mutation into the IR-GFP fusion protein (IR Y1361C-GFP) in both alleles in HepG2 cells (Figure 4G). By performing FRAP, we found that

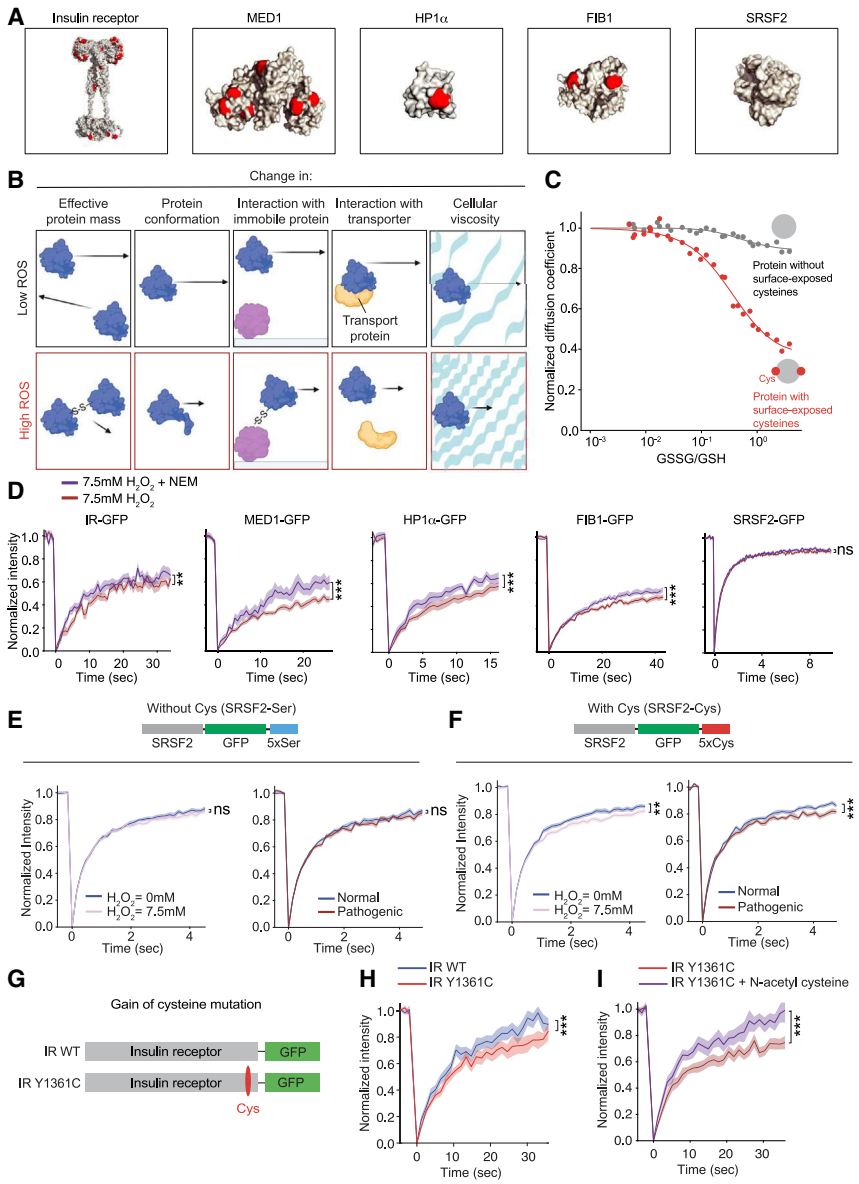

Figure 4. Surface-exposed cysteines sensitize proteins to oxidation-driven decrease in protein mobility

(A) Rendering of the crystal structure of indicated proteins showing cysteines in red.

(B) Diverse models for decreased protein mobility, including change in effective protein mass, protein conformation, interaction with immobile protein, interaction with a protein that facilitates transport, and cellular viscosity increasing resistance to movement.

(C) Predicted normalized diffusion coefficient from simulations of a mixture of proteins with (red) and without (gray) surface-exposed cysteines as a function of the ratio of oxidized (GSSG) to reduced (GSH) glutathione. The diffusion coefficient was normalized to the mean of all simulated data points for GSSG/GSH < 10^{-3} (see STAR Methods).

(D) Quantification of FRAP data for insulin receptor (7.5 mM H_2O_2, n = 16 cells; 7.5 mM H_2O_2 + N-ethylmaleimide [NEM], n = 16 cells), MED1 (7.5 mM H_2O_2, n = 29 cells; 7.5 mM H_2O_2 + NEM, n = 15 cells), HP1α (7.5 mM H_2O_2, n = 14 cells; 7.5 mM H_2O_2 + NEM, n = 13 cells), FIB1 (7.5 mM H_2O_2, n = 24 cells; 7.5 mM H_2O_2 + NEM, n = 24 cells), and SRSF2 (7.5 mM H_2O_2, n = 12 cells; 7.5 mM H_2O_2 + NEM, n = 12 cells) in HepG2 cells treated with 0 or 7.5 mM of H_2O_2 after pre-treatment with 10 μM NEM. Data are plotted as means ± SEM. ** represents p value < 0.01 and *** represents p value < 0.001.

(E and F) Top: representation of SRSF2 fusion proteins with an added serine- or cysteine-containing rigid linker. Bottom: quantification of FRAP data for SRSF2 fusion proteins in cells treated with the indicated experimental conditions (SRSF2-Ser, 0 mM H_2O_2, n = 13 cells, 7.5 mM H_2O_2, n = 12, normal, n = 10 cells, pathogenic, n = 10 cells; SRSF2-Cys, 0 mM H_2O_2, n = 13 cells, 7.5 mM H_2O_2, n = 13, normal, n = 10 cells, pathogenic, n = 10 cells). Data are plotted as mean ± SEM. ** represents p value < 0.01 and *** represents p value < 0.001.

(G) Representation of wild-type (WT) and mutant IR fusion proteins.

(H) Quantification of FRAP data for WT (IR WT, n = 15 cells) or Y1361C mutant IR (IR Y1361C, n = 15 cells). Data are plotted as mean ± SEM. *** represents p value < 0.001.

(I) Quantification of FRAP data for Y1361C mutant IR in cells treated with (n = 15 cells) or without (n = 15 cells) N-acetyl cysteine. Data are plotted as mean ± SEM. t test was used for statistical analysis (D–I). *** represents p value < 0.001.

See also Figures S5 and S6 and Table S4.

the gain-of-cysteine mutation caused a reduction in IR protein mobility in HepG2 cells under normal redox conditions (Figure 4H) and that treating cells expressing IR Y1361C-GFP with NAC enhanced IR Y1361C protein mobility (Figure 4I). Mutating the same amino acid to serine had little to no effect on IR protein mobility (Figure S6C). These results indicate that mutations that add surface cysteines sensitize the IR to physiological levels of ROS, reducing its mobility under normal redox conditions, and that addition of an antioxidant can enhance this receptor's mobility. It is possible that the Y1361C mutation confers this special sensitivity to normal redox conditions because it occurs in a region known to interact with other proteins containing surface-exposed cysteines.[69] Gain-of-cysteine mutations are among the most pathogenic missense mutations (Figure S6D), and their effect on protein mobility may not be limited to IR, but it may extend to other disease-relevant proteins.

Diverse pathogenic factors decrease protein mobility

The pathogenic stimuli that are associated with diverse diseases are thought to commonly induce oxidative stress.[70] We developed a mobility biosensor assay to investigate relationships between surface-exposed cysteines and protein mobility under oxidative conditions and to investigate whether diverse pathogenic stimuli produce similar mobility phenotypes in liver cells and in other disease-relevant cell types. We constructed the protein mobility sensor by adding a rigid linker containing

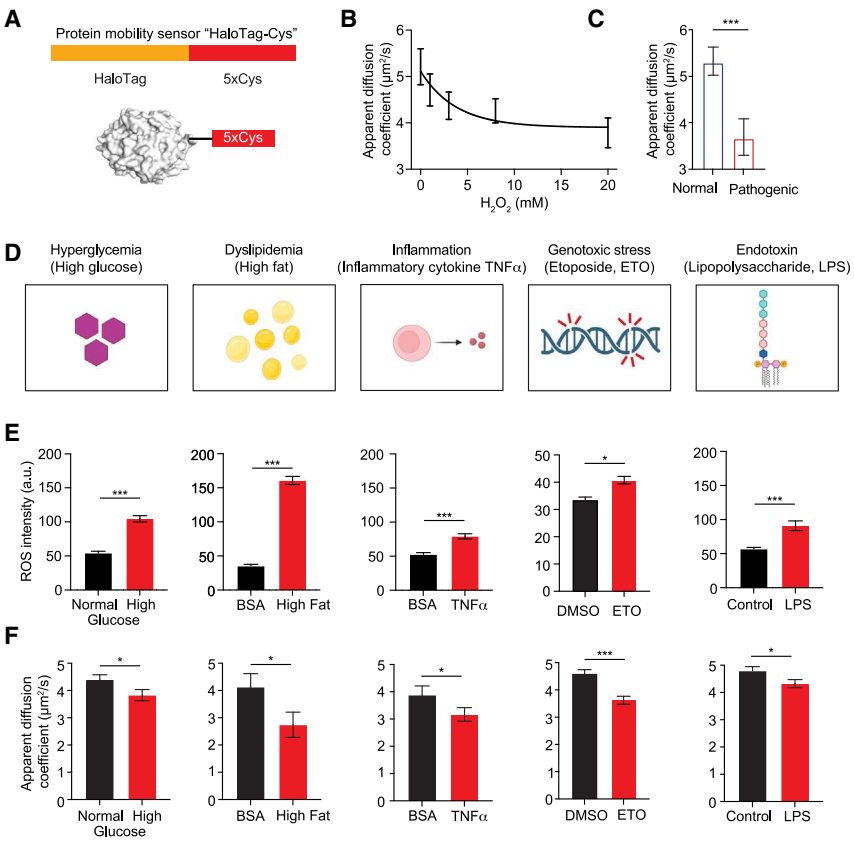

Figure 5. Diverse pathogenic factors decrease protein mobility

(A) Representations of HaloTag fusion protein (HaloTag-Cys).

(B) Apparent diffusion coefficient of HaloTag-Cys as determined by SPT in cells treated as indicated (n = 245, 316, 428, 560, and 305 molecules for 0, 1, 3, 8, and 20 mM H_2O_2, respectively).

(C) Apparent diffusion coefficient of HaloTag-Cys as determined by SPT in cells treated as indicated (n = 446 and 173 molecules for normal and pathogenic, respectively). Data are plotted as means ± SEM. Mann-Whitney test was used for statistical analysis. *** represents p value < 0.001.

(D) Cartoon depicting pathogenic stimuli.

(E) ROS quantification in cells treated as indicated. Data are plotted as mean ± SEM. Numbers of cells: normal glucose (77) vs. high glucose (67); BSA (115) vs. high fat (171); BSA (150) vs. TNF-α (91); DMSO (152) vs. etoposide (ETO, 83); control (82) vs. lipopolysaccharide (LPS, 78). t test was used for statistical analysis. * represents p value < 0.05 and *** represents p value < 0.001.

(F) Apparent diffusion coefficient of HaloTag-Cys as determined by SPT in cells treated as indicated. Numbers of molecules: normal glucose (1,001) vs. high glucose (582); BSA (126) vs. high fat (101); BSA (265) vs. TNF-α (363); DMSO (1,718) vs. ETO (1,804); control (1,456) vs. LPS (1,327). Cohen's d = 0.1, 0.2, 0.1, 0.2, and 0.1 for hyperglycemia, dyslipidemia, inflammation, genotoxic stress, and endotoxin, respectively. Data are plotted as means ± SEM. Mann-Whitney test was used for statistical analysis. * represents p value < 0.05 and *** represents p value < 0.001.

See also Figure S7.

five cysteine residues to the HaloTag protein (HaloTag-Cys) (Figure 5A) together with a control biosensor containing five serine residues (HaloTag-Ser). The HaloTag-Cys biosensor was appropriately sensitive to pathogenic levels of H_2O_2, as evidenced by the mobility of HaloTag-Cys decreasing upon H_2O_2 treatment in a dose-dependent fashion (Figure 5B). Similarly, treatment of cells containing the biosensor with pathogenic insulin concentrations led to reduced protein mobility (Figure 5C). Pathogenic levels of insulin had less of an effect on the mobility of a control HaloTag-Ser protein (Figure S6E).

Pathogenic stimuli that induce oxidative stress include hyperglycemia, high fat, inflammation, genotoxic stress, endotoxin, and drug toxicity (Figure 5D).[71–76] These stimuli have been shown to increase ROS through diverse mechanisms, which include, but are not limited to, dysregulation of mitochondria, dysregulation of redox homeostasis proteins, ER stress, and eNOS dysregulation.[75,77–83] Treating cells with these pathogenic stimuli led to elevated levels of ROS (Figure 5E), confirming previous results.[28,71–75] These treatments also reduced the mobility of the HaloTag-Cys protein (Figures 5F, S7A, and S7B). In skeletal muscle cells, another disease-relevant cell type, pathogenic stimuli also decreased HaloTag-Cys mobility (Figure S7C). Taken together, these results are consistent with a model in which diverse pathogenic stimuli known to induce oxidative stress cause suppressed protein mobility in multiple disease-relevant cell types.

Protein mobility and functional activity

Biochemical reactions are typically collision limited,[31,32] and reduced rates of protein diffusion would be expected to reduce functional outputs (Figure 6A). We produced a mathematical model and conducted tests *in vitro* and in cells designed to confirm that reduced protein mobility confers reduced enzymatic activity with the IR (Figure 6B). Phosphorylation of substrates by protein kinases such as the IR (Figure 6C), which would be expected to be collision limited, should be reduced when protein mobility is decreased. Mathematical modeling of phosphorylation of substrates by protein kinases showed that reaction outputs are reduced when protein mobility is decreased (Figure 6D). IR and an IR substrate protein, IRS1, were purified and subjected to environments that would slow or accelerate the mobility of proteins *in vitro*. When the mobility of proteins was reduced *in vitro* by increasing glycerol concentration, and thus viscosity, we observed reduced phosphorylation of IRS1 by IR (Figure 6E). Agitation of solutions can increase protein mobility and thus the collision rate of molecules,[84] and agitation was found to partially rescue the reduction in phosphorylation with elevated viscosity (Figure 6F). These results support the expectation that reduced protein mobility reduces the kinase activity of IR.

To further probe the relationship between protein mobility and functional output in cells, we used the BirA/AviTag system, which was previously shown to exhibit collision-limited activity.[31] In this system, where the biotin ligase BirA biotinylates its substrate

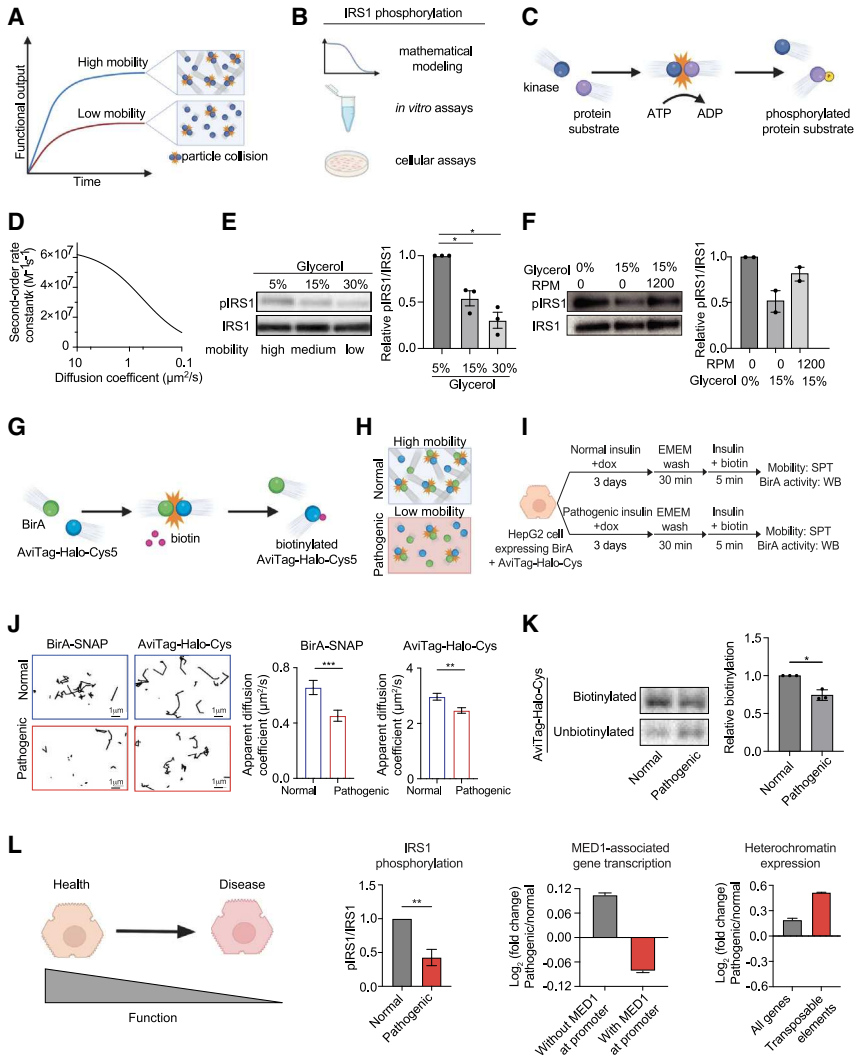

Figure 6. Protein mobility affects function

(A–C) Cartoons depicting relationship between protein mobility, functional output, and collision frequency (A), models and assays used to study IRS phosphorylation (B), and the phosphorylation of IRS1 by a kinase (C).

(D) Second-order rate constant from simulations of IRS1 phosphorylation as a function of diffusion coefficient.

(E) Immunoblot for phosphorylated IRS1 (pIRS1) and IRS1 (left). IRS1 phosphorylation assay was performed in solutions containing 5%, 15%, or 30% glycerol. Quantification of relative pIRS1 amount (right) (n = 3 biological replicates). t test was used for statistical analysis. * represents p value < 0.05.

(F) Immunoblot for phosphorylated IRS1 (pIRS1) and IRS1 (left). IRS1 phosphorylation assay was performed in solutions containing 0% or 15% glycerol with agitation (1,200 rpm) or without agitation (0 RPM). Quantification of relative pIRS1 amount (right) (n = 2 biological replicates).

(G) Cartoon depicting biotinylation assay.

(H) Cartoon depicting high mobility in normal conditions and low mobility in pathogenic conditions.

(I) Schematic representation of cell treatments.

(J) Representative tracks for movement of individual molecules as determined by SPT of the indicated proteins (left). Scale bars are indicated. Apparent diffusion coefficient of the indicated proteins in cells treated with normal or pathogenic insulin (right). Numbers of molecules: BirA-SNAP normal (1,003) vs. pathogenic (865); AviTag-Halo-Cys normal (1,022) vs. pathogenic (1,067). Mann-Whitney test was used for statistical analysis. ** represents p value < 0.01 and *** represents p value < 0.001.

(K) Immunoblot for biotinylated and unbiotinylated AviTag-Halo-Cys. t test was used for statistical analysis. * represents p value < 0.05.

(L) Cartoon depicting function decreases in diseased cells (left). Quantification of relative pIRS1 determined by immunoblotting (t test was used for statistical analysis, ** represents p value < 0.05), $\log_2$(fold change) of gene expression for genes whose promoter is occupied or not occupied by MED1, and $\log_2$(fold change) of expression of protein-coding genes or repetitive elements.

See also Figure S7.

AviTag, fusion of BirA with SNAP-tag (BirA-SNAP) and fusion of the AviTag to our protein mobility biosensor HaloTag-Cys allowed us to monitor both protein mobility and BirA activity (Figures 6G and 6H) in HepG2 cells. Under conditions of pathogenic signaling in cells, the reduction in protein mobility correlated with reduced biotinylation (Figures 6I–6K). These results support the concept that reduced protein mobility leads to reduced functional activity.

The cellular processes that have been reported to be dysregulated in chronic syndromes include reduced phosphorylation of substrates, altered gene regulation, and repression of heterochromatic repeats, among others.[8–18] To confirm that these processes are indeed dysregulated in cells under the conditions studied here, we conducted assays in cells that were treated with normal and with pathogenic insulin. The results showed evidence of dysregulated features noted previously in chronic syndromes (Figures 6L and S7D). Phosphorylation of IRS1 was reduced, genes occupied by the mediator coactivator subunit MED1 were expressed at lower levels, and there was elevated expression of heterochromatic repeats. These results are consistent with a model where reduced protein mobility can contribute to the diversity of dysregulated processes that are evident in chronic disease.

DISCUSSION

Pathogenic signaling contributes to prevalent diseases characterized by dysregulation of remarkably diverse cellular processes.[8–17] Consequently, equally diverse pathogenic mechanisms are assumed to cause these phenotypes. However, the findings on protein mobility in healthy and dysregulated cells described here suggest an alternative explanation, namely,

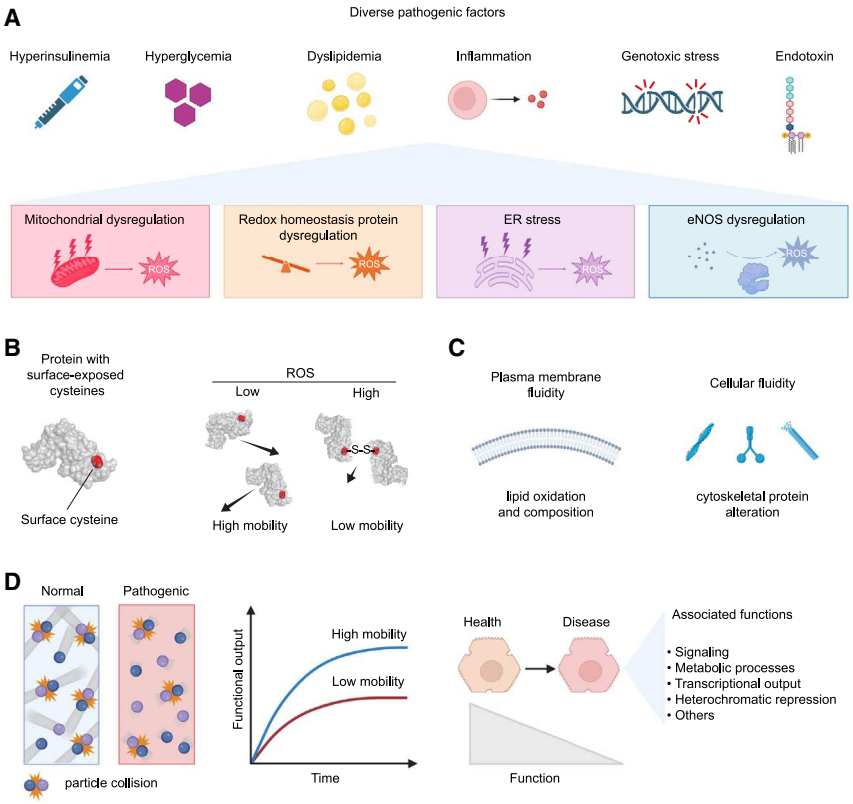

Figure 7. Proteolethargy is a pathogenic mechanism in chronic disease

(A) Diverse pathogenic factors lead to oxidative stress via multiple cellular pathways and mechanisms.

(B) Proteins with surface-exposed cysteines suffer reduced mobility in high ROS environments due to their sensitivity to oxidation.

(C) Alterations in plasma membrane and cytoplasmic fluidity can also occur in high ROS environments.

(D) Mobility is decreased in pathogenic signaling, thereby reducing rates of particle collision and leading to reduced functional output for diverse cellular processes.

that a common mechanism—suppressed mobility, here referred to as proteolethargy—contributes to dysregulation of a range of cellular processes in the setting of diverse pathogenic stimuli.

Proteolethargy, the phenomenon of reduced protein mobility in the setting of pathogenic stimuli, might be caused by any number of mechanisms, but several lines of evidence converge on the effects of excess ROS on protein mobility as a common mechanism that can impact proteins throughout the cell in diverse chronic syndromes (Figure 7). Cells exposed to diverse pathogenic stimuli produce excess ROS through mechanisms that include dysregulation of mitochondria, dysregulation of redox homeostasis proteins, ER stress, and eNOS dysregulation, among others (Figure 7A).[75,77–83] Proteins exposed to oxidative environments exhibit reduced mobility if they have surface-exposed cysteines or are engineered to have surface cysteines. These effects can be remedied in part by treatment of cells with reducing agents or agents that are thiol protective. Gain-of-cysteine mutations can cause reduced mobility of the mutated protein. We estimate that ~50% of human proteins contain at least one surface-exposed cysteine (see STAR Methods), so there is potential for half of the proteome to be directly susceptible to proteolethargy in high ROS environments.

Our experimental and modeling data jointly support a model in which proteins with surface-exposed cysteines, upon transiting through a milieu that is densely packed with biomolecules, have the potential to form transient disulfide crosslinks with other proteins (Figure 7B). An elevated oxidative environment has the potential to increase the lifetime of the intermolecular crosslinks,[63,85,86] effectively increasing the hydrodynamic radius and thereby decreasing protein mobility.[64] Variations of this model are possible, where changes in disulfide bond rates or lifetimes have additional influences on protein mobility through improper complex formation, changing protein conformation, promoting binding to immobile proteins, disrupting associations with transport proteins, or altering cytoplasmic viscosity (Figure 4B).[63–67] It is also likely that the effects of elevated oxidative environments can impact protein mobility more indirectly; for example, changes in plasma membrane fluidity due to altered lipid oxidation and composition have the potential to influence protein mobility,[87–93] and changes that affect cytoskeleton-associated proteins have been noted to impact cellular fluidity (Figure 7C).[94,95]

Proteolethargy would be expected to adversely impact diverse functions in cells. In healthy cells, proteins with prominent roles in diverse cellular processes are highly mobile and thus able to transit a space equivalent to the diameter of a cell in 2–10 s. In cells subjected to pathogenic signaling, however, the mobility of most proteins studied here was reduced by 20%–35%. Since many biological processes in cells are collision limited, decreases in protein mobility are expected to reduce functional outputs (Figure 7D).[31,32,96] Supporting this view, we found that reducing the mobility of IR reduces its rate of phosphorylation of the IR substrate IRS1 *in vitro* and *in vivo* and that a synthetic system designed to report biotin ligase activity in cells showed reduced ligase activity when cells were subjected to pathogenic signaling. The cellular processes that have been reported to be dysregulated in chronic syndromes such as diabetes and inflammatory disorders are diverse and include signaling activity, gene regulation, heterochromatin repression, and metabolic activity.[8–17] These cellular functions were found to be dysregulated in the cell system studied here. We thus suggest that proteolethargy may account for the diversity of dysregulated cellular functions noted for at least some chronic diseases.

Many proteins have been shown to assemble together with functionally related proteins into biomolecular condensates,

cellular organelles that are not physically delimited by membranes.[25,28,44,49–55,97,98] We found that the mobility of proteins was reduced both inside and outside of these compartments. The mobility of the synthetic proteins such as the protein mobility biosensor, which does not appear to assemble into condensates, was reduced by high ROS environments. Our results thus indicate that proteolethargy can occur across the cell, and it occurs both inside and outside of condensate compartments.

There is limited information on the mobility of a range of proteins with diverse functions in human cells and even less information on the effects of pathogenic stimuli on protein mobility. This paucity of knowledge may explain why proteolethargy has apparently not been described as a pathogenic mechanism in chronic diseases. Previous studies have investigated the diffusive behaviors of certain transcriptional regulators in mammalian cells,[24,35,99,100] and one noted that the mobility of the IR is reduced in rat hippocampal neurons by low concentrations of tumor necrosis factor alpha and by cholesterol depletion.[34]

The model described here for proteolethargy in disease has implications for the development of therapeutics for certain chronic diseases. Restoring protein mobility might be considered among the therapeutic hypotheses for these chronic diseases. Protein mobility biosensors, such as the one developed for this study, may prove to be valuable for high-throughput screening for drugs that restore normal protein mobility under pathogenic signaling conditions. Redox homeostasis is regulated by many pathways and proteins, which counteract transient increases in ROS that occur normally in diverse cellular processes,[70,101,102] so it is possible that therapeutic targeting of these natural pathways will prove beneficial for treating or preventing proteolethargy. The rescue of protein mobility with NAC treatment, as described here, is a proof of principle for this concept.

Limitations of the study

We propose that pathogenic signaling reduces the mobility of a large fraction of cellular proteins, that reduced protein mobility is due largely to a dysregulated redox environment that impacts oxidation-sensitive cysteines, and that this proteolethargy may account for the diversity of dysregulated cellular processes that are evident in chronic disease. Pathogenic signaling could potentially affect ~50% of the proteome, based on estimates of surface-exposed cysteines in proteins, but a necessarily limited number of proteins are surveyed in this work. There are additional oxidation-sensitive amino acids and oxidation-related mechanisms that may contribute to decreased protein mobility, which are not studied here. As this work is focusing on the movement of individual molecules at specific timescales and distance scales, we did not explicitly examine all potential mechanisms that may affect protein movement. Proteolethargy in the setting of pathogenic stimuli was observed using cell lines and a defined set of experimentally tractable treatments, so further studies will be needed to learn how reduced protein mobility manifests as disease phenotypes in whole organisms. Diverse endogenous proteins were studied in cells subjected to pathogenic insulin signaling, but these proteins were not studied in response to diverse pathogenic stimuli, where a biosensor was deployed to report protein mobility. Excess ROS has been implicated in aging and diseases not studied here, so further studies are necessary to learn whether reduced protein mobility is associated with, and perhaps contributes to, aging and other diseases.

RESOURCE AVAILABILITY

Lead contact

Further information and requests for resources and reagents should be directed to and will be fulfilled by the lead contact, Richard Young (young@wi.mit.edu).

Materials availability

All plasmids and cell lines generated in this study are available upon request.

Data and code availability

Metabolomic datasets generated in this study have been deposited in Metabolights: MTBLS9535. RNA-seq datasets generated in this study have been deposited in GEO: GSE273733. Published MED1 ChIP-seq data (GEO: GSM2040029) and input (GEO: GSM2864933) were used in this study. The code for Brownian dynamics simulations of proteins with surface-exposed cysteines has been deposited in GitHub: https://github.com/younglab/proteolethargy. All other codes are available to researchers via the corresponding authors.

ACKNOWLEDGMENTS

We thank Phillip Sharp, Eric Olson, Christine Ivashchenko, Max Friesen, and Mehran Kardar for enlightening discussions; Christina Lilliehook for feedback on the manuscript; Asier Vidal and Tenzin Kunchok of the W.M Keck Microscopy Facility and the Whitehead Institute Metabolomics Core for advice; members of the Harvard Center for Biological Imaging, the Whitehead Genome Technology Core for their assistance; and ONI for the long-term loan of the Nanoimager. Funding was received as follows: the National Institutes of Health grant GM144283 (to R.A.Y.), National Institutes of Health grant CA155258 (to R.A.Y.), National Science Foundation grant PHY2044895 (to A.C. and R.A.Y.), St. Jude Children's Research Hospital Transcription Collaborative (to R.A.Y.), and the National Institutes of Health grant KL2TR002542 (to J.M.P.).

AUTHOR CONTRIBUTIONS

Conceptualization, A.D., M.M.Z., S.M., J.M.P., T.I.L., and R.A.Y.; methodology, A.D., M.M.Z., S.M., J.M.P., A.T.H., D.K. (computation), G.D., K.J.O., I.S., H.E., N.M.H., O.C., A.K.C. (computation), T.I.L., and R.A.Y.; investigation, A.D., M.M.Z., S.M., J.M.P., A.T.H., D.K. (computation), G.D., K.J.O., I.S., H.E., O.C., A.K.C. (computation), T.I.L., and R.A.Y.; visualization, A.D., M.M.Z., S.M., J.M.P., A.T.H., D.K. (computation), G.D., O.C., A.K.C. (computation), T.I.L., and R.A.Y.; funding acquisition, R.A.Y., A.K.C., O.C., and J.M.P.; project administration, T.I.L. and R.A.Y.; supervision, T.I.L. and R.A.Y.; writing – original draft, A.D., M.M.Z., S.M., J.M.P., T.I.L., and R.A.Y.; writing – review & editing, A.D., M.M.Z., S.M., J.M.P., A.T.H., D.K., G.D., K.J.O., H.E., O.C., A.K.C., T.I.L., and R.A.Y.

DECLARATION OF INTERESTS

The Whitehead Institute has filed a patent application based on this paper. A.D. is a consultant for Dewpoint Therapeutics. A.K.C. is a consultant (titled "Academic Partner") of Flagship Pioneering, a consultant and member of the Strategic Oversight Board of Apriori Bio (a Flagship company), and a consultant and SAB member of Metaphore Bio (a Flagship company). R.A.Y. is a founder or shareholder of Syros Pharmaceuticals, Camp4 Therapeutics, Omega Therapeutics, Dewpoint Therapeutics, Paratus Sciences, and Precede Biosciences and has an advisory role at Novo Nordisk.

STAR★METHODS

Detailed methods are provided in the online version of this paper and include the following:

- KEY RESOURCES TABLE

SUPPLEMENTAL INFORMATION

Supplemental information can be found online at https://doi.org/10.1016/j.cell.2024.10.051.

Received: March 16, 2024
Revised: August 7, 2024
Accepted: October 31, 2024
Published: November 27, 2024

REFERENCES

1. Hajat, C., and Stein, E. (2018). The global burden of multiple chronic conditions: A narrative review. Prev. Med. Rep. *12*, 284–293. https://doi.org/10.1016/j.pmedr.2018.10.008.
2. Collins, F.S.D., Doudna, J.A., Lander, E.S., and Rotimi, C.N. (2021). Human Molecular Genetics and Genomics — Important Advances and Exciting Possibilities. N. Engl. J. Med. *384*, 1–4. https://doi.org/10.1056/NEJMp2030694.
3. Roden, M., and Shulman, G.I. (2019). The integrative biology of type 2 diabetes. Nature *576*, 51–60. https://doi.org/10.1038/s41586-019-1797-8.
4. Langley, M.R., Rangaraju, S., Dey, A., and Sarkar, S. (2022). Editorial: Environmental Effect on Neuroinflammation and Neurodegeneration. Front. Cell. Neurosci. *16*, 935190. https://doi.org/10.3389/fncel.2022.935190.
5. Janssen, J.A.M.J.L. (2021). Hyperinsulinemia and Its Pivotal Role in Aging, Obesity, Type 2 Diabetes, Cardiovascular Disease and Cancer. Int. J. Mol. Sci. *22*, 7797. https://doi.org/10.3390/ijms22157797.
6. Shanik, M.H., Xu, Y., Skrha, J., Dankner, R., Zick, Y., and Roth, J. (2008). Insulin resistance and hyperinsulinemia: is hyperinsulinemia the cart or the horse? Diabetes Care *31* (suppl 2), S262–S268. https://doi.org/10.2337/dc08-s264.
7. Crofts, C.A.P.Z. (2015). Hyperinsulinemia: A unifying theory of chronic disease? Diabesity *1*, 34–43. https://doi.org/10.15562/diabesity.2015.19.
8. DeFronzo, R.A., Ferrannini, E., Groop, L., Henry, R.R., Herman, W.H., Holst, J.J., Hu, F.B., Kahn, C.R., Raz, I., Shulman, G.I., et al. (2015). Type 2 diabetes mellitus. Nat. Rev. Dis. Primers *1*, 15019. https://doi.org/10.1038/nrdp.2015.19.
9. Liu, J., Liu, S., Yu, Z., Qiu, X., Jiang, R., and Li, W. (2022). Uncovering the gene regulatory network of type 2 diabetes through multi-omic data integration. J. Transl. Med. *20*, 604. https://doi.org/10.1186/s12967-022-03826-5.
10. Ahmed, S.A.H., Ansari, S.A., Mensah-Brown, E.P.K., and Emerald, B.S. (2020). The role of DNA methylation in the pathogenesis of type 2 diabetes mellitus. Clin. Epigenetics *12*, 104. https://doi.org/10.1186/s13148-020-00896-4.
11. Dlamini, Z., Mokoena, F., and Hull, R. (2017). Abnormalities in alternative splicing in diabetes: therapeutic targets. J. Mol. Endocrinol. *59*, R93–R107. https://doi.org/10.1530/JME-17-0049.
12. Kobiita, A., Godbersen, S., Araldi, E., Ghoshdastider, U., Schmid, M.W., Spinas, G., Moch, H., and Stoffel, M. (2020). The Diabetes Gene JAZF1 Is Essential for the Homeostatic Control of Ribosome Biogenesis and Function in Metabolic Stress. Cell Rep. *32*, 107846. https://doi.org/10.1016/j.celrep.2020.107846.
13. Yuan, Q., Tang, B., and Zhang, C. (2022). Signaling pathways of chronic kidney diseases, implications for therapeutics. Signal Transduct. Target. Ther. *7*, 182. https://doi.org/10.1038/s41392-022-01036-5.
14. Bradner, J.E., Hnisz, D., and Young, R.A. (2017). Transcriptional addiction in cancer. Cell *168*, 629–643. https://doi.org/10.1016/j.cell.2016.12.013.
15. Meng, G., and Mei, H. (2019). Transcriptional Dysregulation Study Reveals a Core Network Involving the Progression of Alzheimer's Disease. Front. Aging Neurosci. *11*, 101. https://doi.org/10.3389/fnagi.2019.00101.
16. Gandal, M.J., Haney, J.R., Wamsley, B., Yap, C.X., Parhami, S., Emani, P.S., Chang, N., Chen, G.T., Hoftman, G.D., de Alba, D., et al. (2022). Broad transcriptomic dysregulation occurs across the cerebral cortex in ASD. Nature *611*, 532–539. https://doi.org/10.1038/s41586-022-05377-7.
17. Fuller, H., Zhu, Y., Nicholas, J., Chatelaine, H.A., Drzymalla, E.M., Sarvestani, A.K., Julián-Serrano, S., Tahir, U.A., Sinnott-Armstrong, N., Raffield, L.M., et al. (2023). Metabolomic epidemiology offers insights into disease aetiology. Nat. Metab. *5*, 1656–1672. https://doi.org/10.1038/s42255-023-00903-x.
18. Jiao, L., Liu, Y., Yu, X.Y., Pan, X., Zhang, Y., Tu, J., Song, Y.H., and Li, Y. (2023). Ribosome biogenesis in disease: new players and therapeutic targets. Signal Transduct. Target. Ther. *8*, 15. https://doi.org/10.1038/s41392-022-01285-4.
19. Misteli, T. (2008). Physiological importance of RNA and protein mobility in the cell nucleus. Histochem. Cell Biol. *129*, 5–11. https://doi.org/10.1007/s00418-007-0355-x.
20. Misteli, T. (2001). Protein dynamics: implications for nuclear architecture and gene expression. Science *291*, 843–847. https://doi.org/10.1126/science.291.5505.843.
21. Ellis, R.J. (2001). Macromolecular crowding: an important but neglected aspect of the intracellular environment. Curr. Opin. Struct. Biol. *11*, 114–119. https://doi.org/10.1016/s0959-440x(00)00172-x.
22. Axelrod, D., Koppel, D.E., Schlessinger, J., Elson, E., and Webb, W.W. (1976). Mobility measurement by analysis of fluorescence photobleaching recovery kinetics. Biophys. J. *16*, 1055–1069. https://doi.org/10.1016/S0006-3495(76)85755-4.
23. Berg, H. (1993). Random Walks in Biology, Expanded Edition (Princeton University Press).
24. Lakadamyali, M. (2022). Single nucleosome tracking to study chromatin plasticity. Curr. Opin. Cell Biol. *74*, 23–28. https://doi.org/10.1016/j.ceb.2021.12.005.
25. Su, X., Ditlev, J.A., Hui, E., Xing, W., Banjade, S., Okrut, J., King, D.S., Taunton, J., Rosen, M.K., and Vale, R.D. (2016). Phase separation of

signaling molecules promotes T cell receptor signal transduction. Science *352*, 595–599. https://doi.org/10.1126/science.aad9964.

26. Ditlev, J.A., Vega, A.R., Köster, D.V., Su, X., Tani, T., Lakoduk, A.M., Vale, R.D., Mayor, S., Jaqaman, K., and Rosen, M.K. (2019). A composition-dependent molecular clutch between T cell signaling condensates and actin. eLife *8*, e42695. https://doi.org/10.7554/eLife.42695.

27. Delarue, M., Brittingham, G.P., Pfeffer, S., Surovtsev, I.V., Pinglay, S., Kennedy, K.J., Schaffer, M., Gutierrez, J.I., Sang, D., Poterewicz, G., et al. (2018). mTORC1 Controls Phase Separation and the Biophysical Properties of the Cytoplasm by Tuning Crowding. Cell *174*, 338–349.e20. https://doi.org/10.1016/j.cell.2018.05.042.

28. Dall'Agnese, A., Platt, J.M., Zheng, M.M., Friesen, M., Dall'Agnese, G., Blaise, A.M., Spinelli, J.B., Henninger, J.E., Tevonian, E.N., Hannett, N.M., et al. (2022). The dynamic clustering of insulin receptor underlies its signaling and is disrupted in insulin resistance. Nat. Commun. *13*, 7522. https://doi.org/10.1038/s41467-022-35176-7.

29. Li, H., Zhang, J., Shi, Y., Zhao, G., Xu, H., Cai, M., Gao, J., and Wang, H. (2022). Mechanism of INSR clustering with insulin activation and resistance revealed by super-resolution imaging. Nanoscale *14*, 7747–7755. https://doi.org/10.1039/d2nr01051h.

30. Nair, S.J., Yang, L., Meluzzi, D., Oh, S., Yang, F., Friedman, M.J., Wang, S., Suter, T., Alshareedah, I., Gamliel, A., et al. (2019). Phase separation of ligand-activated enhancers licenses cooperative chromosomal enhancer assembly. Nat. Struct. Mol. Biol. *26*, 193–203. https://doi.org/10.1038/s41594-019-0190-5.

31. Persson, L.B., Ambati, V.S., and Brandman, O. (2020). Cellular Control of Viscosity Counters Changes in Temperature and Energy Availability. Cell *183*, 1572–1585.e16. https://doi.org/10.1016/j.cell.2020.10.017.

32. Alejo, J.L., Kempes, C.P., and Adamala, K.P. (2022). Diffusion control in biochemical specificity. Biophys. J. *121*, 1541–1548. https://doi.org/10.1016/j.bpj.2022.03.005.

33. Schavemaker, P.E., Boersma, A.J., and Poolman, B. (2018). How Important Is Protein Diffusion in Prokaryotes? Front. Mol. Biosci. *5*, 93. https://doi.org/10.3389/fmolb.2018.00093.

34. Gralle, M., Labrecque, S., Salesse, C., and De Koninck, P. (2021). Spatial dynamics of the insulin receptor in living neurons. J. Neurochem. *156*, 88–105. https://doi.org/10.1111/jnc.14950.

35. Oksuz, O., Henninger, J.E., Warneford-Thomson, R., Zheng, M.M., Erb, H., Vancura, A., Overholt, K.J., Hawken, S.W., Banani, S.F., Lauman, R., et al. (2023). Transcription factors interact with RNA to regulate genes. Mol. Cell *83*, 2449–2463.e13. https://doi.org/10.1016/j.molcel.2023.06.012.

36. Mir, M., Stadler, M.R., Ortiz, S.A., Hannon, C.E., Harrison, M.M., Darzacq, X., and Eisen, M.B. (2018). Dynamic multifactor hubs interact transiently with sites of active transcription in Drosophila embryos. eLife *7*, e40497. https://doi.org/10.7554/eLife.40497.

37. Gómez-García, P.A., Portillo-Ledesma, S., Neguembor, M.V., Pesaresi, M., Oweis, W., Rohrlich, T., Wieser, S., Meshorer, E., Schlick, T., Cosma, M.P., and Lakadamyali, M. (2021). Mesoscale Modeling and Single-Nucleosome Tracking Reveal Remodeling of Clutch Folding and Dynamics in Stem Cell Differentiation. Cell Rep. *34*, 108614. https://doi.org/10.1016/j.celrep.2020.108614.

38. Sefried, S., Häring, H.U., Weigert, C., and Eckstein, S.S. (2018). Suitability of hepatocyte cell lines HepG2, AML12 and THLE-2 for investigation of insulin signalling and hepatokine gene expression. Open Biol. *8*, 180147. https://doi.org/10.1098/rsob.180147.

39. Irvine, K.M., Skoien, R., Bokil, N.J., Melino, M., Thomas, G.P., Loo, D., Gabrielli, B., Hill, M.M., Sweet, M.J., Clouston, A.D., and Powell, E.E. (2014). Senescent human hepatocytes express a unique secretory phenotype and promote macrophage migration. World J. Gastroenterol. *20*, 17851–17862. https://doi.org/10.3748/wjg.v20.i47.17851.

40. Müller, F.A., and Sturla, S.J. (2019). Human in vitro models of nonalcoholic fatty liver disease. Curr. Opin. Toxicol. *16*, 9–16. https://doi.org/10.1016/j.cotox.2019.03.001.

41. Wang, Z.D., and Deng, W. (2022). Dynamic transcription regulation at the single-molecule level. Dev. Biol. *482*, 67–81. https://doi.org/10.1016/j.ydbio.2021.11.004.

42. Chen, K.Y., Jenkins, E., Körbel, M., Ponjavic, A., Lippert, A.H., Santos, A.M., Ashman, N., O'Brien-Ball, C., McBride, J., Klenerman, D., and Davis, S.J. (2021). Trapping or slowing the diffusion of T cell receptors at close contacts initiates T cell signaling. Proc. Natl. Acad. Sci. USA *118*, e2024250118. https://doi.org/10.1073/pnas.2024250118.

43. Bryan, L.C., Weilandt, D.R., Bachmann, A.L., Kilic, S., Lechner, C.C., Odermatt, P.D., Fantner, G.E., Georgeon, S., Hantschel, O., Hatzimanikatis, V., and Fierz, B. (2017). Single-molecule kinetic analysis of HP1-chromatin binding reveals a dynamic network of histone modification and DNA interactions. Nucleic Acids Res. *45*, 10504–10517. https://doi.org/10.1093/nar/gkx697.

44. Sabari, B.R., Dall'Agnese, A., Boija, A., Klein, I.A., Coffey, E.L., Shrinivas, K., Abraham, B.J., Hannett, N.M., Zamudio, A.V., Manteiga, J.C., et al. (2018). Coactivator condensation at super-enhancers links phase separation and gene control. Science *361*, eaar3958. https://doi.org/10.1126/science.aar3958.

45. Feric, M., Vaidya, N., Harmon, T.S., Mitrea, D.M., Zhu, L., Richardson, T.M., Kriwacki, R.W., Pappu, R.V., and Brangwynne, C.P. (2016). Coexisting Liquid Phases Underlie Nucleolar Subcompartments. Cell *165*, 1686–1697. https://doi.org/10.1016/j.cell.2016.04.047.

46. Song, S.H., McIntyre, S.S., Shah, H., Veldhuis, J.D., Hayes, P.C., and Butler, P.C. (2000). Direct measurement of pulsatile insulin secretion from the portal vein in human subjects. J. Clin. Endocrinol. Metab. *85*, 4491–4499. https://doi.org/10.1210/jcem.85.12.7043.

47. Pørksen, N., Grøfte, T., Greisen, J., Mengel, A., Juhl, C., Veldhuis, J.D., Schmitz, O., Rössle, M., and Vilstrup, H. (2002). Human insulin release processes measured by intraportal sampling. Am. J. Physiol. Endocrinol. Metab. *282*, E695–E702. https://doi.org/10.1152/ajpendo.00516.2000.

48. Alaaeldin, R., Abdel-Rahman, I.A.M., Hassan, H.A., Youssef, N., Allam, A.E., Abdelwahab, S.F., Zhao, Q.L., and Fathy, M. (2021). Carpachromene Ameliorates Insulin Resistance in HepG2 Cells via Modulating IR/IRS1/PI3k/Akt/GSK3/FoxO1 Pathway. Molecules *26*, 7629. https://doi.org/10.3390/molecules26247629.

49. Sabari, B.R., Dall'Agnese, A., and Young, R.A. (2020). Biomolecular Condensates in the Nucleus. Trends Biochem. Sci. *45*, 961–977. https://doi.org/10.1016/j.tibs.2020.06.007.

50. Strom, A.R., Emelyanov, A.V., Mir, M., Fyodorov, D.V., Darzacq, X., and Karpen, G.H. (2017). Phase separation drives heterochromatin domain formation. Nature *547*, 241–245. https://doi.org/10.1038/nature22989.

51. Larson, A.G., Elnatan, D., Keenen, M.M., Trnka, M.J., Johnston, J.B., Burlingame, A.L., Agard, D.A., Redding, S., and Narlikar, G.J. (2017). Liquid droplet formation by HP1alpha suggests a role for phase separation in heterochromatin. Nature *547*, 236–240. https://doi.org/10.1038/nature22822.

52. Spector, D.L., and Lamond, A.I. (2011). Nuclear speckles. Cold Spring Harb. Perspect. Biol. *3*, a000646. https://doi.org/10.1101/cshperspect.a000646.

53. Banani, S.F., Lee, H.O., Hyman, A.A., and Rosen, M.K. (2017). Biomolecular condensates: organizers of cellular biochemistry. Nat. Rev. Mol. Cell Biol. *18*, 285–298. https://doi.org/10.1038/nrm.2017.7.

54. Brangwynne, C.P., Eckmann, C.R., Courson, D.S., Rybarska, A., Hoege, C., Gharakhani, J., Jülicher, F., and Hyman, A.A. (2009). Germline P granules are liquid droplets that localize by controlled dissolution/condensation. Science *324*, 1729–1732. https://doi.org/10.1126/science.1172046.

55. Alberti, S. (2017). The wisdom of crowds: regulating cell function through condensed states of living matter. J. Cell Sci. *130*, 2789–2796. https://doi.org/10.1242/jcs.200295.

56. Huang, X., Chen, S., Li, W., Tang, L., Zhang, Y., Yang, N., Zou, Y., Zhai, X., Xiao, N., Liu, W., et al. (2021). ROS regulated reversible protein phase separation synchronizes plant flowering. Nat. Chem. Biol. *17*, 549–557. https://doi.org/10.1038/s41589-021-00739-0.

57. Chong, P.A., and Forman-Kay, J.D. (2019). Oxidative Inhibition of Pbp1 Phase Separation. Biochemistry *58*, 3057–3059. https://doi.org/10.1021/acs.biochem.9b00511.

58. Kato, M., Yang, Y.S., Sutter, B.M., Wang, Y., McKnight, S.L., and Tu, B.P. (2019). Redox State Controls Phase Separation of the Yeast Ataxin-2 Protein via Reversible Oxidation of Its Methionine-Rich Low-Complexity Domain. Cell *177*, 711–721.e8. https://doi.org/10.1016/j.cell.2019.02.044.

59. Visser, A.J.W.G., Westphal, A.H., Skakun, V.V., and Borst, J.W. (2016). GFP as potential cellular viscosimeter. Methods Appl. Fluoresc. *4*, 035002. https://doi.org/10.1088/2050-6120/4/3/035002.

60. Adrien, V., Rayan, G., Astafyeva, K., Broutin, I., Picard, M., Fuchs, P., Urbach, W., and Taulier, N. (2022). How to best estimate the viscosity of lipid bilayers. Biophys. Chem. *281*, 106732. https://doi.org/10.1016/j.bpc.2021.106732.

61. Pucadyil, T.J., and Chattopadhyay, A. (2006). Confocal fluorescence recovery after photobleaching of green fluorescent protein in solution. J. Fluoresc. *16*, 87–94. https://doi.org/10.1007/s10895-005-0019-y.

62. Ge, X., Yu, Q., Qi, W., Shi, X., and Zhai, Q. (2008). Chronic insulin treatment causes insulin resistance in 3T3-L1 adipocytes through oxidative stress. Free Radic. Res. *42*, 582–591. https://doi.org/10.1080/10715760802158448.

63. Cumming, R.C., Andon, N.L., Haynes, P.A., Park, M., Fischer, W.H., and Schubert, D. (2004). Protein disulfide bond formation in the cytoplasm during oxidative stress. J. Biol. Chem. *279*, 21749–21758. https://doi.org/10.1074/jbc.M312267200.

64. Wilkins, D.K., Grimshaw, S.B., Receveur, V., Dobson, C.M., Jones, J.A., and Smith, L.J. (1999). Hydrodynamic radii of native and denatured proteins measured by pulse field gradient NMR techniques. Biochemistry *38*, 16424–16431. https://doi.org/10.1021/bi991765q.

65. Winter, J., Ilbert, M., Graf, P.C., Ozcelik, D., and Jakob, U. (2008). Bleach activates a redox-regulated chaperone by oxidative protein unfolding. Cell *135*, 691–701. https://doi.org/10.1016/j.cell.2008.09.024.

66. Ilbert, M., Horst, J., Ahrens, S., Winter, J., Graf, P.C.F., Lilie, H., and Jakob, U. (2007). The redox-switch domain of Hsp33 functions as dual stress sensor. Nat. Struct. Mol. Biol. *14*, 556–563. https://doi.org/10.1038/nsmb1244.

67. Knudsen, J.R., Persson, K.W., Henriquez-Olguin, C., Li, Z., Di Leo, N., Hesselager, S.A., Raun, S.H., Hingst, J.R., Trouillon, R., Wohlwend, M., et al. (2023). Microtubule-mediated GLUT4 trafficking is disrupted in insulin-resistant skeletal muscle. eLife *12*, e83338. https://doi.org/10.7554/eLife.83338.

68. Mahmud, Z., Malik, S.U.F., Ahmed, J., and Azad, A.K. (2016). Computational Analysis of Damaging Single-Nucleotide Polymorphisms and Their Structural and Functional Impact on the Insulin Receptor. BioMed Res. Int. *2016*, 2023803. https://doi.org/10.1155/2016/2023803.

69. Borsari, C., Keles, E., McPhail, J.A., Schaefer, A., Sriramaratnam, R., Goch, W., Schaefer, T., De Pascale, M., Bal, W., Gstaiger, M., et al. (2022). Covalent Proximity Scanning of a Distal Cysteine to Target PI3-Kalpha. J. Am. Chem. Soc. *144*, 6326–6342. https://doi.org/10.1021/jacs.1c13568.

70. Sharifi-Rad, M., Anil Kumar, N.V., Zucca, P., Varoni, E.M., Dini, L., Panzarini, E., Rajkovic, J., Tsouh Fokou, P.V., Azzini, E., Peluso, I., et al. (2020). Lifestyle, Oxidative Stress, and Antioxidants: Back and Forth in the Pathophysiology of Chronic Diseases. Front. Physiol. *11*, 694. https://doi.org/10.3389/fphys.2020.00694.

71. Panahi, G., Pasalar, P., Zare, M., Rizzuto, R., and Meshkani, R. (2018). High glucose induces inflammatory responses in HepG2 cells via the oxidative stress-mediated activation of NF-kappaB, and MAPK pathways in HepG2 cells. Arch. Physiol. Biochem. *124*, 468–474. https://doi.org/10.1080/13813455.2018.1427764.

72. Fischer, R., and Maier, O. (2015). Interrelation of oxidative stress and inflammation in neurodegenerative disease: role of TNF. Oxid. Med. Cell. Longev. *2015*, 610813. https://doi.org/10.1155/2015/610813.

73. Ly, L.D., Xu, S., Choi, S.K., Ha, C.M., Thoudam, T., Cha, S.K., Wiederkehr, A., Wollheim, C.B., Lee, I.K., and Park, K.S. (2017). Oxidative stress and calcium dysregulation by palmitate in type 2 diabetes. Exp. Mol. Med. *49*, e291. https://doi.org/10.1038/emm.2016.157.

74. Raza, H., John, A., and Shafarin, J. (2016). Potentiation of LPS-Induced Apoptotic Cell Death in Human Hepatoma HepG2 Cells by Aspirin via ROS and Mitochondrial Dysfunction: Protection by N-Acetyl Cysteine. PLoS One *11*, e0159750. https://doi.org/10.1371/journal.pone.0159750.

75. Shin, H.J., Kwon, H.K., Lee, J.H., Anwar, M.A., and Choi, S. (2016). Etoposide induced cytotoxicity mediated by ROS and ERK in human kidney proximal tubule cells. Sci. Rep. *6*, 34064. https://doi.org/10.1038/srep34064.

76. Jackson, S.P., and Bartek, J. (2009). The DNA-damage response in human biology and disease. Nature *461*, 1071–1078. https://doi.org/10.1038/nature08467.

77. Singh, A., Koduru, B., Carlisle, C., Akhter, H., Liu, R.M., Schroder, K., Brandes, R.P., and Ojcius, D.M. (2017). NADPH oxidase 4 modulates hepatic responses to lipopolysaccharide mediated by Toll-like receptor-4. Sci. Rep. *7*, 14346. https://doi.org/10.1038/s41598-017-14574-8.

78. González, P., Lozano, P., Ros, G., and Solano, F. (2023). Hyperglycemia and Oxidative Stress: An Integral, Updated and Critical Overview of Their Metabolic Interconnections. Int. J. Mol. Sci. *24*, 9352. https://doi.org/10.3390/ijms24119352.

79. Inoguchi, T., Li, P., Umeda, F., Yu, H.Y., Kakimoto, M., Imamura, M., Aoki, T., Etoh, T., Hashimoto, T., Naruse, M., et al. (2000). High glucose level and free fatty acid stimulate reactive oxygen species production through protein kinase C--dependent activation of NAD(P)H oxidase in cultured vascular cells. Diabetes *49*, 1939–1945. https://doi.org/10.2337/diabetes.49.11.1939.

80. Chen, X., Andresen, B.T., Hill, M., Zhang, J., Booth, F., and Zhang, C. (2008). Role of Reactive Oxygen Species in Tumor Necrosis Factor-alpha Induced Endothelial Dysfunction. Curr. Hypertens. Rev. *4*, 245–255. https://doi.org/10.2174/157340208786241336.

81. Griffin, M.E., Marcucci, M.J., Cline, G.W., Bell, K., Barucci, N., Lee, D., Goodyear, L.J., Kraegen, E.W., White, M.F., and Shulman, G.I. (1999). Free fatty acid-induced insulin resistance is associated with activation of protein kinase C theta and alterations in the insulin signaling cascade. Diabetes *48*, 1270–1274. https://doi.org/10.2337/diabetes.48.6.1270.

82. Schulze-Osthoff, K., Bakker, A.C., Vanhaesebroeck, B., Beyaert, R., Jacob, W.A., and Fiers, W. (1992). Cytotoxic activity of tumor necrosis factor is mediated by early damage of mitochondrial functions. Evidence for the involvement of mitochondrial radical generation. J. Biol. Chem. *267*, 5317–5323. https://doi.org/10.1016/S0021-9258(18)42768-8.

83. Rosca, M.G., Vazquez, E.J., Chen, Q., Kerner, J., Kern, T.S., and Hoppel, C.L. (2012). Oxidation of fatty acids is the source of increased mitochondrial reactive oxygen species production in kidney cortical tubules in early diabetes. Diabetes *61*, 2074–2083. https://doi.org/10.2337/db11-1437.

84. Baldyga, J., and Bourne, J.R. (1999). Turbulent Mixing and Chemical Reactions (Wiley).

85. Yoshimura, S.H., Otsuka, S., Kumeta, M., Taga, M., and Takeyasu, K. (2013). Intermolecular disulfide bonds between nucleoporins regulate karyopherin-dependent nuclear transport. J. Cell Sci. *126*, 3141–3150. https://doi.org/10.1242/jcs.124172.

86. Higo, S., Asano, Y., Kato, H., Yamazaki, S., Nakano, A., Tsukamoto, O., Seguchi, O., Asai, M., Asakura, M., Asanuma, H., et al. (2010). Isoform-specific intermolecular disulfide bond formation of heterochromatin protein 1 (HP1). J. Biol. Chem. *285*, 31337–31347. https://doi.org/10.1074/jbc.M110.155788.

87. Portolés, M.T., Pagani, R., Díaz-Laviada, I., and Municio, A.M. (1987). Effect of Escherichia coli lipopolysaccharide on the microviscosity of liver plasma membranes and hepatocyte suspensions and monolayers. Cell Biochem. Funct. *5*, 55–61. https://doi.org/10.1002/cbf.290050107.

88. de la Haba, C., Palacio, J.R., Martínez, P., and Morros, A. (2013). Effect of oxidative stress on plasma membrane fluidity of THP-1 induced macrophages. Biochim. Biophys. Acta *1828*, 357–364. https://doi.org/10.1016/j.bbamem.2012.08.013.

89. Perona, J.S. (2017). Membrane lipid alterations in the metabolic syndrome and the role of dietary oils. Biochim. Biophys. Acta Biomembr. *1859*, 1690–1703. https://doi.org/10.1016/j.bbamem.2017.04.015.

90. Tsuda, K., Kinoshita, Y., Nishio, I., and Masuyama, Y. (2001). Hyperinsulinemia is a determinant of membrane fluidity of erythrocytes in essential hypertension. Am. J. Hypertens. *14*, 419–423. https://doi.org/10.1016/s0895-7061(00)01247-4.

91. Pilon, M. (2016). Revisiting the membrane-centric view of diabetes. Lipids Health Dis. *15*, 167. https://doi.org/10.1186/s12944-016-0342-0.

92. Winocour, P.D., Watala, C., and Kinglough-Rathbone, R.L. (1992). Membrane fluidity is related to the extent of glycation of proteins, but not to alterations in the cholesterol to phospholipid molar ratio in isolated platelet membranes from diabetic and control subjects. Thromb. Haemost. *67*, 567–571. https://doi.org/10.1055/s-0038-1648495.

93. Kamboj, S.S., Chopra, K., and Sandhir, R. (2009). Hyperglycemia-induced alterations in synaptosomal membrane fluidity and activity of membrane bound enzymes: beneficial effect of N-acetylcysteine supplementation. Neuroscience *162*, 349–358. https://doi.org/10.1016/j.neuroscience.2009.05.002.

94. Jaqaman, K., and Grinstein, S. (2012). Regulation from within: the cytoskeleton in transmembrane signaling. Trends Cell Biol. *22*, 515–526. https://doi.org/10.1016/j.tcb.2012.07.006.

95. Carlini, L., Brittingham, G.P., Holt, L.J., and Kapoor, T.M. (2020). Microtubules Enhance Mesoscale Effective Diffusivity in the Crowded Metaphase Cytoplasm. Dev. Cell *54*, 574–582.e4. https://doi.org/10.1016/j.devcel.2020.07.020.

96. Molines, A.T., Lemière, J., Gazzola, M., Steinmark, I.E., Edrington, C.H., Hsu, C.T., Real-Calderon, P., Suhling, K., Goshima, G., Holt, L.J., et al. (2022). Physical properties of the cytoplasm modulate the rates of microtubule polymerization and depolymerization. Dev. Cell *57*, 466–479.e6. https://doi.org/10.1016/j.devcel.2022.02.001.

97. Cho, W.K., Spille, J.H., Hecht, M., Lee, C., Li, C., Grube, V., and Cisse, I.I. (2018). Mediator and RNA polymerase II clusters associate in transcription-dependent condensates. Science *361*, 412–415. https://doi.org/10.1126/science.aar4199.

98. Keber, F.C., Nguyen, T., Mariossi, A., Brangwynne, C.P., and Wühr, M. (2024). Evidence for widespread cytoplasmic structuring into mesoscale condensates. Nat. Cell Biol. *26*, 346–352. https://doi.org/10.1038/s41556-024-01363-5.

99. Chong, S., Dugast-Darzacq, C., Liu, Z., Dong, P., Dailey, G.M., Cattoglio, C., Heckert, A., Banala, S., Lavis, L., Darzacq, X., and Tjian, R. (2018). Imaging dynamic and selective low-complexity domain interactions that control gene transcription. Science *361*, eaar2555. https://doi.org/10.1126/science.aar2555.

100. Cho, W.K., Jayanth, N., English, B.P., Inoue, T., Andrews, J.O., Conway, W., Grimm, J.B., Spille, J.H., Lavis, L.D., Lionnet, T., and Cisse, I.I. (2016). RNA Polymerase II cluster dynamics predict mRNA output in living cells. eLife *5*, e13617. https://doi.org/10.7554/eLife.13617.

101. Ray, P.D., Huang, B.W., and Tsuji, Y. (2012). Reactive oxygen species (ROS) homeostasis and redox regulation in cellular signaling. Cell. Signal. *24*, 981–990. https://doi.org/10.1016/j.cellsig.2012.01.008.

102. Schieber, M., and Chandel, N.S. (2014). ROS function in redox signaling and oxidative stress. Curr. Biol. *24*, R453–R462. https://doi.org/10.1016/j.cub.2014.03.034.

103. Klein, I.A., Boija, A., Afeyan, L.K., Hawken, S.W., Fan, M., Dall'Agnese, A., Oksuz, O., Henninger, J.E., Shrinivas, K., Sabari, B.R., et al. (2020). Partitioning of cancer therapeutics in nuclear condensates. Science *368*, 1386–1392. https://doi.org/10.1126/science.aaz4427.

104. Stringer, C., Wang, T., Michaelos, M., and Pachitariu, M. (2021). Cellpose: a generalist algorithm for cellular segmentation. Nat. Methods *18*, 100–106. https://doi.org/10.1038/s41592-020-01018-x.

105. Dobin, A., Davis, C.A., Schlesinger, F., Drenkow, J., Zaleski, C., Jha, S., Batut, P., Chaisson, M., and Gingeras, T.R. (2013). STAR: ultrafast universal RNA-seq aligner. Bioinformatics *29*, 15–21. https://doi.org/10.1093/bioinformatics/bts635.

106. Jin, Y., Tam, O.H., Paniagua, E., and Hammell, M. (2015). TEtranscripts: a package for including transposable elements in differential expression analysis of RNA-seq datasets. Bioinformatics *31*, 3593–3599. https://doi.org/10.1093/bioinformatics/btv422.

107. Li, H., and Durbin, R. (2009). Fast and accurate short read alignment with Burrows-Wheeler transform. Bioinformatics *25*, 1754–1760. https://doi.org/10.1093/bioinformatics/btp324.

108. Zhang, Y., Liu, T., Meyer, C.A., Eeckhoute, J., Johnson, D.S., Bernstein, B.E., Nusbaum, C., Myers, R.M., Brown, M., Li, W., and Liu, X.S. (2008). Model-based analysis of ChIP-Seq (MACS). Genome Biol. *9*, R137. https://doi.org/10.1186/gb-2008-9-9-r137.

109. Quinlan, A.R., and Hall, I.M. (2010). BEDTools: a flexible suite of utilities for comparing genomic features. Bioinformatics *26*, 841–842. https://doi.org/10.1093/bioinformatics/btq033.

110. Chen, X., Zaro, J.L., and Shen, W.C. (2013). Fusion protein linkers: property, design and functionality. Adv. Drug Deliv. Rev. *65*, 1357–1369. https://doi.org/10.1016/j.addr.2012.09.039.

111. Li, C.H., Coffey, E.L., Dall'Agnese, A., Hannett, N.M., Tang, X., Henninger, J.E., Platt, J.M., Oksuz, O., Zamudio, A.V., Afeyan, L.K., et al. (2020). MeCP2 links heterochromatin condensates and neurodevelopmental disease. Nature *586*, 440–444. https://doi.org/10.1038/s41586-020-2574-4.

112. Li, L., Pan, Z., and Yang, X. (2019). Key genes and co-expression network analysis in the livers of type 2 diabetes patients. J. Diabetes Investig. *10*, 951–962. https://doi.org/10.1111/jdi.12998.

113. Guo, Y.E., Manteiga, J.C., Henninger, J.E., Sabari, B.R., Dall'Agnese, A., Hannett, N.M., Spille, J.H., Afeyan, L.K., Zamudio, A.V., Shrinivas, K., et al. (2019). Pol II phosphorylation regulates a switch between transcriptional and splicing condensates. Nature *572*, 543–548. https://doi.org/10.1038/s41586-019-1464-0.

114. Radtke, K.K., Coles, L.D., Mishra, U., Orchard, P.J., Holmay, M., and Cloyd, J.C. (2012). Interaction of N-acetylcysteine and cysteine in human plasma. J. Pharm. Sci. *101*, 4653–4659. https://doi.org/10.1002/jps.23325.

115. Sergé, A., Bertaux, N., Rigneault, H., and Marguet, D. (2008). Dynamic multiple-target tracing to probe spatiotemporal cartography of cell membranes. Nat. Methods *5*, 687–694. https://doi.org/10.1038/nmeth.1233.

116. Ovesný, M., Křížek, P., Borkovec, J., Svindrych, Z., and Hagen, G.M. (2014). ThunderSTORM: a comprehensive ImageJ plug-in for PALM and STORM data analysis and super-resolution imaging. Bioinformatics *30*, 2389–2390. https://doi.org/10.1093/bioinformatics/btu202.

117. Izeddin, I., Recamier, V., Bosanac, L., Cisse, I.I., Boudarene, L., Dugast-Darzacq, C., Proux, F., Benichou, O., Voituriez, R., Bensaude, O., et al. (2014). Single-molecule tracking in live cells reveals distinct target-search strategies of transcription factors in the nucleus. Elife *3*, 02230. https://doi.org/10.7554/eLife.02230.

118. Hansen, A.S., Woringer, M., Grimm, J.B., Lavis, L.D., Tjian, R., and Darzacq, X. (2018). Robust model-based analysis of single-particle tracking experiments with Spot-On. eLife *7*, 33125. https://doi.org/10.7554/eLife.33125.

119. Kent, S., Brown, K., Yang, C.H., Alsaihati, N., Tian, C., Wang, H., and Ren, X. (2020). Phase-Separated Transcriptional Condensates Accelerate Target-Search Process Revealed by Live-Cell Single-Molecule Imaging. Cell Rep. *33*, 108248. https://doi.org/10.1016/j.celrep.2020.108248.

120. Nguyen, V.Q., Ranjan, A., Liu, S., Tang, X., Ling, Y.H., Wisniewski, J., Mizuguchi, G., Li, K.Y., Jou, V., Zheng, Q., et al. (2021). Spatiotemporal coordination of transcription preinitiation complex assembly in live cells. Mol. Cell *81*, 3560–3575.e6. https://doi.org/10.1016/j.molcel.2021.07.022.

121. Chen, J., Zhang, Z., Li, L., Chen, B.C., Revyakin, A., Hajj, B., Legant, W., Dahan, M., Lionnet, T., Betzig, E., et al. (2014). Single-molecule dynamics of enhanceosome assembly in embryonic stem cells. Cell *156*, 1274–1285. https://doi.org/10.1016/j.cell.2014.01.062.

122. Krouglova, T., Vercammen, J., and Engelborghs, Y. (2004). Correct diffusion coefficients of proteins in fluorescence correlation spectroscopy. Application to tubulin oligomers induced by Mg2+ and Paclitaxel. Biophys. J. *87*, 2635–2646. https://doi.org/10.1529/biophysj.104.040717.

123. Banani, S.F., Afeyan, L.K., Hawken, S.W., Henninger, J.E., Dall'Agnese, A., Clark, V.E., Platt, J.M., Oksuz, O., Hannett, N.M., Sagi, I., et al. (2022). Genetic variation associated with condensate dysregulation in disease. Dev. Cell *57*, 1776–1788.e8. https://doi.org/10.1016/j.devcel.2022.06.010.

124. Moses, D., Yu, F., Ginell, G.M., Shamoon, N.M., Koenig, P.S., Holehouse, A.S., and Sukenik, S. (2020). Revealing the Hidden Sensitivity of Intrinsically Disordered Proteins to their Chemical Environment. J. Phys. Chem. Lett. *11*, 10131–10136. https://doi.org/10.1021/acs.jpclett.0c02822.

125. Janin, J. (1979). Surface and inside volumes in globular proteins. Nature *277*, 491–492. https://doi.org/10.1038/277491a0.

126. Heinig, M., and Frishman, D. (2004). STRIDE: a web server for secondary structure assignment from known atomic coordinates of proteins. Nucleic Acids Res. *32*, W500–W502. https://doi.org/10.1093/nar/gkh429.

127. Wang, P., Zhang, Q., Li, S., Cheng, B., Xue, H., Wei, Z., Shao, T., Liu, Z.X., Cheng, H., and Wang, Z. (2021). iCysMod: an integrative database for protein cysteine modifications in eukaryotes. Brief. Bioinform. *22*, bbaa400. https://doi.org/10.1093/bib/bbaa400.

128. Milo, R. (2013). What is the total number of protein molecules per cell volume? A call to rethink some published values. BioEssays *35*, 1050–1055. https://doi.org/10.1002/bies.201300066.

129. Eastman, P., Swails, J., Chodera, J.D., McGibbon, R.T., Zhao, Y., Beauchamp, K.A., Wang, L.P., Simmonett, A.C., Harrigan, M.P., Stern, C.D., et al. (2017). OpenMM 7: Rapid development of high performance algorithms for molecular dynamics. PLoS Comput. Biol. *13*, e1005659. https://doi.org/10.1371/journal.pcbi.1005659.

130. Sies, H. (2017). Hydrogen peroxide as a central redox signaling molecule in physiological oxidative stress: Oxidative eustress. Redox Biol. *11*, 613–619. https://doi.org/10.1016/j.redox.2016.12.035.

131. Zhang, H., and Forman, H.J. (2012). Glutathione synthesis and its role in redox signaling. Semin. Cell Dev. Biol. *23*, 722–728. https://doi.org/10.1016/j.semcdb.2012.03.017.

132. Davies, M.J. (2016). Protein oxidation and peroxidation. Biochem. J. *473*, 805–825. https://doi.org/10.1042/BJ20151227.

133. Winterbourn, C.C., and Metodiewa, D. (1999). Reactivity of biologically important thiol compounds with superoxide and hydrogen peroxide. Free Radic. Biol. Med. *27*, 322–328. https://doi.org/10.1016/s0891-5849(99)00051-9.

134. Fra, A., Yoboue, E.D., and Sitia, R. (2017). Cysteines as Redox Molecular Switches and Targets of Disease. Front. Mol. Neurosci. *10*, 167. https://doi.org/10.3389/fnmol.2017.00167.

135. Szajewski, R.P., and Whitesides, G.M. (1980). Rate constants and equilibrium constants for thiol-disulfide interchange reactions involving oxidized glutathione. J. Am. Chem. Soc. *102*, 2011–2026. https://doi.org/10.1021/ja00526a042.

136. Forman, H.J., Zhang, H., and Rinna, A. (2009). Glutathione: overview of its protective roles, measurement, and biosynthesis. Mol. Aspects Med. *30*, 1–12. https://doi.org/10.1016/j.mam.2008.08.006.

137. Zitka, O., Skalickova, S., Gumulec, J., Masarik, M., Adam, V., Hubalek, J., Trnkova, L., Kruseova, J., Eckschlager, T., and Kizek, R. (2012). Redox status expressed as GSH:GSSG ratio as a marker for oxidative stress in paediatric tumour patients. Oncol. Lett. *4*, 1247–1253. https://doi.org/10.3892/ol.2012.931.

138. Roussel, M.R.; institute of P (2023). Foundations of Chemical Kinetics: a Hands On Approach (IOP Publishing).

139. Dutagaci, B., Nawrocki, G., Goodluck, J., Ashkarran, A.A., Hoogstraten, C.G., Lapidus, L.J., and Feig, M. (2021). Charge-driven condensation of RNA and proteins suggests broad role of phase separation in cytoplasmic environments. eLife *10*, 64004. https://doi.org/10.7554/eLife.64004.

140. Hsieh, M.Y., Yang, S., Raymond-Stinz, M.A., Edwards, J.S., and Wilson, B.S. (2010). Spatio-temporal modeling of signaling protein recruitment to EGFR. BMC Syst. Biol. *4*, 57. https://doi.org/10.1186/1752-0509-4-57.

141. Gura Sadovsky, R., Brielle, S., Kaganovich, D., and England, J.L. (2017). Measurement of Rapid Protein Diffusion in the Cytoplasm by Photo-Converted Intensity Profile Expansion. Cell Rep. *18*, 2795–2806. https://doi.org/10.1016/j.celrep.2017.02.063.

142. Schrödinger, L.D. (2020). PyMOL. http://www.pymol.org/pymol.

STAR★METHODS

KEY RESOURCES TABLE

REAGENT or RESOURCE	SOURCE	IDENTIFIER
Antibodies		
Anti-insulin receptor (IF)	Cell Signaling	23413; RRID: AB_2924796
Anti-MED1 (IF)	Abcam	ab64965; RRID: AB_1142301
Anti-HP1α (IF)	Abcam	ab109028; RRID: AB_10858495
Anti-FIB1 (IF and WB)	Abcam	ab5821; RRID: AB_2105785
Anti-SRSF2 (IF)	Abcam	ab11826; RRID: AB_298608
Anti-insulin receptor (WB)	Cell Signaling	3025; RRID: AB_2280448
Anti-MED1 (WB)	Bethyl	A300-793A; RRID: AB_577241
Anti-SRSF2 (WB)	Thermo Fisher Scientific	PA5-12402; RRID: AB_2184941
Anti-b-actin	Sigma-Aldrich	A5441; RRID: AB_476744
Anti-H3	Cell Signaling	4499; RRID: AB_10544537
Donkey anti-rabbit IgG	Cytiva Life Sciences	NA934-1ML; RRID: AB_772206
Sheep anti-mouse IgG	Cytiva Life Sciences	NXA931V; RRID: N/A
Anti-HA (WB)	Cell Signaling	3724; RRID: AB_1549585
Anti-pIRS1 (WB)	Cell Signaling	3070; RRID: AB_2127863
Anti- IRS1 (WB)	Cell Signaling	2382; RRID: AB_330333
Anti-IR (WB)	Cell Signaling	74118; RRID: AB_2799850
Anti-pIRS1 (IF)	Abcam	ab4873; RRID: AB_304698
Bacterial and virus strains		
NEB® 10-beta Competent E. coli (High Efficiency)	NEB	C3019H
Biological samples		
HepG2 cells	ATCC	HB-8065TM
C2C12 cells	ATCC	CRL-1772
Chemicals, peptides, and recombinant proteins		
Insulin	Sigma-Aldrich	I9278-5ML
H_2O_2	Sigma-Aldrich	H1009
N-acetyl cysteine	Sigma-Aldrich	A9165-25G
Tumor necrosis factor alpha	Thermo Fisher Scientific	PHC3016
Glucose	Sigma-Aldrich	G8270
Lipopolysaccharide	Sigma-Aldrich	L2630
Fatty acid-free BSA	Sigma-Aldrich	A8806-5G
Etoposide	Thermo Scientific Chemicals	J63651
Oleic acid	Sigma-Aldrich	O7501
Palmitic acid	Sigma-Aldrich	P9767
N-acetyl-p-benzoquinone imine (NAPQI)	Sigma-Aldrich	A7300-1mg
Doxycycline	Sigma-Aldrich	D9891-5G
Fetal bovine serum	Sigma-Aldrich	F4135
Janelia Fluor 585	Gift from the Lavis Lab	N/A
Janelia Fluor 549	Promega	GA1110
Hygromycin	Thermo Fisher Scientific	10687-010
TrypanBlue	Invitrogen	T10282
BSA (IF)	Jackson Immunoresearch Laboratories	001-000-162
Hoechst (IF)	Thermo Fischer Scientific	3258

(*Continued on next page*)

Continued

REAGENT or RESOURCE	SOURCE	IDENTIFIER
Hoechst (live cell imaging)	Thermo Fischer Scientific	33342
PBS	Gibco	10010-023
Protease and phosphatase inhibitors	Sigma-Aldrich	11873580001 and 4906837001
Acetonitrile	Thermo Fischer Scientific	A955-4
Methanol	Thermo Fischer Scientific	A456-4
LC-MS grade water (metabolomics)	Thermo Fischer Scientific	W6-4
Ammonium Carbonate	Sigma-Aldrich	379999-50G
Ammonium Hydroxide Solution	Sigma-Aldrich	338818-100mL
Nitric Acid	Thermo Fischer Scientific	A467-500mL
20 Canonicial Metabolomics Amino Acid Mix[2.5 mM each]	Cambridge Isotope Labs	MSK-CAA-1
Purified active recombinant human insulin receptor	Millipore	14-466
Purified recombinant IRS1	Abcam	ab70538
Glycerol	Invitrogen	15514011
Streptavadin, unconjugated	Invitrogen	43-430-2
Biotin	Millipore	B4501
DMSO	Sigma-Aldrich	D2438
Critical commercial assays		
NEBuilder HiFi DNA Assembly Master Mix	NEB	E2621S
Phusion polymerase	Thermo Fisher Scientific	F531S
CellROX Deep Red Reagent	Thermo Fisher Scientific	C10422
Cell Lytic M	Sigma-Aldrich	C2978
BCA Protein Assay Kit	Thermo Fisher Scientific	23250
ECL substrate	Millipore	WBKL20500
TRIzol™ reagent	Thermo Fisher Scientific	15596026
Native Sample Buffer	BioRad	1610738
KAPAHyperRiboErase	Roche	KK8561
Deposited data		
Metabolomics data	Metabolights	Metabolights: MTBLS9535
RNA-seq	GEO	GEO: GSE273733
MED1 ChIP-seq	GEO	GEO: GSM2040029
Input	GEO	GEO: GSM2864933
Experimental models: Cell lines		
HepG2 cells	ATCC	HB-8065TM
C2C12 cells	ATCC	CRL-1772
HepG2 expressing endogenous IR tagged with GFP	Dall'Agnese et al.[28]	N/A
HepG2 expressing endogenous IR tagged with HaloTag	This work	N/A
HepG2 expressing endogenous MED1 tagged with GFP	This work	N/A
HepG2 expressing endogenous MED1 tagged with HaloTag	This work	N/A
HepG2 expressing endogenous HP1α tagged with GFP	This work	N/A
HepG2 expressing endogenous HP1α tagged with HaloTag	This work	N/A
HepG2 expressing endogenous FIB1 tagged with GFP	This work	N/A

(*Continued on next page*)

Continued

REAGENT or RESOURCE	SOURCE	IDENTIFIER
HepG2 expressing endogenous FIB1 tagged with HaloTag	This work	N/A
HepG2 expressing endogenous SRSF2 tagged with GFP	This work	N/A
HepG2 expressing endogenous SRSF2 tagged with HaloTag	This work	N/A
HepG2 expressing endogenous SRSF2-Ser tagged with GFP	This work	N/A
HepG2 expressing endogenous SRSF2-Cys tagged with GFP	This work	N/A
HepG2 expressing GFP	This work	N/A
HepG2 expressing HaloTag	This work	N/A
HepG2 expressing endogenous IR-Y1361S tagged with GFP	This work	N/A
HepG2 expressing endogenous IR-Y1361C tagged with GFP	This work	N/A
HepG2 expressing HaloTag-Cys	This work	N/A
HepG2 expressing HaloTag-Ser	This work	N/A
C2C12 expressing HaloTag-Cys	This work	N/A
HepG2 expressing AviTag-HaloTag-Cys/ BirA-SNAP	This work	N/A
Oligonucleotides for genotyping		
IR_fwd: GGAGAATGTGCCCCTGGAC	IDT/Eton Bioscience	N/A
IR_rev: TTGGTAACCAAACGAGTCCACCT	IDT/Eton Bioscience	N/A
MED1_fwd: CGAGCACCCTTCTCTTCTTG	IDT/Eton Bioscience	N/A
MED1_rev: GAAGTTGAGAGTCCCCATCG	IDT/Eton Bioscience	N/A
HP1α _fwd: CAAGGTGAGGAGGAAATCA	IDT/Eton Bioscience	N/A
HP1α _rev: CACAGGGAAGCAGAAGGAAG	IDT/Eton Bioscience	N/A
SRSF2_fwd: CAAGTCTCCTGAAGAG GAAGGA	IDT/Eton Bioscience	N/A
SRSF2_rev: AAGGGCTGTATCCAAAC AAAAAC	IDT/Eton Bioscience	N/A
FIB1_fwd: CCTTTTAATCAGCAAC CCACTC	IDT/Eton Bioscience	N/A
FIB1_rev: GTGACCGAGTGAGAATT TACCC	IDT/Eton Bioscience	N/A
Recombinant DNA		
Repair template DNA to make endogenously HaloTag tagged cell lines	This work	N/A
gRNA construct DNA to make endogenously tagged cell lines	Klein et al.[103] and this work	N/A
Repair template DNA to make endogenously GFP tagged cell lines	Klein et al.[103] and this work	N/A
Construct to express HaloTag-Cys	This work	N/A
Construct to express HaloTag-Ser	This work	N/A
Construct to express AviTag-HaloTag-Cys	This work	N/A
Construct to express BirA-SNAP	This work	N/A
Software and algorithms		
Prism Version 9.4.0	GraphPad	N/A
Fiji/ImageJ v2.1.0/153c	GraphPad	N/A

(*Continued on next page*)

Continued

REAGENT or RESOURCE	SOURCE	IDENTIFIER
FreeStyle v1.3	Thermo Fisher Scientific	N/A
TraceFinder v4.1	Thermo Fisher Scientific	N/A
ZEN Blue	Zeiss Thermo Fisher Scientific	N/A
MATLAB vR2021b	MathWorks	N/A
Cellpose	Stringer et al.[104]	N/A
STAR	Dobin et al.[105]	N/A
TEtranscripts	Jin et al.[106]	N/A
BWA	Li and Durbin[107]	N/A
MACS2	Zhang et al.[108]	N/A
Bedtools	Quinlan and Hall[109]	N/A
Other		
ZEISS LSM 980 with Airyscan 2 microscope	ZEISS	ZEISS LSM 980 with Airyscan
Elyra 7 microscope	ZEISS	Elyra 7
Nanoimager microscope	ONI	Nanoimager
ClinVar	ClinVar	ClinVar: https://ftp.ncbi.nlm.nih.gov/pub/clinvar/vcf_GRCh38/archive_2.0/2023/clinvar_20230903.vcf.gz https://ftp.ncbi.nlm.nih.gov/pub/clinvar/tab_delimited/variant_summary.txt.gz
Uniprot Swiss-Prot	Uniprot	ClinVar: https://ftp.uniprot.org/pub/databases/uniprot/current_release/knowledgebase/idmapping/by_organism/HUMAN_9606_idmapping_selected.tab.gz https://ftp.uniprot.org/pub/databases/uniprot/current_release/knowledgebase/idmapping/by_organism/HUMAN_9606_idmapping.dat.gz
Brownian dynamics simulations of proteins with surface cysteines	This work	GitHub: https://github.com/younglab/proteolethargy

EXPERIMENTAL MODEL AND STUDY PARTICIPANT DETAILS

HepG2 (male) cells were acquired from ATCC (ATCC, HB-8065TM) and cultured in 150 mm cell culture grade dishes with EMEM media (ATCC, 30-2003) supplemented with 10% fetal bovine serum (FBS; Sigma-Aldrich, F4135) without antibiotic and kept in a humidified incubator at 37°C with 5% CO_2. These cells were chosen because they are widely used to study diverse pathologies and because they can be genetically modified. To passage the cells, 20 ml of room-temperature phosphate buffered saline solution (Gibco, 10010-023) was added to the dish, aspirated off, then 3 ml of TrypLE Express Enzyme (Life Technologies, 12604021) was added to help dissociate cells. The dish was then incubated at 37°C with humidity and 5% CO_2 for 5 minutes. After 5 minutes, cells were mechanically dissociated by pipetting them up and down 7 times using a 10ml serological pipette fitted with a p200 tip. To quench the TrypLE, 7 ml of EMEM-FBS was added to the dish. 1 ml of the cell suspension was left on the dish and 20 ml of EMEM-FBS was added on top. HepG2 cells were continuously cultured in a 150 mm dish and split 1:10 when the cells became confluent. The cells were subcultured on a new plate monthly, seeded using a 1:2 split.

C2C12 (female) cells were acquired from ATCC (ATCC, CRL-1772) and cultured in 150 mm cell culture grade dishes with DMEM media (Gibco, 11965-092) supplemented with 10% fetal bovine serum (FBS; Sigma-Aldrich, F4135) without antibiotic and kept in a humidified incubator at 37°C with 5% CO_2. These cells were chosen because they are widely used to study diverse pathologies and because they can be genetically modified. Cells were passaged at 30-50% confluence to prevent differentiation. To passage the cells, 20 ml of room-temperature phosphate buffered saline solution (Gibco, 10010-023) was added to the dish, aspirated off, then 3 ml of TrypLE Express Enzyme (Life Technologies, 12604021) was added to help dissociate cells from the dish and one another. The dish was then incubated at 37°C with humidity and 5% CO_2 for 5 minutes. After 5 minutes, the cells were dissociated by tapping the sides of the plate. To quench the TrypLE, the cells were resuspended in 7 ml of DMEM supplemented with 10% FBS, and these resuspended cells were used to seed a new dish at a 1:20 dilution.

METHOD DETAILS

Any additional information required to reanalyze the data reported in this paper is available from the lead contact upon request.

Constructs and construct generation

For tagging endogenous proteins (IR, MED1, HP1α, FIB1, and SRSF2) with GFP, HaloTag, or GFP-5xSer/Cys, the homology directed repair (HDR) strategy of CRISPR was adopted. For this strategy, three components are needed: 1) Cas9 protein to cut the DNA, 2) sgRNA to guide Cas9 to the desired target, and 3) a DNA repair template that contains the desired edit as well as 800 bp of homologous sequence immediately upstream and downstream of the target. The sgRNA sequence and Cas9 coding sequence for transient expression of both in cells were integrated in the same plasmid (which was refer to as "sgRNA-Cas9 plasmid"), while the repair templates were integrated into a second plasmid.

sgRNA-Cas9 plasmids

20 bp of target sequences were cloned into a plasmid containing sgRNA backbone, a codon-optimized version of Cas9, and mCherry. The mCherry was used during FACS sorting to select for Cas9-mCherry^{+} cells. Constructs for the generation of MED1-GFP, HP1α-GFP, SRSF2-GFP, FIB1-GFP, and insulin receptor-GFP (IR-GFP) cell lines were described in previous publications.[28,103] To generate the IR-Y1361C-GFP cell line, the following sgRNA sequences with PAM sequence in parentheses were used for CRISPR/Cas9 editing:

sgRNA_IR_C-term_1: CACGGTAGGCACTGTTAGGA(AGG)
sgRNA_IR_C-term_2: TAGGCACTGTTAGGAAGGAT(TGG)
sgRNA_IR_C-term_3: CCTCCGTTCATGTGTGTGTA(AGG)

The other sgRNA sequences are reported in previous publications.[28,103]

Cloning was performed using NEBuilder HiFi DNA Assembly Master Mix (NEB, E2621S) according to manufacturer's specifications.

Repair templates for GFP tagging

Approximately 800bp of Homo sapiens genomic DNA sequences flanking the Cas9 cutting sites were cloned into the pUC19 vector using NEBuilder HiFi DNA Assembly Master Mix (NEB, E2621S), with in-frame monomeric enhanced fluorescent protein (GFP) sequence being inserted together with a flexible 10-animo acid linker sequence (GGSGGGGSGG) to space the fluorophore and the protein of interest. Constructs for MED1-GFP, HP1α-GFP, SRSF2-GFP, FIB1-GFP, and IR-GFP cell line generations are described in previous publications.[28,103] For the IR-Y1361C-GFP cell line generation, the homology repair template consists of INSR exon 22 containing the Y1361C missense mutation in frame with GFP flanked on either side by 800-bp homology arms amplified from HepG2 genomic DNA using PCR. For SRSF2-GFP-Ser/Cys cell line generation, the SRSF2-GFP repair template was modified to fuse SRSF2-GFP to a flexible linker followed by either a 5xSer array or a 5xCys array. The 5xSer array contains 5 serines spaced by a rigid linker (AEAAAKEAAAKA),[110] while the 5xCys array contains 5 cysteines spaced by the same rigid linker.[110] These constructs were cloned using NEBuilder HiFi DNA Assembly Master Mix.

Repair templates for HaloTag tagging

Constructs for MED1-HaloTag, HP1α-HaloTag, SRSF2-HaloTag, FIB1-HaloTag, and IR-HaloTag were generated by replacing the mEGFP with HaloTag in the repair templates using NEBuilder HiFi DNA Assembly Master Mix.

To generate cells for doxycycline-inducible expression of GFP, HaloTag, HaloTag-Ser/Cys, or AviTag-HaloTag-Cys/BirA-SNAP, a PiggyBac vector[28] was used to make the GFP, HaloTag or SNAP-tag containing construct.

PiggyBac vectors for doxycycline-inducible expression of GFP, HaloTag or SNAP

Sequences of SiriusGFP, HaloTag, or SNAP-tag were cloned using NEBuilder HiFi DNA Assembly Master Mix into a doxycycline-inducible, PiggyBac vector, which was described in our previous publication.[28]

PiggyBac vectors for doxycycline-inducible expression of HaloTag-Ser/Cys arrays

Constructs for doxycycline-inducible HaloTag-Ser and HaloTag-Cys were generated by inserting the coding sequence for HaloTag protein whose C-terminal is fused to a flexible linker (GAPGSAGSAAGGSGA)[111] and to an array containing either 5 serines or 5 cysteines which are separated by a rigid linker (AEAAAKEAAAKA)[110] into a PiggyBac vector. Constructs were made using NEBuilder HiFi DNA Assembly Master Mix.

PiggyBac vectors for doxycycline inducible expression of AviTag-HaloTag-Cys and BirA

Constructs for doxycycline-inducible HaloTag-Ser and HaloTag-Cys were generated by inserting coding sequences for the constructs into PiggyBac vectors. The AviTag-Halo-Cys construct encodes the coding sequence for HaloTag-Cys construct described above with the AviTag peptide (GLNDIFEAQKIEWHE) with FLAG and HA tags all separated by flexible linkers (PGGSG) fused to the N-terminus. The BirA construct encodes a coding sequence for a human codon-optimized version of BirA with a C-terminal flexible linker (GAPGSAGSAAGGSGA) followed by a SNAP-tag and HA-tag. Constructs were made using NEBuilder HiFi DNA Assembly Master Mix.

Cell editing

Selection criteria for the studied endogenous proteins

We chose for study a plasma membrane receptor (insulin receptor, IR), a transcriptional cofactor (Mediator subunit MED1), a regulator of heterochromatin (heterochromatin protein HP1α), a component of the nucleolus (fibrillarin, FIB1) and a subunit of the mRNA splicing apparatus (serine and arginine-rich splicing factor 2, SRSF2) for multiple reasons. These proteins are well-studied and important regulators of diverse processes in cells (signaling, gene expression, gene silencing, rRNA biogenesis and splicing, respectively). The biological processes associated with these proteins have been shown to be dysregulated in prevalent syndromes. The expression level of these proteins in the liver is similar between healthy donors and patients with type 2 diabetes.[112] Previous studies have shown that the endogenous proteins can be successfully tagged with fluorescent probes.[28,44,103,111,113] When labeled with florescent probes, they retained their ability to concentrate in the proper locations in cells.[28,44,103,111,113] All these proteins have been reported to assemble into condensate compartments together with other biomolecules with shared functions.[28,44,49,53,113]

Endogenously tagged cell line generation

The IR-GFP cell line used here was generated in our previous study.[28] A CRISPR/Cas9 system is used to generate genetically modified HepG2 cell lines as previously performed.[28] 1×10^6 cells were transfected with 1.5 μg sgRNA-Cas9 plasmid and 1.5 μg of homology repair template using Lipofectamine 3000 (Invitrogen, L3000). 24 hours post-transfection, transfection media was replaced with fresh cell culture media (EMEM-FBS). To enrich for transfected cells, cells were sorted 72 hours after transfection based on the expression of mCherry fluorescent protein encoded from the sgRNA-Cas9 plasmid. mCherry positive cells were expanded for 1.5 to 2 weeks before a second sorting for the expression of GFP or HaloTag. To sort based on HaloTag expression, cells were cultured for 15 minutes with Janelia Fluor 585 (a gift of the Lavis Laboratory) prior to sorting. Cells were then expanded and the cell lines were validated by Western blot, PCR genotyping using Phusion polymerase (Thermo Fisher Scientific, F531S) and imaging experiments.

To generate the clonal cell line used in Figures 4H and 4I, after the second sort, single cells were plated into individual wells of a 96-well plate. The single cells were cultured for 1–1.5 months in conditioned media. To make conditioned media, HepG2 cells were first cultured in fresh media (EMEM-FBS) for 3 days and this media was subsequently harvested. Conditioned media was then made by mixing the harvested media 1:1 with fresh media and filter-sterilizing prior to use.

Genotyping PCR was performed according to the manufacturer's specifications, using the following primers:

IR_fwd: GGAGAATGTGCCCCTGGAC

IR_rev: TTGGTAACCAAACGAGTCCACCT

Doxycycline inducible expression cell line generation

A PiggyBac transposon system (Systems Biosciences) was used for stable integration. 1×10^6 wildtype HepG2 cells were plated in a 6-well plate and simultaneously transfected with 0.5 μg of the PiggyBac expression vector and 0.2 μg of a plasmid encoding PiggyBac transposase (gift of Jaenisch lab) using Lipofectamine 3000 (Invitrogen, L3000). 24 hours post-transfection, transfection media was replaced with fresh media, EMEM with 10% FBS. 72 hours post-transfection, the cells were treated with media containing 150 μg/mL hygromycin (Thermo Fisher Scientific, 10687-010) (for cells edited to express HaloTag-Cys, HaloTag-Ser, and AvTag-Halo-Cys) or 2 μg/mL puromycin (Millipore, P4512-1MLX10) (for cells edited to express BirA-SNAP). Selection media was refreshed every 3 days and un-transfected cells were also treated with hygromycin as a positive control, confirming the efficiency of selection. Typically, 7-10 days were required for the hygromycin to kill all the non-transfected HepG2 cells. For cells with doxycycline-inducible co-expression of AviTag-Halo-Cys and BirA-SNAP, additional sorting was applied to get cells with low expression of both proteins and minimized cell-to-cell expression variability when performing doxycycline induction: cells were treated with 10 ng/mL doxycycline overnight, followed by co-staining with 50 nM of Halo-JF549 and 50 nM SNAP-JF646 for 20 minutes and proceeding to FACS sorting.

Cell viability

Cell viability was measured by mixing 1:1 TrypanBlue (Invitrogen, T10282) with single cell suspension, then 10 μl of the TrypanBlue/cell mixture was loaded into Countess cell counting chamber slides (Invitrogen, 100078809) and viability was measured using the Countess 3 FL (Invitrogen). All samples were prepared in biological triplicate.

Cell treatments for HepG2

Insulin treatment

The cell plating and insulin treatment regime used in this study is the same as the one previously published.[28] Cells were seeded at a density of 32,000 cells/cm^2 onto 35-mm glass bottom dishes (MatTek Corporation, P35G-1.5-20-C). Starting the day after plating, cells were serum-starved for two days by washing the plates twice with EMEM media without FBS (EMEM) and maintaining the cells in EMEM for 48 hours. Then cells were treated with EMEM supplemented with 0.125% fatty acid-free BSA (Sigma-Aldrich, A8806-5G) ("EMEM-BSA") that contained either 1) 0.1 nM insulin (Sigma-Aldrich, I9278-5ML) or 2) 3nM insulin, which are the concentrations of insulin in the portal vein of healthy and insulin resistant patients.[46] The media was refreshed twice per day (every ~12 hours) for 3 days. This treatment regime produced either a baseline "normal" signaling state or a "pathogenic" elevated signaling state.[28] To ensure that the protein mobility was due to the cellular state and not due to differences in the concentration of insulin, insulin wash-outs were performed. Insulin wash-outs were performed by extensively washing cells with EMEM: the cells were washed

six times each with 2mL of EMEM, including three quick washes, two 5 min washes, and a 15 min wash at 37 °C. Cells were then acutely treated with 3 nM insulin for 5 minutes in EMEM-BSA at 37 °C with 5% CO_2 in a humidified incubator and then subjected to the desired assay.

H_2O_2 treatment

For experiments in Figures 3E, 3F, S4C, and S4D, cells were seeded at a density of 32,000 cells/cm^2, serum-starved for two days as described above. Then cells were treated with EMEM-BSA containing 0.1 nM insulin for three days refreshing the media containing insulin twice per day (every ~12 hours). Following a quick wash in EMEM, cells were treated with 0 mM or 7.5 mM H_2O_2 (Sigma-Aldrich, H1009) in EMEM for 5 minutes. This treatment regime was selected because it lead to a similar degree of oxidative stress as pathogenic insulin (see Figures 3B and 3C and "metabolomics for quantification of GSSG and GSH ratio" below) and minimizes potential indirect effects of extended H_2O_2 treatment. Cells were then subjected to the desired assay. For the H_2O_2 titration experiment in Figure 5, cells were seeded at a density of 100,000 cells/cm^2, serum-starved for two days, followed by treating with 0, 1, 3, 8, or 20 mM H_2O_2 in EMEM for 5 minutes before proceeding to imaging. For Figure S6A, cells were plated at a density of 56,000 cells/cm^2. When cells reached 80-90% confluency, cells were washed with EMEM once for 30 minutes before treating the cells with 0, 0.1, 1 or 20 mM H_2O_2 for 5-10 minutes. Cells were then collected for western blot. For Figure S7D, cells were cultured in EMEM for 2 days and in EMEM BSA containing 0.1nM insulin for 2 days. Following washes with EMEM as described above, cells were treated with 20mM H_2O_2 for 30 minutes and then stimulated with 3nM insulin in EMEM-BSA for 5 minutes at 37 °C with 5% CO_2 in a humidified incubator. Cells were then processed for immunofluorescence.

N-acetyl cysteine (NAC) treatment

Cells were seeded at a density of 32,000 cells/cm^2, serum-starved for two days as described above. Following serum starvation, the cells were treated with 1) EMEM-BSA containing 3 nM insulin for two days and then with 2) EMEM-BSA containing 3 nM insulin and 1 mM NAC (Sigma-Aldrich, A9165-25G) for one day, refreshing the media twice per day (every ~12 hours). We treated the cells with 1mM NAC for 24 hours, because it is reported as a clinically relevant concentration[114] and treating HepG2 cells with 1mM NAC for 24 hours partially restores insulin signaling.[28] Insulin washouts and final stimulation was performed as described above. For NAC treatments of cells expressing IR-Y1361C mutant protein, cells were seeded at a density of 32,000 cells/cm^2 in 35mm glass-bottom dishes, serum-starved for 16 hours and treated with EMEM-BSA containing 0.1 nM insulin and 1 mM NAC for two days refreshing the media twice per day (every ~12 hours). Insulin washouts and final stimulation was performed as described above and cells were then subjected to the desired assay.

NEM with H_2O_2 treatment

Cells were seeded at a density of 55,000 cells/cm^2 in 35 mm glass-bottom imaging dishes (Mattek, P35G-1.5-20-C) and the following day were washed once with EMEM and then serum-starved in 2 ml of EMEM for 24 hours as described above. 100 mM N-ethyl maleimide (NEM) (Thermo Fisher Scientific, 156100500) stock solution was freshly prepared in sterile water prior to experiments. A final concentration of 0 or 10 μM NEM in EMEM was added to cells and incubated at 37°C, 5% CO_2 for 10 minutes, then the cells were treated with H_2O_2 (Sigma-Aldrich, H1009) to a final concentration of 7.5 mM and imaged immediately. Imaging did not proceed longer than 10 minutes to limit secondary effects from extended hydrogen peroxide treatment.

High glucose treatment

Cells were seeded at a density of 100,000 cells/cm^2, and then serum-starved for 16 hours. Cells were then cultured in media containing high glucose concentrations (EMEM supplemented with 33 mM of glucose, Sigma-Aldrich, G8270) or in media containing physiological concentrations of glucose (EMEM supplemented with 33 mM of mannitol, Sigma-Aldrich, M1902) for 12 hours. EMEM media provides physiological concentrations of glucose, and mannitol is used to ensure cells are under similar osmolarity conditions as the high glucose condition. Cells were then subjected to the desired assay.

High fat treatment

Cells were seeded at a density of 32,000 cells/cm^2, and then serum-starved for two days as described above. Cells were then cultured for two days with either EMEM supplemented with fatty acids and BSA (EMEM-HF) or with EMEM-BSA as a control. For EMEM-HF, a 50x stock solution is first made by supplementing EMEM with the following components to the indicated concentrations: 6.25% fatty acid-free BSA (Sigma-Aldrich, A8806-5G), 2.25 mM oleic acid (Sigma-Aldrich, O7501), and 1.5 mM palmitic acid (Sigma-Aldrich, P9767). This mixture was then incubated at 37°C for 1 hour with constant shaking in a thermomixer. The stock solution was then diluted 1:50 for use in experiments resulting in a final concentration of 0.125% BSA, 45 mM oleic acid and 30 mM palmitic acid for cell treatments. Media was refreshed twice a day (every ~12 hours). Cells were then subjected to the desired assay.

Tumor necrosis factor alpha (TNFα) treatments

Cells were seeded at a density of 32,000 cells/cm^2, and then serum-starved for two days as described above. Cells were then treated with EMEM-BSA media with/without 10 ng/ml Human TNF-α Recombinant Protein (Thermo Fisher Scientific, PHC3016) for two days, refreshing the media twice per day (every ~12 hours). The cells were then subjected to the desired assay.

Etoposide treatment

Cells were seeded at a density of 100,000 cells/cm^2 for etoposide treatment and 10,000 cells/cm^2 for DMSO control. The differences in seeding densities were required to ensure both sets of cells eventually reached similar levels of confluency, as etoposide blocks cell proliferation. Cells were treated with EMEM-FBS media containing 1) 1.5 μM etoposide (Thermo Scientific Chemicals, J63651, reconstituted in DMSO) or 2) the same volume of DMSO (Sigma-Aldrich, D2438) as a DMSO control. After 3 days, cells were treated again with 1.5μM etoposide or DMSO for 3 more days. Cells were then subjected to the desired assay.

Lipopolysaccharide (LPS) treatment

Cells were seeded at a density of 100,000 cells/cm^2, and then serum-starved for 16 hours. Cells were then cultured in EMEM containing 1 μg/ml of LPS (Sigma-Aldrich, L2630) for 24 hours. Cells were then subjected to the desired assay.

N-acetyl-p-benzoquinone imine (NAPQI) treatment

Cells were seeded at a density of 32,000 cells/cm^2, and then serum-starved for 2 days. Cells were then treated with EMEM media containing 150 mM NAPQI (Sigma-Aldrich, A7300-1mg) in DMSO or with EMEM media containing DMSO as a control for 15 minutes. Cells were then subjected to the desired assay.

BirA/Avi Assay

Cells were treated with the insulin treatment described above. For each treatment with insulin besides the acute stimulation, 1 ng/ml doxycycline was added. 10 μM biotin (Millipore, B4501) was added to the acute insulin treatment and cells were incubated at 37°C 5% CO_2 for 5 minutes and subjected to the desired assay.

Cell treatments for C2C12

Insulin treatment

Cells were seeded at a density of 100,000 cells/cm^2 onto 35-mm glass bottom dishes (MatTek Corporation, P35G-1.5-20-C) for imaging. Starting the day after plating, cells were serum-starved for two days by washing the plates twice with DMEM media without FBS (DMEM) and maintaining the cells in DMEM for 48 hours. Then cells were treated with DMEM supplemented with 0.125% fatty acid-free BSA (Sigma-Aldrich, A8806-5G) (“DMEM-BSA”) that contained either 1) 0.1 nM insulin (Sigma-Aldrich, I9278-5ML) or 2) 3nM insulin. The media containing insulin was refreshed twice per day (every ∼12 hours) for two days. This treatment regime produced either a baseline “normal” signaling state or a “pathogenic” elevated signaling state.[28] Right before imaging, insulin washouts were performed as follows: in total six washes with 2mL of DMEM each, including three quick washes, two 5 min washes, and a 15 min wash at 37 °C. Cells were then acutely treated with 3 nM insulin for 5 minutes in DMEM-BSA at 37 °C with 5% CO2 in a humidified incubator and then subjected to the desired assay.

High glucose treatment

Cells were seeded at a density of 100,000 cells/cm^2, and then serum-starved for 16 hours. Cells were then cultured in media containing high glucose concentrations (DMEM supplemented with 33 mM of glucose, Sigma-Aldrich, G8270) or in media containing physiological concentrations of glucose (DMEM supplemented with 33mM of mannitol, Sigma-Aldrich, M1902) for 12 hours. DMEM media provides physiological concentrations of glucose, and mannitol is used to ensure cells are under similar osmolarity conditions as the high glucose condition. Cells were then subjected to the desired assay.

High fat treatment

Cells were seeded at a density of 100,000 cells/cm^2. After one day, cells were then cultured for one day with either DMEM-FBS supplemented with 200 μM palmitic acid (Sigma-Aldrich, P9767) (DMEM-HF) or with DMEM-FBS supplemented with 200 μM BSA as a control. For DMEM-HF, a 50x stock solution was first made by supplementing DMEM with the following components to the indicated concentrations: 6.25% fatty acid-free BSA (Sigma-Aldrich, A8806-5G) and 10 μM palmitic acid (Sigma-Aldrich, P9767). This mixture was then incubated at 37°C for 1 hour with constant shaking in a thermomixer. The stock solution was then diluted 1:50 for use in experiments resulting in a final concentration of 0.125% BSA, 200 μM palmitic acid for cell treatments. Cells were then subjected to the desired assay.

Tumor necrosis factor alpha (TNFα) treatment

Cells were seeded at a density of 100,000 cells/cm^2, and then serum-starved for two days as described above. Cells were then treated with DMEM-BSA media with/without 10 ng/ml Human TNF-α Recombinant Protein (Thermo Fisher Scientific, PHC3016) for two days, refreshing the media twice per day (every ∼12 hours). The cells were then subjected to the desired assay.

Etoposide treatment

Cells were seeded at a density of 100,000 cells/cm^2 for etoposide treatment and 1,000 cells/cm^2 for DMSO control. The differences in seeding densities were required to ensure both sets of cells eventually reached similar levels of confluency, as etoposide blocks cell proliferation. Cells were treated with DMEM-FBS media containing 1) 1.5 μM etoposide (Thermo Scientific Chemicals, J63651, reconstituted as 10mM in DMSO) or 2) the same volume of DMSO (Sigma-Aldrich, D2438) as a DMSO control. After 3 days, cells were treated again with 1.5μM etoposide or DMSO control for 3 more days. Cells were then subjected to the desired assay.

Lipopolysaccharide (LPS) treatment

Cells were seeded at a density of 100,000 cells/cm^2, and then serum-starved for 16 hours. Cells were then cultured in DMEM containing 1 μg/ml of LPS (Sigma-Aldrich, L2630) for 24 hours. Cells were then subjected to the desired assay.

N-acetyl-p-benzoquinone imine (NAPQI) treatment

Cells were seeded at a density of 100,000 cells/cm^2, and then serum-starved for 2 days. Cells were then treated with DMEM media containing 150 μM NAPQI (Sigma-Aldrich, A7300-1mg) in DMSO or DMSO as a control for 15 minutes. Cells were then subjected to the desired assay.

Live-cell imaging experiments: general setup

General imaging conditions

Cells were plated on 35-mm glass bottom dishes (MatTek Corporation, P35G-1.5-20-C). For imaging doxycycline inducible proteins, 0.1 μg/ml of doxycycline was added to the media 8-12 hours prior to imaging. Cells were imaged for no longer than 10 minutes inside an incubation chamber supplemented with warmed (37°C) humidified air and with 5% CO_2. For exogenous GFP or HaloTag visualization, the cells were also stained with 1:20,000 of Hoechst 33342 (Thermo Scientific, 62249) for 10 minutes to stain the nuclei before imaging.

Live-cell super-resolution microscopy

ZEISS LSM 980 with Airyscan 2 was used to acquire the super-resolution images of GFP-/HaloTag-tagged proteins. Cells were imaged with a ZEISS incubation system that stably maintained the samples at 37°C with 5% CO_2 and humidified air. A 63X objective with oil immersion was used. For GFP-tagged proteins, 488 nm laser was used for excitation. For Halo-tagged proteins, cells were first incubated with media containing 100 nM Janelia Fluor 549 (Halo-JF549, Promega, GA1110) for 15 minutes. The cells were then washed with fresh media and then cultured at 37°C with 5% CO_2 for 10 minutes before imaging with 561 nm laser excitation and the mCherry filter for emission. Due to the various expression levels of different proteins, the laser power was adjusted for each protein, such that the brightest pixels remained below the saturated levels of the detection range (maximum brightness = 255 for 8-bit images). Following raw image acquisition, Airyscan super-resolution processing was performed via ZEN Blue.

Fluorescence recovery after photobleaching (FRAP)

ZEISS LSM 980 with 63X objective, oil immersion was used to perform FRAP experiments on GFP-tagged proteins in live cells. The acquisition mode, laser power, time interval between frames, total number of frames, and other FRAP-specific settings were customized for each protein of interest (POI) such that each experiment would satisfy four criteria: (1) have sufficient signal, (2) have sufficient duration to capture recovery, (3) have sufficient temporal resolution, (4) endure minimal photobleaching throughout the time course. Detailed configurations for different protein targets are summarized in Table S5. For each single FRAP acquisition course, several frames were first recorded to establish pre-bleach levels of signal, followed by photobleaching with 100% laser power of a 2μm-by-2μm square region. For insulin receptor, this square region contained a portion of the plasma membrane. For MED1, HP1α, and SRSF2, this square region contained an area of the relevant punctate high signal (a condensate). For FIB1, this square region overlapped, but did not completely cover the nucleolus. For GFP, this square region was either randomly sampled within the nucleus or randomly sampled within the cytoplasm. The number of bleaching cycles is reported in Table S5. After photobleaching, fluorescence recovery was recorded over time. Raw image series were processed via ZEN Blue (2D Airyscan processing), followed by drift correction using a cross-correlation algorithm. Averaged intensity measurements from an unbleached region were further used to correct for the photobleaching occurring during the image acquisition.

Statistical analysis was performed with the Statistics and Machine Learning Toolbox of MATLAB. A two-tailed student's *t*-test was used to generate p-values comparing timepoints at the later end of recovery curves, at which point recovery intensities had stabilized. The number of timepoints (n) for each comparison was ~6-13% of the total number of timepoints collected in the recovery curve (the number of time points considered is specified in Table S5). All FRAP experiments were performed twice using a total of 4 biologically independent samples. Each dish was imaged for no more than ten minutes to minimize secondary effects of extended treatment.

Single particle tracking (SPT)

ZEISS Elyra 7 with 63X objective, oil immersion was used to perform SPT experiments on Halo-tagged for all proteins, except AviTag-Halo-Cys and BirA-SNAP, in live cells. ONI Nanoimager with 100X objective, oil immersion was used to perform SPT experiments for AviTag-Halo-Cys and BirA-SNAP in live cells. Cells were co-stained with two Halo dyes: one used for tracking individual molecules of a protein and the other for visualizing the bulk distribution of the protein. After staining, cells were washed by incubating with fresh media without dyes for at least 10 minutes. HILO illumination was used during the tracking. The detailed sample preparations and configurations of SPT for different proteins are summarized in Table S5. For the tracking of AviTag-Halo-Cys and BirA-SNAP, cells were first incubated with media containing 0.1 nM Janelia Fluor 549-Halo and 0.1 nM Janelia Fluor 646-SNAP (a generous gift from Luke Lavis Lab at Janelia Farm Research Campus) for 20 minutes and molecules were tracked at 100 Hz acquisition rate with 35% laser power. There are four major steps in the SPT analysis to obtain single molecule trajectories: pixelwise peak detection, subpixel localization of the peaks, reconnection of the peaks (to construct trajectories) and validation of trajectories. For the first three steps, point spread functions (PSFs) from single molecules were detected, subpixel-localized, and reconnected with custom code in MATLAB based on the published multiple-target tracing (MTT) tool.[115] During the pixelwise peak detection step, for each pixel, two hypotheses H_0 and H_1 were compared based on a generalized likelihood ratio test, where H_0 defines the non-presence of particles and H_1 the presence of a particle at the center of the pixel. Valid peaks were identified with a constant false alarm rate ($\approx 1.5\times10^{-6}$). Additional peaks were identified with a B-spline wavelet filter.[116] The subpixel localization of the peaks was performed by maximizing the likelihood of the PSF to match the local intensity distribution of a 7x7 pixel area using Gauss-Newton regression. The reconnection of the peaks to construct trajectories was performed based on the multiple-target reconnection as described in MTT,[115] with the prior maximum diffusion coefficients, the disappearance probability for blinking and maximum number of disappearance frames summarized in Table S5. A set of reconnected peaks comprises a trajectory. Validation of trajectories for those occurring in the relevant biological compartments was performed using bulk distribution or nuclear stain as a reference. For insulin receptors, the plasma membranes were manually selected by drawing polygons via MATLAB; for other proteins of interest, nuclei or nucleoli regions were labeled by a deep learning based algorithm Cellpose.[104]

Live-cell imaging experiments: analysis and additional validation

Inferring mobility from FRAP courses

With FRAP, we investigated protein mobility in cell models of disease at the length and time scales of 1-2 microns and (tens of) seconds, with the additional question of whether protein mobility was altered both inside and outside of condensates. For the proteins that could be reliably assigned to be within or outside of condensates during image acquisition (MED1, HP1α, FIB1 and SRSF2), a square region containing both the condensate(s) and the surrounding dilute phase was imaged, allowing separate FRAP analyses both inside and outside of the condensates. The areas inside the condensates (condensed region) and outside the condensates (dilute regions) were differentiated by custom code in MATLAB by fitting the cumulative distribution of pixel-wise intensities of each FRAP region to a two-step function, with the first step identifying the low-intensity pixels in the nucleus (the dilute region) and the second step by identifying the high-intensity pixels with enriched fluorescent signal in the nucleus (the condensed region). For FRAP outside the condensates, the dilute region was selected for analysis, and for FRAP inside the condensates, the condensed phase was selected for analysis. For insulin receptor (IR), due to the rapid movement of IR condensates, we could not perform reliable assignments of the condensate-occupied pixels throughout a FRAP acquisition course. Instead, the fluorescence signal analysis was limited to the plasma membrane (where most signals are located), which was manually selected in ZEN Blue. For GFP alone, the pixels inside the entire 2μm-by-2μm photobleached region were selected for fluorescence signal analysis as GFP alone does not form condensates. For each frame of each FRAP course, the average intensity of selected pixels was calculated. The average intensities from different frames were further normalized through the following linear transformation: the averaged intensity of pre-photobleaching frames was set to 1, while the intensity right after photobleaching was set to 0. This resulted in a FRAP curve for each independent photobleaching experiment. A single average FRAP curve from all replicate samples was obtained by plotting the mean normalized pixel intensity and SEM for each timepoint. To evaluate the difference of protein mobility between any two conditions, the maximum extent of recovery at the end of the recorded time window was compared. For this comparison, a two-tailed student's t-test was used to calculate statistical significance. Data points used for the comparison were chosen by selecting time points where signal recovery was approaching an apparent plateau (listed in Table S5) and aggregating those signal intensities.

Statistical analysis was performed with the Statistics and Machine Learning Toolbox of MATLAB. A two-tailed student's *t*-test was used to generate p-values comparing timepoints at the later end of recovery curves, at which point recovery intensities had stabilized. The number of timepoints (n) for each comparison was ~6-13% of the total number of timepoints collected in the recovery curve (the number of time points considered is specified in Table S5). All FRAP experiments were performed twice using a total of 4 biologically independent samples. Each dish was imaged for no more than ten minutes to minimize secondary effects of extended treatment.

Inferring mobility from 2D SPT trajectories

We investigated protein mobility in cell models of disease at the length and time scales of (sub)micron and (sub)second, and focused on the question of whether apparent diffusion rates are reduced under pathogenic conditions. We used a wide-field microscope to measure planar (XY) movement at a desired, feasible length/time scale. The use of 2D projections to measure apparent diffusion coefficient (*D*) has been a widely used approach,[117–120] given the assumption that the molecules diffuse isotropically along the three-dimensional axes X, Y and Z. This assumption is supported by the observation that a similar apparent diffusion coefficient was observed when Sox2–a nuclear protein–was tracked in 3D ($D \approx 2.5 \mu m^2/s$[121]) and 2D projection in XY ($D \approx 2.8 \mu m^2/s$[118]). To provide a scalar measurement of the molecular movement we infer from a given SPT trajectory, we calculate an apparent diffusion coefficient for each trajectory. This value *D* is derived from the relationship between the mean square displacement (MSD) versus timelag (τ). Only trajectories with at least 5 reconnected peaks were selected. For trajectories with more than 20 reconnected peaks, only the first 20 peaks were used for estimating the *D*. A linear regression between MSD and timelag with an additional zero-order term (localization error due to limited spatial resolution) was used to fit the apparent diffusion coefficient in two dimensions: $\mathrm{MSD}(\tau) = 4D\tau + \sigma^2$. At this point, we obtained the fitted *D* for each trajectory, which was a reliable estimation only if 1) the *D* was above the effective magnitude caused by localization error, and 2) the fitting noise was relatively low. To filter for reliable *D* above the localization uncertainty, molecules with $D \geq 0.01\ \mu m^2/s$ for endogenous proteins and $D \geq 0.1\ \mu m^2/s$ for exogenous HaloTag were selected for the analysis (drop-off rate $\simeq$ 10-30%), To filter for reliable *D* with low fitting noise, molecules whose fitting residual was below the MSD of one-frame timelag were selected for the analysis (drop-off rate $\simeq$ 5%-10%). These two filters were sequentially applied to obtain the final well-fitted trajectories. Mann-Whitney test was used to evaluate the statistical significance between the diffusion coefficients in different conditions. For HepG2 cells, all SPT experiments were performed in 4 biologically independent samples, for C2C12 cells, all SPT experiments were performed in 2 biologically independent samples. In this work, we are using mobility to describe the transit of individual molecules or ensembles of molecules through space over a given unit time. Such movement is likely to be the net effect of diverse forces within the cell. In this work, the duration of tracking mostly ranges from 0.02s-0.1s, with a temporal resolution of 4ms-10ms, and spatial resolution of 30nm-80nm.

Evaluation of the comparability between FRAP and SPT – general setup

There are two biophysical parameters inferred from both FRAP and SPT that can be used to address how comparable the values generated by these two methods are: (1) fraction of immobile molecules; (2) apparent diffusion coefficient of mobile molecules. For (1), we used five endogenously tagged proteins (IR, MED1, HP1α, FIB1, and SRSF2) which are known to have a "bound state" and thus a putative immobile fraction of molecules; For (2), we used exogenously expressed GFP vs HaloTag with the assumption that these proteins demonstrate homogeneous apparent diffusion coefficients throughout the nucleoplasm.

Evaluation via the fraction of immobile molecules

We used SpotOn[118] to evaluate the fraction of immobile molecules by SPT, which requires two hyperparameters: 1) the total number of diffusivity states and 2) the axial detection range. An estimate of the total number of diffusivity states is achieved by identifying the minimum number of Gaussian functions needed to sufficiently fit the log$D$ distribution of individual molecules (Figure S2A).[120] The fitting residual was plotted as a function of the number of Gaussian functions (N) tested to perform the fitting, and the minimum number of Gaussian functions needed was the inflection point of the residual-N relation. We found MED1 can be well fitted by 2 states, and other targets are well fitted by three states. An estimate of the axial detection range is achieved by examining a z-stack scan of fixed cells with sparsely labeled PAJF549 molecules to establish a limit of expectations for focal depth within which a single molecule can be consecutively tracked. We concluded that the focal depth (dz) peaked at ~900nm for our specific setup (Figure S2B). These values were used in SpotOn to estimate of the fraction of immobile molecules by SPT (Figure S2C).

For FRAP datasets, we fitted the normalized recovery curve to the following equation:

$$I(t) = f \cdot \left(1 - 2^{-t/\tau}\right),$$

Where $1 - f$ would be the immobile fraction. The fraction of immobile molecules estimated via two methods are indeed comparable (Figure S2C): FIB1 shows the highest immobile fraction among the five proteins tested; IR, HP1α, and SRSF2 showed relatively lower immobile fractions in both SPT and FRAP. The immobile fractions estimated by FRAP were slightly lower compared to those estimated by SPT. Given that SPT can capture stable immobile events, and transient immobile events in a timescale as short as $\sim 10^{-2}$ s, while FRAP is only sensitive to intermediate/long-term immobile events in a timescale of $\sim 10^{1}$ s, this could explain why the immobile fractions estimated by FRAP are consistently lower.

Evaluation via the apparent diffusion coefficient of mobile molecules

The HaloTag tagged with a JF646 molecule (~34kDa in total) and GFP (~27kDa) have comparable protein size; we thus expect that the intrinsic diffusion coefficients of these two proteins should be similar. For SPT, we estimated the apparent diffusion coefficient of HaloTag by calculating the average apparent diffusion coefficient of mobile molecules. For FRAP, we estimated the apparent diffusion coefficient of GFP by matching the experimental FRAP data to a theoretical model of the diffusion process within a photobleached area. We modeled the theoretical diffusion process of a photobleached region ($l \times l$) as the following partial derivative equation (PDE) problem:

$$\frac{\partial u}{\partial t} = D\left(\frac{\partial^2 u}{\partial x^2} + \frac{\partial^2 u}{\partial y^2}\right), 0 < x < l, 0 < y < l, t > 0,$$

$$u|_{x=0} = 0,\ u|_{x=l} = 0, 0 \le y \le l, t \ge 0,$$

$$u|_{y=0} = 0,\ u|_{y=l} = 0, 0 \le x \le l, t \ge 0,$$

$$u|_{t=0} = 1 - \phi(x,y), 0 \le x \le l, 0 \le y \le l.$$

In this PDE problem, $u(x,y,t)$ is the normalized density of photobleached molecules of a certain pixel (x,y) at certain time t. $x,y = 0$ *or* l are boundaries. $\phi(x,y)$ is the normalized pixelwise intensity (i.e., normalized density of intact molecules) right after photobleach ($t = 0$), thus $1 - \phi$ is the density of photobleached molecules at $t = 0$ (the total normalized intact molecules plus photobleached molecules always equals 1 within each pixel). In the spirit of separation of variables, one general analytical solution that satisfied the boundary conditions was derived as:

$$u(x,y,t) = \sum_{n,m=1}^{\infty} A_{nm} \times \sin\frac{n\pi}{l}x \times \sin\frac{m\pi}{l}y \times \exp\left\{-\left[\left(\frac{n\pi}{l}\right)^2 + \left(\frac{m\pi}{l}\right)^2\right]Dt\right\},$$

Where the coefficients of different modes were computed as:

$$A_{nm} = \frac{4}{l^2}\int\int_0^l (1 - \phi(x,y)) \times \sin\frac{n\pi}{l}x \times \sin\frac{m\pi}{l}y dx dy.$$

The D is determined when the 2-norm residual of the $u(x,y,t)$ throughout the whole FRAP process between the experimental measurement and the theoretical prediction are minimized. The calculations were done by custom MATLAB code. The diffusion coefficient of HaloTag estimated from SPT is 5.3±0.2 $\mu m^2/s$, and the diffusion coefficient of GFP estimated from FRAP is ~6 $\mu m^2/s$

(Figure S2D). Given that the relation between the molecular weight (M) and diffusion coefficient is $D \sim M^{-0.33}$,[122] the diffusion coefficient of a "weighted GFP" (~34kDa) estimated from FRAP would have been ~5.5 $\mu m^2/s$. Therefore, the apparent diffusion coefficient estimated via two methods are comparable indeed.

Estimation of the localization uncertainty

To experimentally derive a lower bound for apparent diffusion constants that indicate molecules that are moving, we examined a fixed sample of cells with sparsely labeled HaloTag-PAJF549 molecules. As these molecules are fixed, diffusion constants derived would theoretically represent "no movement". The distribution of apparent diffusion coefficient fitted from individual molecules in fixed sample centered around D~0.01 $\mu m^2/s$ (Figure S2E), and this pseudo diffusivity is due to the localization uncertainty of single molecules at each frame. Therefore, we used 0.01 $\mu m^2/s$ as the lower bound cutoff when filtering for truly mobile molecules for endogenous protein targets based on the limitation of the localization uncertainty. As for exogenously expressed HaloTag alone, because most molecules are diffusive, we can apply a higher cutoff (D>0.1 $\mu m^2/s$) to select mobile molecules in order to eliminate any false positive mobile molecules without increasing the chance of false negative elimination (Figure S2F).

Validation of reconnecting during trajectory reconstruction

There are two main sources of error when reconstructing a trajectory from localizations: too stringent prior maximum allowed diffusion coefficient (D_{max}), or too great of localization density (Figures S2G–S2I). If D_{max} is smaller than the typical diffusivity of the protein of interest, it will result in an early stop of reconnecting peaks of signal of the same molecule (Figure S2G), and the estimated apparent diffusion coefficient will hit a ceiling set by D_{max} (the estimated apparent diffusion coefficient is artificially low). To prevent this issue, the D_{max} we chose when reconnecting sequential peaks (Table S5) is much larger than the apparent diffusion coefficients estimated from the final trajectories. It should be noted that for all D_{max}, the tracking process will still stop at some point, mainly due to either the photobleach of the dye molecule, or the molecule moving out of the focus (Figure S2H). If the localization density per frame is too great, there will be an increased likelihood that the trajectories of two different molecules form an "ambiguous connection". In this situation, we expect to see an increase in the average number of jumps (connection between two consecutive peaks) per trajectory (Figure S2I). To determine a threshold density that would minimize ambiguous connections in our experiments, we generated IR-HaloTag SPT data with different peak density per frame, followed by reconnecting the peaks with the prior D_{max}=6 $\mu m^2/s$. We found that the average number of jumps per trajectory starts to increase with peak density when the peak density is above 0.01 μm^2/frame, and we ensured peak densities of our experiments were always below this threshold density (Figure S2J). Therefore, we concluded that the prior D_{max} chosen for reconnecting is large enough to capture consecutive jumps for the same molecule, and the peak densities of our actual experiments are low enough to avoid significant "ambiguous connection" given the prior D_{max}.

Estimation of the false positive identifications of trajectories in SPT

The sources of false positive identifications of proteins in SPT include pixel noise, auto-fluorescence, and non-specific dye staining (restricted to PAJF549). The control experiments are summarized in Table S6. The overall rate of false positive identification of trajectories is either ~5% (for JF646 staining) and ~12% (for PAJF549 staining) at maximum. Therefore, we concluded that the SPT dataset of the actual experiments are dominated by trajectories from real proteins of interest.

Diffusion coefficient comparisons based on bulk population or cell-based analysis of single particle trajectories

Diffusion coefficients were calculated as described above for each trajectory in the bulk population of the trajectories. Trajectories were then grouped by cell. Diffusion coefficients were calculated as described above for each trajectory within a single cell, and the median diffusion coefficient was selected for cell-based analysis. This process was repeated for each set of trajectories per cell. Results using the diffusion coefficients for the bulk population were compared to results using median diffusion coefficients from a cell-level analysis to see if cell-level analysis would alter the interpretation of our results. Our results are consistent using both approaches (Figure S2K).

Quantification of condensate properties

Three condensate properties were evaluated in both normal and pathogenic conditions: (1) number of condensates per cell in the focal plane, (2) condensate size in diameter, and (3) the partition ratio, which can be defined as the relative enrichment of the intensity inside the condensate versus outside the condensate. Live-cell super-resolution images taken by ZEISS LSM 980 with Airyscan 2 were used for such quantifications of GFP-tagged proteins.

The first step is to identify/segment puncta. We implemented two approaches to identify/segment puncta depending on the size, morphology, and distribution of the protein condensates. Insulin receptor (IR), MED1 and FIB1 have relatively small condensates (less than ten pixels in diameter), with a round shape and compact distribution, thus the Laplacian of Gaussian (LoG) Blob Detection (sigma = 200nm, 500nm, and 450nm for IR, MED1 and FIB1, respectively) was applied to the images (MATLAB code source: Jason Klebes, 2024. LoG Blob, GitHub), and puncta were identified with the quality filter set to 0.2. Additional intensity filters and partition ratio filters were applied to call puncta, such that there was high agreement between auto-identified puncta and puncta called by a trained eye. HP1α and SRSF2 have varying condensate sizes (ranging from several pixels to more than ten pixels in diameter), with an ellipse or irregular shape and dispersed distribution, thus the images were background-subtracted with a median filter (filter size = 2μm), followed by feature segmentation with Cellpose[104]—an AI-based segmentation tool—with the "cytoplasm" model (feature dimension to be recognized = 1μm) to obtain the punctum features.

The second step is to quantify the three condensate properties of the identified puncta. To quantify the number of puncta in each cell, the regions where puncta could be detected per cell were defined based on the GFP signal and the detected puncta in each cell

were counted. To measure the condensate size, the full-width half-maximum was used as an estimator of IR, MED1 and FIB1 punctum diameters. To measure the condensate size of HP1α and SRSF2, the area of each punctum feature segmented by Cellpose was covered to an effective diameter with the formula: $d = 2*(area/\pi)^{0.5}$. To quantify the partition ratio,[123] the intensity inside the puncta was divided by the intensity of the local dilute phase. The intensity of the local dilute phase for the plasma membrane was used for IR, and the intensity of the local dilute phase of the nucleoplasm was used for the rest of the proteins.

Western Blotting

Protein preparation

HepG2 cells were treated according to the specified treatment protocol, then the media was aspirated off and cells were washed once with ice-cold PBS (Gibco, 10010-023) on ice. The PBS was then removed and Cell Lytic M (Sigma-Aldrich, C2978) supplemented with protease and phosphatase inhibitors (Sigma-Aldrich, 11873580001 and 4906837001) was added to each well to lyse the cells. The cells were scraped with a plastic cell scraper, and the lysates were transferred to a 1.5 ml eppendorf tube and allowed to rotate on a rotator for 15 minutes at 4°C. For proteins that required sheering of DNA to be accurately measured by Western blot (MED1, HP1α, FIB1, SRSF2), the lysates were sonicated in 1.5 ml Eppendorf tubes on ice water (15 seconds on, 20 seconds off, 30% amplitude, for 3 cycles, Fisher Scientific, FB120 Model CL-18) and then centrifuged at 12,000 x g for 15 minutes. The supernatant was transferred to a fresh 1.5 ml tube and the protein concentration was quantified using a BCA Protein Assay Kit (Life Technologies, 23250) according to the manufacturer's instructions.

Preparations of western blot samples

For samples prepared in Figures 6E, 6F, S1, and S6A (blot with DTT, right side), dithiothreitol (DTT) and XT Sample Buffer 4x (BioRad, 1610791) were added to the purified proteins in reaction buffer or protein lysates to final concentrations of 100mM and 1x, respectively and boiled at 95°C for 5 minutes. For western blot in non-reducing conditions, DTT was not added. For samples in Figure 6K, 2-mercaptoethanol and Native Sample Buffer (BioRad, 1610738) were added to the protein lysate to final concentrations of 2.5% and 1x, respectively, boiled for 5 minutes at 95°C and allowed to cool completely before addition of streptavidin (Invitrogen, 43-430-2) to a final concentration of 10μM to cause a shift in molecular weight of proteins that were biotinylated by BirA.

Running western blot samples

5-35 μg of proteins were separated on 10% or 4-12% Criterion™ XT Bis-Tris Protein Gel (BioRad, 3450112, 3450125) in XT MOPS running buffer (Bio-Rad Laboratories, 1610788) at 100 V. Proteins were transferred to a 0.45-μm PVDF membrane (Millipore, IPVH00010) in ice-cold transfer buffer (25 mM Tris, 192 mM glycine, 20% methanol) at 300 mA for 2 hours at 4 °C. Membranes were blocked in either 5% nonfat milk (LabScientific, M0842) dissolved in TBST (2% Tris-HCl pH 8.0, 1.3% 5 M NaCl, 0.05% Tween 20) or 5% BSA (VWR, 102643-516) in TBST for 1 hours at room temperature. Membranes were then incubated overnight at 4°C with primary antibodies (list below) diluted in 5% nonfat milk in TBST or 5% BSA in TBST. Membranes were then washed three times in TBST for 5 minutes at room temperature and then incubated with donkey anti-rabbit IgG (Cytiva Life Sciences, NA934-1ML, 1:10,000 dilution) or sheep anti-mouse IgG (Cytiva Life Sciences, NXA931V, 1:10,000 dilution) diluted in 5% nonfat milk in TBST for 1 hours at room temperature. Membranes were washed three times for 10 minutes in TBST. Membranes were developed with ECL substrate (Millipore, WBKL20500) and imaged using a CCD camera (BIO RAD, 1708265). The "analyze gel" tool on Fiji/ImageJ v2.1.0/153c was used to quantify immunoblot signal. A two-tailed student's t-test was used to generate p-values. Statistical analysis was performed using Prism Version 9.4.0 (GraphPad, La Jolla, CA).

Primary antibodies for Western blotting:

Anti-insulin receptor (Cell Signaling, 3025, dilution 1:1000)
Anti-MED1 (Bethyl, A300-793A, dilution 1:1000)
Anti-HP1α (Abcam, ab109028, dilution 1:1000)
Anti-FIB1 (Abcam, ab5821, dilution 1:1000)
Anti-SRSF2 (Thermo Fisher, PA5-12402, dilution 1:1000)
Anti-b-actin (Sigma-Aldrich, A5441, dilution 1:10,000)
Anti-H3 (Cell Signaling, 4499, dilution 1:1000)
Anti-HA (Cell Signaling, 3724, dilution 1:1000)
Anti-pIRS1 (Cell Signaling, 3070, dilution 1:1000)
Anti-IRS1 (Cell Signaling, 2382, dilution 1:1000)
Anti-IRα (Cell Signaling, 74118, dilution 1:1000)

Immunofluorescence

Wildtype HepG2 cells were fixed with 4% paraformaldehyde in PBS for 10 minutes at room temperature (RT), washed three times with PBS for 5 minutes at RT, permeabilized with 0.5% TX100 for 10 minutes at RT, washed with PBS for 5 minutes at RT, blocked with 4% BSA (Jackson Immunoresearch Laboratories - 001-000-162) in PBS for 1 hour at RT. Cells were incubated with primary antibodies diluted 1:500 in 4% BSA in PBS overnight at 4°C. Cells were washed three times with PBS for 5 minutes at RT and incubated with secondary antibodies Goat anti-Rabbit IgG Alexa Fluor 488 (Life Technologies, A11008) or 555 (Life Technologies, A21428)

diluted 1:500 in 4% BSA in PBS for 1 hour at RT. Cells were then washed in PBS three times for 5 minutes. Nuclei were stained with Hoechst (Thermo Fischer Scientific, 3258) diluted 1:5000 in PBS for 5 minutes at RT and excess Hoechst was removed by washing cells 3 times for 5 minutes with PBS. Cells were stored at 4°C in PBS and imaged using the ZEISS LSM 980 with Airyscan detector using 63x objective. Raw image series were processed via ZEN Blue (2D Airyscan processing). Images were converted in JPEG format using Fiji/ImageJ v2.1.0/153c.

Primary antibodies for immunofluorescence:

Anti-insulin receptor (Cell Signaling, 23413)
Anti-MED1 (Abcam, ab64965)
Anti-HP1α (Abcam, ab109028)
Anti-FIB1 (Abcam, ab582)
Anti-SRSF2 (Abcam, ab11826)
Anti-pIRS1 (Abcam, ab4873)

Fiji/ImageJ v2.1.0/153c was used to quantify pIRS1 fluorescence intensity. Since IRS1 gets phosphorylated in the cytoplasm, with the rectangle selection tool, a rectangle was drawn in cytoplasmic regions. The average fluorescence intensity in the rectangle (= in the cytoplasm) was determined using the measure tool on Fiji/ImageJ v2.1.0/153c. The background was then subtracted by a threshold determined by measuring the background intensity in a rectangular region outside of the cells.

Metabolomics for quantification of GSSG and GSH ratio

All solvents, including water, were purchased from Fisher and were Optima LC/MS grade.

HepG2 cells were treated according to the specified treatment protocol in 6-well culture plates, then the media was removed, and cells were washed twice with ice-cold PBS (Gibco, 10010-023) on ice. The PBS was then removed and 500 μl of ice-cold 80% methanol (Thermo Fisher Scientific, A456-4)/ 20% LC-MS grade water (Thermo Fisher Scientific, W6-4) solution with isotope-labeled amino acid mass-spec internal standards (Cambridge Isotope Labs, MSK-CAA-1) was added to each well on dry ice. The plate was chilled at -80°C for a minimum of 15 minutes, then the cells were scraped for 30 seconds with a plastic cell scraper (Corning, 3008). The methanol-cell mixture was transferred to a 1.5 ml eppendorf tube (Eppendorf, 0223641). The well was washed again with 300 μl of the ice-cold methanol solution to extract most of the remaining cells from the well, which was added to the same 1.5 ml eppendorf tube. The mixture was vortexed on high for 10 minutes at 4°C, then centrifuged on a table top centrifuge on max speed for 10 minutes at 4°C. 600 μl of supernatant were removed from the tube and transferred to a fresh tube on dry ice. The supernatant was dried for 5 hours at 4°C using a speed vac (Labconco 7310020), then resuspended in 1/10th of the volume of the original supernatant in LC-MS grade water on ice. The resuspended metabolites were vortexed on high for 10 minutes at 4°C, then centrifuged on a table top centrifuge on max speed for 10 minutes at 4°C. The supernatant containing the endogenous metabolites and internal standards were transferred to LC-MS vials and liquid chromatography and mass spec was carried out by the Whitehead Institute Metabolomics Core.

Metabolite profiling was conducted on a QExactive bench top orbitrap mass spectrometer equipped with an Ion Max source and a HESI II probe, which was coupled to a Dionex UltiMate 3000 HPLC system (Thermo Fisher Scientific, San Jose, CA). External mass calibration was performed using the standard calibration mixture every 7 days and an additional custom mass calibration was performed weekly alongside standard mass calibrations to calibrate the lower end of the spectrum (m/z 70-1050 positive mode and m/z 60-900 negative mode) using the standard calibration mixtures spiked with glycine (positive mode) and aspartate (negative mode). Typically, samples were reconstituted in 50 uL water and 2 uL were injected onto a SeQuant® ZIC®-pHILIC 150 x 2.1 mm analytical column equipped with a 2.1 x 20 mm guard column (both 5 mm particle size; Millipore-Sigma). Buffer A was 20 mM ammonium carbonate, 0.1% ammonium hydroxide; Buffer B was acetonitrile (Thermo Fisher Scientific, A955-4). The column oven and autosampler tray were held at 25°C and 4°C, respectively. The chromatographic gradient was run at a flow rate of 0.150 mL/min as follows: 0-20 min: linear gradient from 80-20% B; 20-20.5 min: linear gradient form 20-80% B; 20.5-28 min: hold at 80% B. The mass spectrometer was operated in full-scan, polarity-switching mode, with the spray voltage set to 3.0 kV, the heated capillary held at 275°C, and the HESI probe held at 350◦C. The sheath gas flow was set to 40 units, the auxiliary gas flow was set to 15 units, and the sweep gas flow was set to 1 unit. MS data acquisition was performed in a range of m/z = 70-1000, with the resolution set at 70,000, the AGC target at 1x106, and the maximum injection time at 20 msec. Relative quantitation of polar metabolites was performed with TraceFinder™ 4.1 (Thermo Fisher Scientific) using a 5 ppm mass tolerance and referencing an in-house library of chemical standards. Data were filtered according to predetermined QC metrics: CV of pools <25%; R of linear dilution series <0.975.

Metabolomics Analysis for quantification of GSSG and GSH ratio

FreeStyle (Thermo Scientific, Version 1.3) was used to check quality, mass shift, and retention time drift for each metabolite. The MS2 spectra for each metabolite was also verified in FreeStyle. TraceFinder (Thermo Fisher Scientific, Version 4.1) was used to call metabolite peaks and determine raw peak areas. The peak detection defaults were as follows - Mass tolerance: 5 ppm, Retention time window: 30 sec, Ion Ratio Window type: relative +/- 20%, Ion coelution (min) 0.100, Detection algorithm: ICIS (Area noise factor: 5, Peak

noise factor: 10, Baseline window: 40, Noise method: repetitive, Min peak width: 3, Multiplet resolution: 10, Area tail extension: 5). Each peak was manually verified to have the correct shape, retention time, and m/z.

Peak area ratios were determined by normalizing the raw peak area for each metabolite by the raw peak area of the appropriate internal standard.

During the mass spec run, a pooled sample made from pooling 5 μl of each sample was run 4-6 times as technical replicates to measure the reliability of detection for each metabolite—a coefficient of variation < 0.30 was used as a cutoff for metabolites to be measured reliably. Similarly, a dilution series of the pool was also run to determine whether each metabolite was in the linear range of detection—A correlation coefficient R < 0.95 was used as a cutoff.

Two-tailed student's t-test with Welch's correction was used to generate p-values. Statistical analysis was performed using Prism Version 9.4.0 (GraphPad, La Jolla, CA).

Identification of surface-exposed cysteines of individual proteins

Surface-exposed cysteines were identified for specific, individual proteins based on two criteria: 1) the cysteine residue is located within an intrinsically disordered region (IDR) of the protein,[124] as determined by the Predictors of Natural Disordered Regions (PONDR) VSL2 algorithm, or 2) the solvent-accessible area of the cysteine exceeds 20 $Å^2$,[125] as measured by STRIDE.[126]

Variant annotation

Variants and their genomic coordinates (hg38) were obtained from ClinVar: https://ftp.ncbi.nlm.nih.gov/pub/clinvar/vcf_GRCh38/archive_2.0/2023/clinvar_20230903.vcf.gz and ClinVar: https://ftp.ncbi.nlm.nih.gov/pub/clinvar/tab_delimited/variant_summary.txt.gz). Only germline missense variants were considered. We only considered variants with at least one clinical significance annotation as Pathogenic or Benign. The number of missense variants considered in ClinVar is 52,188.

When needed, variants were annotated with impact on protein sequence and other measures of computationally predicted pathogenicity (SIFT, PolyPhen, CADD etc) using Ensembl VEP 110. Gene-level and 1kb-window constraint metrics were obtained from gnomAD v4 and v3, respectively.

For all downstream analyses, variants were counted as protein variants—i.e., DNA variants resulting in the same protein-coding alteration, regardless of their similarity or differences at the DNA level, were counted as the same variant. Variants were mapped to gene, then mapped to proteins using mapping from Uniprot Swiss-Prot: https://ftp.uniprot.org/pub/databases/uniprot/current_release/knowledgebase/idmapping/by_organism/HUMAN_9606_idmapping_selected.tab.gz, https://ftp.uniprot.org/pub/databases/uniprot/current_release/knowledgebase/idmapping/by_organism/HUMAN_9606_idmapping.dat.gz, using the gene's HGNC ID to Uniprot-KB Accession ID of the canonical isoform.

Physics-based model for how cellular environment influences diffusion of proteins with and without cysteines

Estimation of the average number of surface-exposed cysteine per protein and the concentration of surface-exposed cysteine

We used iCysMod[127] to estimate the number of proteins with surface-exposed cysteines and the average number of surface-exposed cysteines per protein across the whole proteome. There are 18,350 proteins in the proteome, among which we tried two commonly used relative solvent accessibility (RSA) cutoffs to evaluate the cysteine surface exposure. With RSA > 40, the estimated number of proteins with at least one surface-exposed cysteine is 10,333 (56.3% of total proteins) with an estimated average number of surface-exposed cysteines of 2.8. With RSA > 50, the estimated number of proteins with at least one surface-exposed cysteine is 6,754 (36.8% of total proteins) with an estimated number of surface-exposed cysteines of 1.9. The mean estimated number of proteins with at least one surface-exposed cysteine using these two cutoffs is 8,544 (46.6% of total proteins, rounded to 50%) with an estimated number of surface-exposed cysteines of 2.35, rounded to 2. The total number of protein molecules per cubic micron in the cell is 2-4 million,[128] which yields 3.3-6.6 mM of proteins. Even though some measured values of cellular protein concentration can be 3 times lower,[128] the protein concentration should still be at least on the order of 1 mM. Given that around 50% of the proteins have at least one surface cysteine, among which each protein has 2 surface cysteines on average, the final surface cysteine concentration should be at least 1mM*50%*2 = 1mM.

Simulations of proteins with surface-exposed cysteines

Brownian dynamics simulations of proteins with surface cysteines (available at GitHub: https://github.com/younglab/proteolethargy) were performed by adapting the polychrom software package (https://doi.org/10.5281/zenodo.3579473), a thin wrapper around OpenMM.[129] We model proteins as self-avoiding, spherical particles of diameter $r_{rep} = 1.2$ which interact through a repulsive potential, $U(r_{ij}) = U_0\{1 + (\tilde{r_{ij}})^{12}[(\tilde{r_{ij}})^2 - 1]\}$ [Eq1], where $\tilde{r_{ij}} = \frac{r_{ij}}{r_{rep}}\sqrt{6/7}$ and $U_0 = 50\,k_BT$ represent a finite energy barrier to allow particle overlaps when $r_{ij} < 0.6r_{rep}$ (Figure S5A). Based on our estimates, the average number of surface-exposed cysteines on proteins that have surface-exposed cysteines is two (see "estimation of the average number of surface cysteine per protein and the concentration of surface cysteine"). Thus, simulated protein spheres are bonded to two surface "cysteines" via the harmonic potential $0.5k(r_{ij} - 0.5)^2$, where k is chosen such that the average extension of the bond is 0.01 when the bond energy is equal to k_BT. A harmonic angle potential of the form $0.5\kappa(\theta - 180^\circ)^2$ with $\kappa = 30k_BT$ enforces that the two cysteines are on opposite sides of the protein sphere. Cysteines on separate proteins can form intermolecular disulfide bridges, which are modeled via a short-ranged attractive

potential of the same form as Equation 1 (Figure S5B). In this case, $U_0 = -E_{attr}$ is the depth of the attractive potential and $\tilde{r}_{ij} = \frac{r_{ij}}{r_{attr}}\sqrt{6/7}$, where the cysteine-cysteine attraction radius is set to $r_{attr} = 0.2$. These parameters were chosen to minimize many-to-one bonding of cysteines, i.e. such that proteins with only 1 surface cysteine predominantly form dimers instead of higher order multimers (Figures S5C and S5D). We simulate 1000 proteins with periodic boundary conditions in a cube whose side length is chosen such that the proteins occupy 30% of the cube volume. Consistent with estimates of the fraction of proteins with surface-exposed cysteines in the cell (see "estimation of the average number of surface cysteine per protein and the concentration of surface cysteine"), 50% of the simulated proteins have two surface cysteines which can form disulfide bonds according to the value of E_{attr}, and the surface patches of the other 50% do not participate in disulfide bonding. As seen in Figure 4C, the proteins without surface-exposed cysteines diffuse more slowly at high E_attr since they are diffusing through a mesh of crosslinked proteins. However, this mobility reduction is far less pronounced than that of the proteins with surface exposed cysteines, which form dimers and multimers at high E_attr (Figure S5E).

For each value of E_{attr}, the diffusion coefficient is quantified as the slope of the protein's mean squared displacement over time. We normalize the diffusion coefficient to the mean of all data points for $E_{attr} \leq 11.25 k_B T$ and fit the resulting data to a decreasing S-curve of the form $D(E_{attr}) = min + (1.0 - min)\left[e^{-k(E_{attr}-E_0)}/(1+e^{-k(E_{attr}-E_0)})\right]^a$ (solid line in Figure S5F). For each simulation, we also calculate the fraction of cysteines that participate in intermolecular disulfide bonding, i.e. the fraction of sticky patches which are within r_{attr} of a neighboring patch (Figure S5G). This data is fit to an increasing S-curve of the form $f(E_{attr}) = \left[1/(1+e^{-k(E_{attr}-E_0)}\right]^a$ to obtain the solid line in Figure S5G. The fraction of bonded cysteines can be mapped to the oxidative state of a cell as measured by the ratio of oxidized to reduced glutathione (GSSG/GSH) using a chemical reaction model (see "chemical reaction model for coupling protein-protein disulfide bonding to redox state" section). For a given value of E_{attr}, we use $f(E_{attr})$ to compute the fraction of bonded cysteines as obtained from the simulations. Figure S5H then allows us to read off the corresponding value of GSSG/GSH. Thus, we relate E_{attr} to the oxidative state of the cell. This in turn allows us to graph the diffusion coefficient as a function of the oxidative state in Figure 4C, where the solid lines represent the fit relationships in Figures S5F–S5H and points show raw simulation data.

Simulation hyperparameter tuning and validation

Since disulfide bonding is modeled via a pairwise attractive potential between surface-exposed cysteines, it is possible for one cysteine to attract more than one binding partner on neighboring proteins. Such many-to-one bonding events can be minimized by tuning the following simulation hyperparameters: the protein-protein repulsion radius, r_{rep}, the protein-protein repulsion energy E_{rep} (Figure S5A), the cysteine-cysteine attraction radius, r_{attr} (Figure S5B), and the spring constant k for the harmonic bonds connecting each protein to each of the cysteines on its surface.

For a given set of parameters $(r_{attr}, r_{rep}, E_{rep}, k)$, we calculate the equilibrium cysteine-cysteine distance $d_3{}^*$ and bond extension $x_3{}^*$ that minimizes the energy of a trimer of proteins with just one surface cysteine, $E_{trimer}(d,x) = 3U_{attr}(d) + 3U_{rep}(d + \sqrt{3}(0.5 + x)) + 3/2kx^2$ (Figure S5C). Analogously, we compute the values of $d_2{}^*$ and $x_2{}^*$ that minimize the energy of a dimer, $E_{dimer}(d,x) = U_{attr}(d) + U_{rep}(d + 2(0.5 + x)) + kx^2$.

We then choose a parameter set where $E_{trimer}(d_3{}^*, x_3{}^*) > 0 > E_{dimer}(d_2{}^*, x_2{}^*)$ for all values of $E_{attr} \in [0,30]\ k_B T$. From this approach, we identified that the choice of $r_{attr} = 0.2, r_{rep} = 1.2, E_{rep} = 50 k_B T, k = 2k_B T/(0.01)^2$ ensured that trimers are always less energetically favorable than dimers. In Figure S5D, we confirm that using these parameters, proteins with one surface cysteine only form dimers even at high values of E_{attr}.

Chemical reaction model for coupling protein-protein disulfide bonding to redox state

To investigate the coupling between cellular redox and the propensity for proteins with surface exposed cysteines to form disulfide bonds, we developed a minimal chemical reaction model. In this model, we assume the level of oxidative stress is represented by a fixed concentration of hydrogen peroxide $[H_2O_2]$, which is the predominant reactive oxygen species (ROS) in the cell.[130] We also assume that glutathione is the primary species responsible for regulating ROS, given that it is the most abundant non-protein antioxidant in the cell.[131] Glutathione (GSH) and proteins with surface exposed thiol groups (PSH) are oxidized in the presence of H_2O_2 and can form disulfide bridges via the following set of reactions:

$$GSH + H_2O_2 \xrightarrow{k_{on}} GSOH + H_2O$$

$$PSH + H_2O_2 \xrightarrow{k'_{on}} PSOH + H_2O$$

$$GSOH + GSH \xrightarrow{k_{SS}} GSSG + H_2O$$

$$GSOH + PSH \xrightarrow{k_{SS}} PSSG + H_2O$$

$$PSOH + GSH \xrightarrow{k_{SS}} PSSG + H_2O$$

$$PSOH + PSH \xrightarrow{k_{SS}} PSSP + H_2O$$

The second-order rate constant of the oxidation of the thiol of a glutathione is k_{on} = 0.42 $M^{-1}s^{-1}$[132] and the rate constant for the oxidation of the thiol of a protein is $k_{on}{}' = 2.3\ M^{-1}s^{-1}$ (based on the oxidation of Cys-34 in BSA).[132] GSOH and PSOH are highly reactive intermediate products which then undergo a much faster disulfide bridging process ($k_{SS} \gg k_{on}, k_{on}{}'$) with another thiol.[133] We set $k_{SS} = 50\ k_{on}{}'$. We assume that proteins can form disulfide bonds with other proteins (PSSP) or with glutathione (PSSG) at equal rates.

Intramolecular disulfide bonds of proteins are removed by a thiol group interchange reaction with GSH.[134] We reason that removal of intermolecular disulfide bonds could be achieved by a similar mechanism:

$$PSSP + GSH \xrightarrow{k_{ex}} PSSG + PSH$$

$$PSSG + GSH \xrightarrow{k_{ex}} GSSG + PSH$$

$$GSSG + PSH \xrightarrow{k_{ex}} PSSG + GSH$$

$$PSSG + PSH \xrightarrow{k_{ex}} PSSP + GSH$$

where we take $k_{ex} \approx$ 0.15 $M^{-1}s^{-1}$ (estimated from the disulfide interchange between GSSG and 2-Mercaptoethanol at pH=7).[135] Ultimately, GSSG is reduced by NADPH,

$$GSSG \xrightarrow{k_{NADPH}} 2\ GSH,$$

while the total concentration of glutathione[136] and surface-exposed protein cysteines (see "estimation of the average number of surface cysteine per protein and the concentration of surface cysteine") are conserved at 1mM:

$$G_{tot} = [GSH] + [GSOH] + [PSSG] + 2[GSSG] = 1\text{mM}$$

$$P_{tot} = [PSH] + [PSOH] + [PSSG] + 2[PSSP] = 1\text{mM}.$$

We simulate the ordinary differential equations (see "ODEs of the chemical reaction model for coupling protein-protein disulfide bonding to redox state") associated with the above chemical reactions for the dynamics of [GSOH], [PSOH], [GSSG], [PSSG], and [PSSP] using MATLAB with ode45. The rate of glutathione reduction $k_{NADPH} = 2.72\times10^{-6}\ s^{-1}$ is chosen such that when the steady state [GSSG]/[GSH] ratio is 0.01 (physiological redox ratio[137]), $[H_2O_2]$ is 10nM (physiological hydrogen peroxide concentration[130]).

We then determine the fraction of surface-exposed cysteines that participate in protein-protein disulfide bonding, $2[PSSP]/P_{tot}$, as a function of the steady state ratio [GSSG]/[GSH] (Figure S5H). Note that even at high ROS, this fraction is capped at 0.62 since surface-exposed cysteines are equally likely to bind to a thiol on a neighboring protein or the thiol of glutathione. Our protein simulations do not include glutathione. Thus, the fraction of bonded cysteines as computed from simulations, which can go up to 1.0 (Figure S5G), corresponds to the fraction of cysteines participating in inter-protein disulfide bridges in our chemical reaction model. To map E_{attr} to GSSG/GSH, we only consider simulation data for which the fraction of bonded cysteines is less than 0.62.

ODEs of the chemical reaction model for coupling protein-protein disulfide bonding to redox state

$$\frac{d[GSOH]}{dt} = k_{on}[GSH][H_2O_2] - k_{SS}[GSH][GSOH] - k_{SS}[PSH][GSOH]$$

$$\frac{d[PSOH]}{dt} = k'_{on}[PSH][H_2O_2] - k_{SS}[GSH][PSOH] - k_{SS}[PSH][PSOH]$$

$$\frac{d[GSSG]}{dt} = k_{SS}[GSH][GSOH] + k_{ex}[PSSG][GSH] - k_{ex}[GSSG][PSH] - k_{NADPH}[GSSG]$$

$$\frac{d[PSSG]}{dt} = k_{SS}[PSH][GSOH] + k_{SS}[GSH][PSOH] + k_{ex}[PSSP][GSH] + k_{ex}[GSSG][PSH] - k_{ex}[PSSG][GSH] - k_{ex}[PSSG][PSH]$$

$$\frac{d[PSSP]}{dt} = k_{SS}[PSH][PSOH] + k_{ex}[PSSG][PSH] - k_{ex}[PSSP][GSH]$$

$$[GSH] = G_{tot} - [GSOH] - [PSSG] - 2[GSSG]$$

$$[PSH] = P_{tot} - [PSOH] - [PSSG] - 2[PSSP]$$

where $[GSH] = G_{tot}$ and $[PSH] = P_{tot}$ at t = 0. $[H_2O_2]$ is a constant value for each simulation ranging from $10 - 3$ uM to 10 uM.

ROS stain and imaging

Following cell treatment, media was removed and cells were incubated with 5 mM CellROX Deep Red Reagent (Thermo Fisher Scientific, C10422) diluted in EMEM for 30 minutes. Cells were then fixed with 4% paraformaldehyde in PBS (BTC Beantown Chemical, 140770-10x10ML) for 10 minutes. Cells were washed with PBS three times and imaged using the RPI Spinning disk confocal microscope, 60x objective. ROS signal intensity was measured using the "measure tool" on Fiji/ImageJ v2.1.0/153c. A two-tailed student's t-test was used to generate p-values. Statistical analysis was performed using Prism Version 9.4.0 (GraphPad, La Jolla, CA). All ROS imaging experiments were performed twice using 2-4 biologically independent samples.

Modeling of the diffusion-limited tyrosine kinase receptor phosphorylation

For a generic reaction $A + B \rightarrow C^*$ at the molecular level, two basic steps are needed to accomplish this reaction: (i) molecules A and B need to "find" each other, and (ii) they transform into an activated complex C^*. The first basic step is called "collision" and the second basic step is called "activation". Accordingly, there are two fundamental rate constants that defines the overall reaction rate: the diffusion limited rate constant k_D describes the rate of collision through the diffusion process, and the inherent reaction constant k_r describes the rate of activation. While k_r is determined by the intrinsic chemical property, $k_D := 4\pi(D_A + D_B)\beta$ largely depends on the diffusion coefficients of molecule A and B, which are D_A and D_B, respectively. β is the characteristic length-scale, defined below.

The exact relation between the overall reaction rate and the two fundamental rate constants is[138]:

$$k = \frac{k_D k_r}{k_r + k_D \exp\left(\frac{U(R_{AB})}{k_B T}\right)}$$

In this equation, R_{AB} is the center-to-center distance when spherical molecules A and B touch, $U(r)$ is the potential between molecules A and B when spaced by a center-to-center distance r, $k_B T$ has the dimension of energy as the product of Boltzmann constant and temperature.

We then use the receptor tyrosine kinase phosphorylation reaction in the collision-limited realm as an example to quantify the relation between protein mobility (D) and protein functional activity (k) in cell:

$$k(D) = \frac{8\pi D\beta k_r}{k_r + 8\pi D\beta \exp\left(\frac{U(2R)}{k_B T}\right)}$$

Here we have assumed equal diffusion coefficients (D) and protein sizes (R) for substrate and enzyme for simplicity. To draw the k-D relation, additional parameters/functions need to be determined, including R, $U(r)$, $k_B T$, β, and k_r.

- The radius of receptor tyrosine kinases is estimated to be R=3 nm.

- For $U(r)$, we adapted a 10-5 Lennard-Jones potential in the colloid-type spherical model to describe the interactions between substrate and enzyme: $U(r) = 4\varepsilon\left(\left(\frac{\sigma}{r}\right)^{10} - \left(\frac{\sigma}{r}\right)^{5}\right)$, and common value of ε = 4.0 kJ/mol was used.[139] Lennard-Jones parameters σ were obtained from the protein radius: $\sigma := 2^{5/6}R$ = 5.35 nm.
- k_BT is set to the value that represents 37°C: k_BT = 2.5 kJ/mol.
- β is a characteristic length-scale defined as $\beta^{-1} = \int_{R_{AB}}^{\infty} dr \cdot \exp\left(U(r)/k_BT\right)/r^2$, which is computed as 7.60 nm in this case (note that R_{AB} =2R).
- To estimate the inherent reaction constant k_r, the apparent receptor tyrosine phosphorylation rate of EGFR *in vitro* is adopted: k = 5.5×10^7 M^{-1}s^{-1}.[140] Therefore, the k_r can be reversely solved in a dilute solution scenario (i.e., $\exp\left(\frac{U(R_{AB})}{k_BT}\right) \approx 1$) as:

$$k_r = \left(\frac{1}{k} - \frac{1}{8\pi D_{vitro}\,\beta}\right)^{-1}$$

To back-calculate k_r, we also need an estimation of the *in vitro* diffusion coefficient of receptor tyrosine kinases. The diffusion coefficient of insulin receptor measured in our paper in live cells (D_{cell} ~1 μm^2/s) is adopted given the comparable molecular weights among insulin receptor, IRS1, and EGFR. It is also known that the diffusion coefficient *in vitro* is around 3 times higher than in cell,[141] thus the effective diffusion coefficient of EGFR in the referred *in vitro* work[140] is estimated to be D_{vitro} ~3 μm^2/s. Hence, k_r = 6.5× 10^7 M^{-1}s^{-1}.

With those parameters/functions in hand, *k-D* relation is generated as plotted in Figure 6D.

In vitro IRS1 phosphorylation

Purified active recombinant human insulin receptor (IR) (Millipore, 14-466) and purified recombinant insulin responsive substrate 1 (IRS1) (Abcam, ab70538) were incubated in freshly prepared reaction buffer consisting of 50 mM Tris pH 7.5, 0.1 mM EGTA, 0.1 mM Na_3VO_4, 0.1 mM 2-mercaptoethanol, 10 mM $MnCl_2$ and 0.01 mg/ml bovine serum albumin with the indicated concentrations of glycerol (Invitrogen, 15514011) for 5 minutes at 30°C immediately after the addition of 50 μM ATP in 5 mM magnesium acetate. All samples were prepared with 75 ng of IR and 240 ng of IRS1. These amounts and ratios were chosen because they fell within the linear range of IRS1 phosphorylation by IR and they provided equivalent moles of IR and IRS1. For samples that were agitated, tubes were subjected to orbital mixing at 1200 rpm using a Thermomixer (Eppendorf, ThermoMixer C, EP5382000023) during the entire incubation. After 5 minutes, reactions were immediately quenched with dithiothreitol (DTT) and XT Sample Buffer 4x (BioRad, 1610791) to a final concentration of 100mM and 1x, respectively and incubated at 95°C for 5 minutes, then ran on Western blot or frozen at -80°C until subjected to western blot.

RNA-seq

Cells were treated with normal or pathogenic insulin concentrations for three days and washed with EMEM as described above and cultured in EMEM solo for 4 hours. RNA was then purified using TRIzol™ reagent (Thermo Fisher Scientific, 15596026) following manufacturer's instructions. RNA-seq libraries were prepared using KAPAHyperRiboErase (Roche, KK8561) and were sequenced on Illumina NovaSeq 6000, generating at least 200 million paired-ended 150-bp reads per sample. Reads were mapped to the human genome GRCh38 using STAR aligner[105] (v2.7.1a), allowing up to 100 multiple alignments and up to 200 loci anchors (–outFilterMultimapNmax 100 –winAnchorMultimapNmax 200). Differential expression analysis of genes and transposable elements comparing triplicates of samples treated with normal or pathogenic concentrations of insulin was performed using TEtranscripts[106] (v2.2.3). The list of protein coding genes was downloaded from ENSEMBL BioMart (http://www.ensembl.org/biomart/martview/6e82036bfd2b9ca0c5044d2c7449824d).

ChIP-seq

Published MED1 ChIP-seq data (GEO: GSM2040029) and input (GEO: GSM2864933) were used in this study. ChIP-seq bioinformatics analysis was performed on the Whitehead High-Performance Computing Facility using the nf-core ChIP-seq pipeline v1.2.1112 with Nextflow v20.04.1. Quality control of fastq files was performed with FastQC v0.11.9. Trim Galore! v0.6.4_dev was used to trim low-quality reads. Alignment was performed against the hg19 genome assembly using BWA v0.7.17-r1188.[107] Peak calling was performed using MACS2[108] v2.2.7.1 with q value of 0.01. For the identification of genes whose promoter (transcription start site, TSS, +/-1kb) were occupied by MED1, the same hg38 gene list used for the RNA-seq analysis was used. The coordinates of the promoters were converted from hg38 to hg19 using LiftOver (https://genome.ucsc.edu/cgi-bin/hgLiftOver). Bedtools[109] v2.29.2 was used to measure the distance between MED1 peaks and gene promoters (bedtools closest -d). A gene was considered occupied by MED1 the distance between MED1 peak and the promoter was 0. The changes in gene expression measured by RNA-seq were matched to each MED1-occupied and non-occupied gene using the VLOOKUP tool in Excel v16.78.3.

Illustrations

PyMOL[142] was used for protein illustrations in Figures 4A, 6A, 7B, and S6B. PDB ID: IR 6PXV, MED1 7EMF, HP1α 3I3C, FIB1 7SE7, SRSF2 2LEC. Cartoon illustrations were created with BioRender.com. Figures were generated using Adobe Illustrator v27.0.1.

QUANTIFICATION AND STATISTICAL ANALYSIS

Statistical analyses for FRAP were performed using the Statistics and Machine Learning Toolbox of MATLAB R2021b or R2024a (The MathWorks, Inc., Natick, MA). All other statistical analyses were performed using Prism Version 9.4.0 (GraphPad, La Jolla, CA). All statistical tests used, the exact value of n, and what n represents can all be found in the figure legends. All data are reported as mean ± SEM or mean + SEM. For Figures 2E, 5B, 5C, 5F, 6J, S2K, S4B, S6E, S7B, and S7C, a two-tailed Mann-Whitney U test was applied. For Figures 2G, 3F, 3I, 4D–4F, 4H, 4I, 5E, S3A, S4A, S4C–S4E, and S6C, an unpaired two-tailed student's *t*-test was applied. For Figures 3B, 6E, 6K, 6L, S1A–S1E, and S7D, an unpaired two-tailed student's *t*-test with Welch's correction was applied. All statistical results were done without randomization or stratification. The notation for statistical significance is as follows: * represents $p < 0.05$, ** represents $p < 0.01$ and *** represents $p < 0.001$.

Supplemental figures

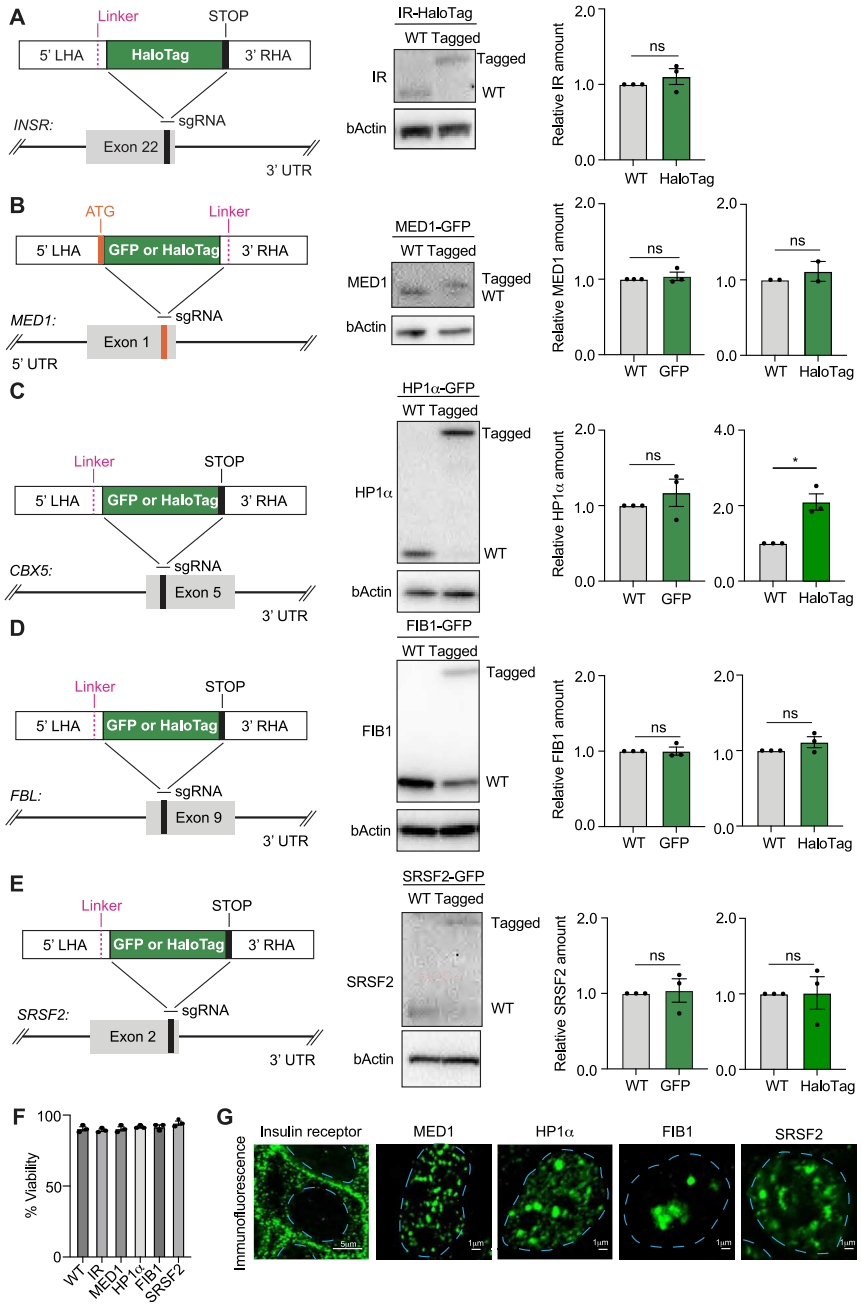

Figure S1. Cell line validation, related to Figure 1

(A) Strategy to endogenously tag IR with HaloTag (left). Immunoblot for IR and beta actin (β-actin, middle). Quantification of relative IR amount as compared with beta actin (right). Data are plotted as mean ± SEM (n = 3 biological replicates in each condition).

(B) Strategy to endogenously tag MED1 with GFP or HaloTag (left). Immunoblot for MED1 and beta actin (β-actin, middle). Quantification of relative MED1 amounts as compared with beta actin (right). Data are plotted as mean ± SEM (n = 2 to 3 biological replicates in each condition).

(C) Same as (B), but for HP1α (n = 3 biological replicates in each condition). * represents p value < 0.05.

(D) Same as (B), but for FIB1.

(E) Same as (B), but for SRSF2.

(F) Viability of WT cells or cells expressing endogenous IR, MED1, HP1α, FIB1, and SRSF2 tagged with HaloTag. Data are plotted as mean ± SEM (n = 3 biological replicates in each condition).

(G) Immunofluorescence images of IR, MED1, HP1α, FIB1, and SRSF2 (green) in WT HepG2 cells. Dashed blue lines represent nuclear outline. Scale bars are indicated.

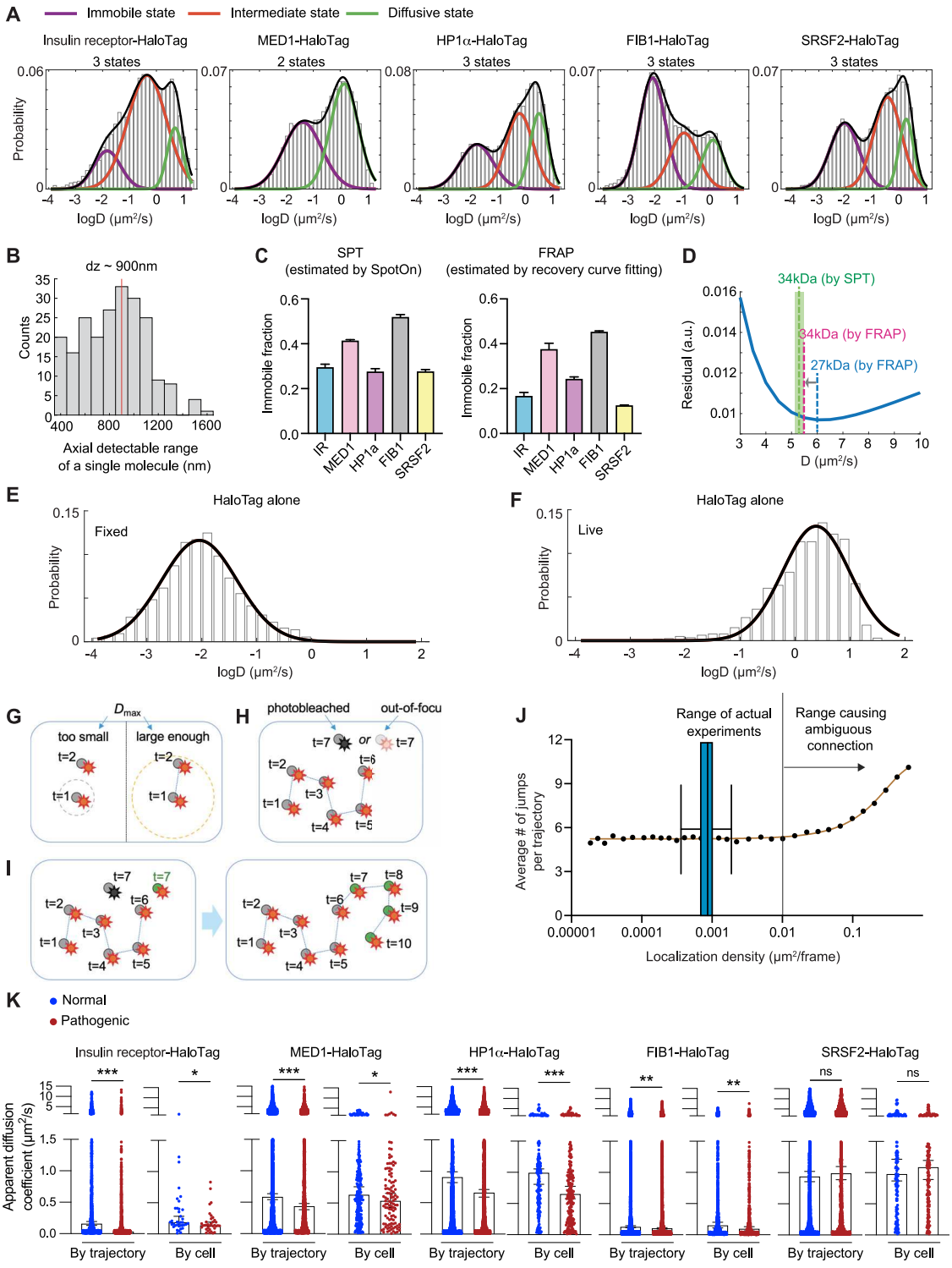

Figure S2. Additional characterization of SPT and FRAP analyses, related to Figures 1 and 2

(A) log*D* distribution of individual molecules (histogram) fitted to either two or three Gaussian functions (colored curves indicate individual Gaussian functions, and the black curve in each graph is the sum of individual Gaussian functions).

(B) Distribution of the continuous axial detectable range of a single molecule. The distribution peaked at ~900 nm.

(C) Immobile fraction of endogenous proteins estimated from SPT dataset vs. FRAP dataset. Data are plotted as mean + SEM.

(legend continued on next page)

(D) Plot of the residual of experimentally observed and theoretical models of FRAP recovery as a function of different diffusion coefficient *D* used for the model. The best-fitted diffusion coefficient of GFP (27 kDa) is indicated by a dashed blue line. The apparent diffusion coefficients of a HaloTag-JF646 (~34 kDa), based on SPT, are indicated as mean (dashed green line) and SEM (light green). The apparent diffusion coefficient of a HaloTag-JF646 (~34 kDa) inferred from the relationship between FRAP-estimated diffusion of a protein of known molecular weight, GFP (27 kDa), is indicated by a dashed magenta line.
(E) The log*D* distribution of individual HaloTag-alone molecules in fixed sample (histogram). The solid black line represents the best-fitted single Gaussian function.
(F) The log*D* distribution of individual HaloTag-alone molecules in live sample (histogram). The solid black line represents the best-fitted single Gaussian function.
(G) Graphical illustration of a premature stop during localization reconnection caused by assuming a too small maximumly allowed prior apparent diffusion coefficient (D_{max}) (left) vs. a successful reconnection because of assuming a large enough D_{max} (right).
(H) Graphical illustration of two reasons why the tracking of a protein may stop even if the next localization is within the two-dimensional range defined by D_{max}: (i) photobleach of the dye molecule tagged to the protein and (ii) the protein moving out of focus.
(I) Graphical illustration of why the localization reconnection may continue by mistakenly joining the trajectories of two proteins together. In this case, the number of jumps per "trajectory" will go beyond normal.
(J) Average number of jumps per trajectory at different localization density. Beyond certain localization density threshold (vertical line at ~0.01 per μm^2 per frame), the number of jumps per "trajectory" will start to increase due to the reason shown in (I), which is associated with significant chance of ambiguous connection. The localization density range of the actual experiments for IR-HaloTag SPT is marked as the horizontal boxplot, which is safely below the threshold that will cause significant ambiguous connection.
(K) Diffusion coefficient comparisons based on trajectory-level (left) or cell-level analysis (right) for IR, MED1, HP1α, FIB1, and SRSF2. Apparent diffusion coefficients for normal (blue) and pathogenic (red) conditions are shown. For trajectory-level analysis, each dot represents the value for individual trajectories; the median value is indicated by the black rectangle, while the error bars identify the 95% confidence interval of the median. For cell-level analysis, each dot represents the median value of the trajectories assigned to a single cell; the median value of the set of cell-level values is indicated by the black rectangle, while the error bars identify the 95% confidence interval of the median. IR: by trajectory, normal n = 1,169 trajectories, pathogenic n = 1,323 trajectories; by cell, normal n = 37 cells, pathogenic n = 35 cells. MED1: by trajectory, normal n = 5,719 trajectories, pathogenic n = 2,227 trajectories; by cell, normal n = 214 cells, pathogenic n = 110 cells. HP1α: by trajectory, normal n = 4,568 trajectories, pathogenic n = 3,598 trajectories; by cell, normal n = 180 cells, pathogenic n = 219 cells. FIB1: by trajectory: normal n = 2,855 trajectories, pathogenic n = 205 trajectories; by cell, normal n = 205 cells, pathogenic n = 162 cells. SRSF2: by trajectory: normal n = 3,399 trajectories, pathogenic n = 2,872 trajectories; by cell: normal n = 142 cells, pathogenic n = 162 cells. Mann-Whitney test was used for statistical analysis.

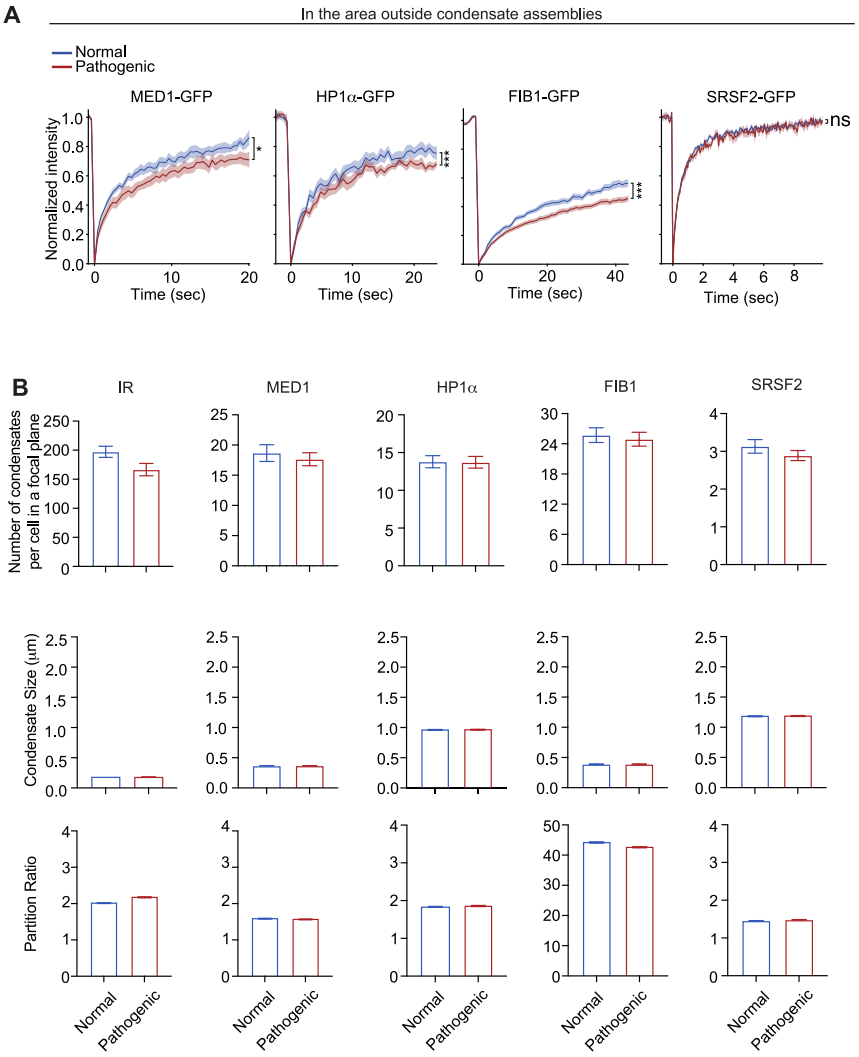

Figure S3. The effect of pathogenic signaling on protein mobility outside of condensates and on condensate properties, related to Figure 2

(A) Quantification of FRAP data for MED1, HP1α, FIB1, and SRSF2 in areas outside of condensate assemblies in cells that were treated with normal signaling (normal) or pathogenic signaling (pathogenic). Number of cells: MED1 normal n = 10, pathogenic n = 10; HP1α normal n = 15, pathogenic n = 15; FIB1 normal n = 24, pathogenic n = 24; SRSF2 normal n = 14, pathogenic n = 14. t test was used for statistical analysis. * represents p value < 0.05 and *** represents p value < 0.001.

(B) Number, size, and partition ratio of IR, MED1, HP1α, FIB1, and SRSF2 condensates in cells that were treated with normal signaling (normal) or pathogenic signaling (pathogenic). Number of condensates: IR normal n = 22, pathogenic n = 24; MED1 normal n = 135, pathogenic n = 127; HP1α normal n = 44, pathogenic n = 56; FIB1 normal n = 150, pathogenic n = 214; SRSF2 normal n = 58, pathogenic n = 53. Condensate size, number of condensates: IR normal n = 3,846, pathogenic n = 3,548; MED1 normal n = 3,522, pathogenic n = 3,426; HP1α normal n = 1,499, pathogenic n = 1,558; FIB1 normal n = 541, pathogenic n = 660; SRSF2 normal n = 954, pathogenic n = 699. Partition ratio, number of condensates: IR normal n = 3,846, pathogenic n = 3,548; MED1 normal n = 3,522, pathogenic n = 3,426; HP1α normal n = 1,499, pathogenic n = 1,558; FIB1 normal n = 541, pathogenic n = 660; SRSF2 normal n = 954, pathogenic n = 699.

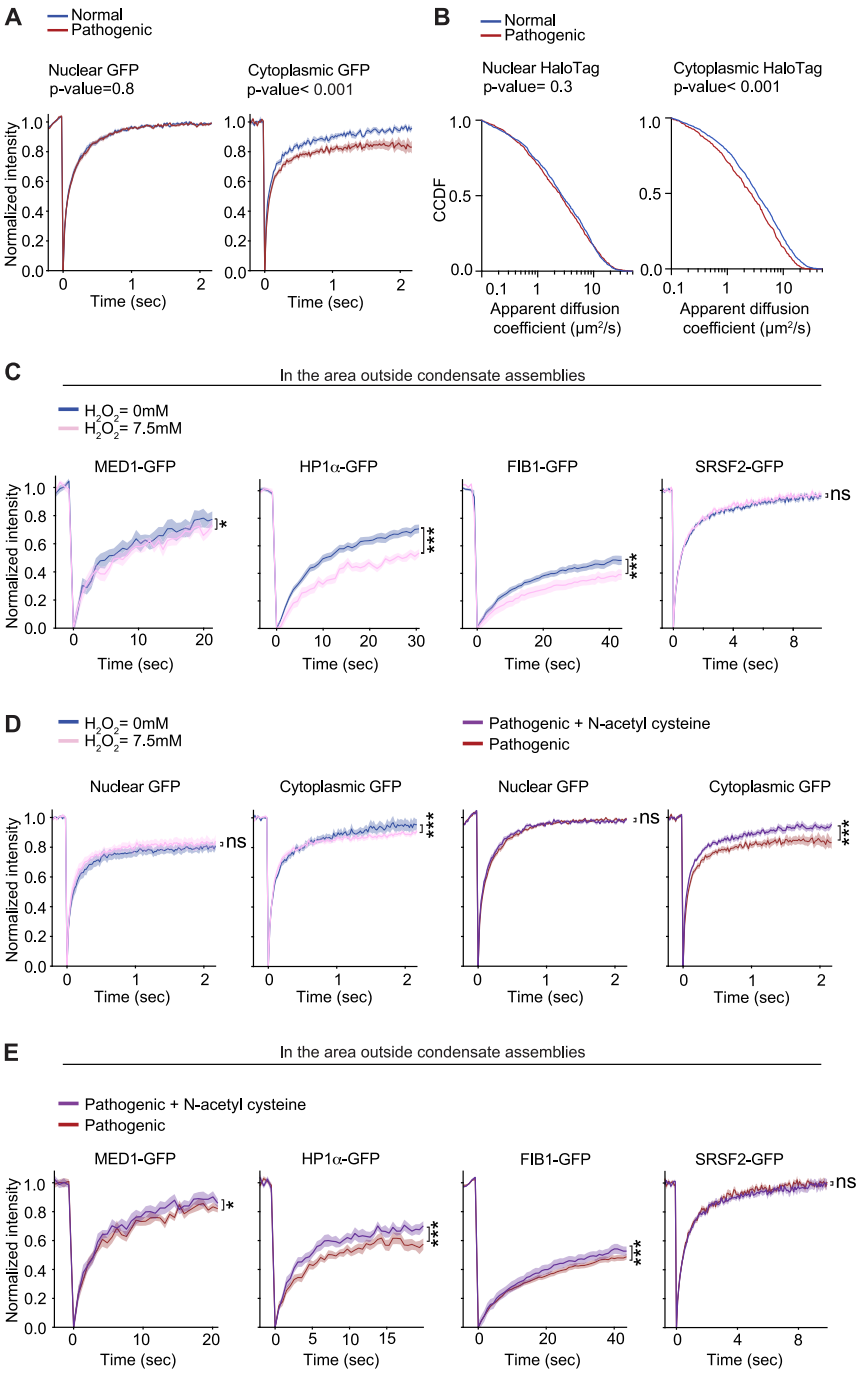

Figure S4. The effect of oxidative environments on protein mobility, related to Figures 2 and 3

(A) Quantification of FRAP data for nuclear (left) and cytoplasmic (right) GFP in HepG2 cells that were treated with normal signaling (normal) or pathogenic signaling (pathogenic). Nuclear GFP, number of cells: normal n = 16, pathogenic n = 17; cytoplasmic GFP: n = 15 for each condition. Data are plotted as mean (dark blue and dark red lines) ± SEM (light blue and light red regions). p values are reported in the figure.

(B) CCDF graphs of apparent diffusion coefficients as determined by SPT for nuclear (left) and cytoplasmic (right) HaloTag in HepG2 cells that were treated with normal signaling (normal) or pathogenic signaling (pathogenic). Nuclear HaloTag, number of molecules: normal n = 771, pathogenic n = 937; cytoplasmic HaloTag: normal n = 1,279, pathogenic n = 625. t test was used for statistical analysis. p values are reported in the figure.

(C) Quantification of FRAP data for MED1, HP1α, FIB1, and SRSF2 in areas outside of condensates in HepG2 cells that were treated with 0 mM H_2O_2 or 7.5 mM H_2O_2. 0 mM H_2O_2 n = 11, 20, 15, and 14 cells for MED1, HP1α, FIB1, and SRSF2, respectively. 7.5 mM H_2O_2 n = 11, 20, 15, and 14 cells for MED1, HP1α, FIB1, and SRSF2, respectively. * represents p value < 0.05 and *** represents p value < 0.001.

(legend continued on next page)

(D) Quantification of FRAP data for nuclear and cytoplasmic GFP in HepG2 cells that were treated with 0 mM H_2O_2 or 7.5 mM H_2O_2 (n = 7 cells per condition for nuclear FRAP and n = 10 cells per condition for cytoplasmic FRAP). Data are plotted as mean (dark pink and dark blue lines) ± SEM (light pink and light blue regions). Quantification of FRAP data for nuclear GFP in HepG2 cells previously treated with pathogenic signaling with (pathogenic + N-acetyl cysteine [NAC], n = 17 cells) or without (pathogenic, n = 11 cells) NAC (left). Quantification of FRAP data for cytoplasmic GFP in HepG2 cells previously treated with pathogenic signaling with (pathogenic + NAC, n = 10 cells) or without (pathogenic, n = 10 cells) NAC (left). *** represents p value < 0.001.
(E) Quantification of FRAP data for MED1, HP1α, FIB1, and SRSF2 in areas outside of condensates in n HepG2 cells previously treated with pathogenic signaling with or without NAC. Without NAC n = 11, 20, 37, and 15 cells for MED1, HP1α, FIB1, and SRSF2, respectively. With NAC n =11, 20, 28, and 15 for MED1, HP1α, FIB1, and SRSF2, respectively. Data are plotted as mean (dark purple and dark red lines) ± SEM (light purple and light red regions). t test was used for statistical analysis. * represents p value < 0.05 and *** represents p value < 0.001.

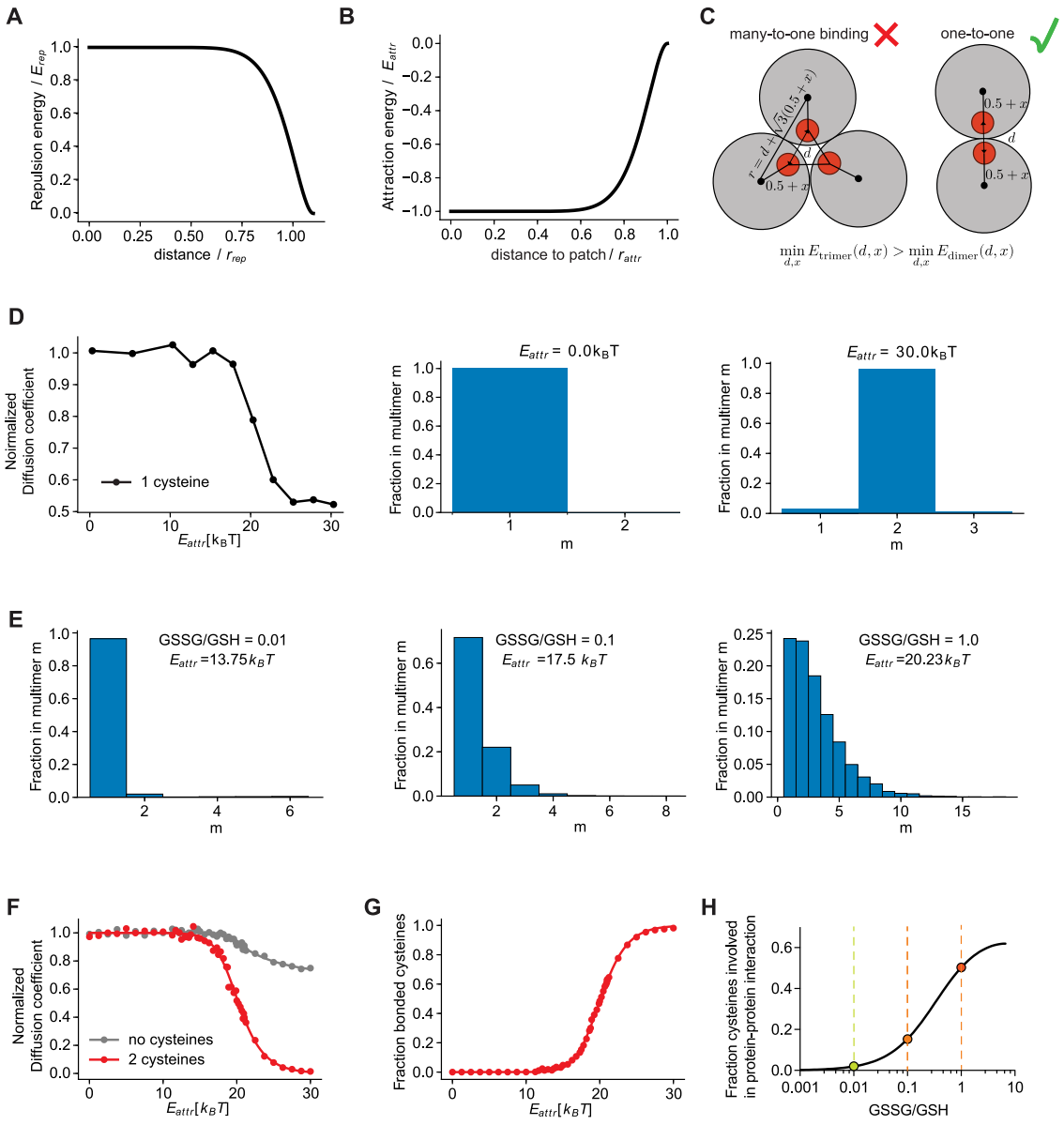

Figure S5. Modeling protein diffusion with increasing ROS, related to Figure 4

(A) Repulsive potential between protein spheres as a function of the inter-protein distance normalized to the protein diameter r_{rep}.

(B) Attractive potential between sticky patches (surface cysteines) as a function of the inter-patch distance normalized to the patch-patch attraction radius r_{attr}. The depth of the attractive potential, E_{attr}, controls the propensity for intermolecular disulfide bonding.

(C) Cartoon depicting minimum energy configurations of a trimer of proteins with a single surface cysteine, which represents an undesirable many-to-one bonding event, and a dimer, which represents a one-to-one bonding event. These configurations are determined by the equilibrium patch-patch distance d and protein-cysteine bond extension *x*, which minimize the energy of the trimer or dimer. Simulation parameters are chosen such that trimers are energetically less favorable than dimers.

(D) Diffusion coefficient and cluster size distributions from simulations of 1,000 proteins with one surface-exposed cysteine as a function of E_{attr}, normalized to the mean of the first five data points. At E_{attr} = 0 k_BT, all proteins are in a monomeric state, but at E_{attr} = 30 k_BT, nearly all proteins form dimers. Notably none form trimers, demonstrating that the choice of simulation hyperparameters minimizes many-to-one bonding.

(E) Fraction of simulated proteins that form a multimer of size m for simulations at three different values of E_{attr}, which correspond to three different GSSG/GSH ratios highlighted in (H).

(F) Normalized diffusion coefficient from simulations of a mixture of proteins with (red) and without (gray) surface-exposed sticky patches (cysteines) as a function of the patch-patch attraction energy E_{attr}.

(G) Fraction of surface cysteines that participate in intermolecular bonding as a function of E_{attr}, as calculated from protein dynamics simulations.

(legend continued on next page)

(H) Fraction of surface cysteines that participate in protein-protein disulfide bonding as a function of the steady-state ratio of oxidized (GSSG) to reduced (GSH) glutathione, as calculated from a chemical reaction model. Representative GSSG/GSH ratios are highlighted with dashed lines and circles (yellow, orange, and red).

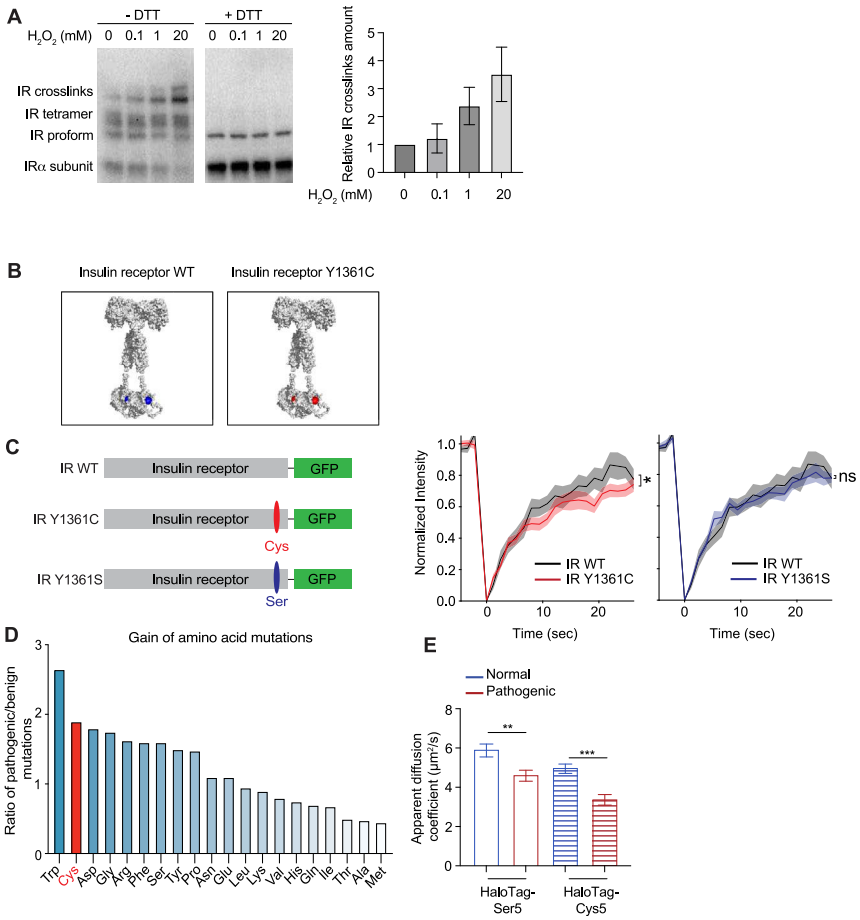

Figure S6. Cysteines in protein mobility, related to Figure 4

(A) Immunoblot for IR (left). Cells were treated with indicated concentrations of H_2O_2 prior to protein isolation and western blotting in reducing (+DTT) or non-reducing (−DTT) conditions. Quantification of relative IR crosslink amount as compared with IRα subunit (right).

(B) Renderings of dimers of WT or dimers of Y1361C IR. Cartoon design was based on both the previously published structure of IR (PDB: 6PXV) and the AlphaFold structure of the unresolved region of IR. Tyrosines are represented as blue, and cysteines are represented in red.

(C) Cartoon depicting WT (IR WT) and mutant IR (IR Y1361C and IR Y1361S; left). Quantification of FRAP data for WT (IR WT, n = 15 cells) and mutant IR (IR Y1361C, n = 16 cells; IR Y1361S, n = 15 cells; right). These experiments were performed on the same day, and as a result, the IR WT FRAP curves are the same. Data are plotted as mean (dark black, dark red, and dark blue lines) ± SEM (light black, light red, and light blue regions). t test was used for statistical analysis. * represents p value < 0.05.

(D) Measurement of the pathogenicity of all 20 gain-of-amino acid mutations as determined by the ratio of the number of pathogenic mutations to the number of benign mutations for a specific amino acid throughout the proteome.

(E) Apparent diffusion coefficient for HaloTag-Ser5 and HaloTag-Cys5 in cells treated with normal or pathogenic insulin. HaloTag-Ser5 normal n = 710 molecules, HaloTag-Ser5 pathogenic n = 747 molecules; HaloTag-Cys5 normal n = 1,239 molecules, HaloTag-Cys5 pathogenic n = 569 molecules. Mann-Whitney test was used for statistical analysis. ** represents p value < 0.01 and *** represents p value < 0.001.

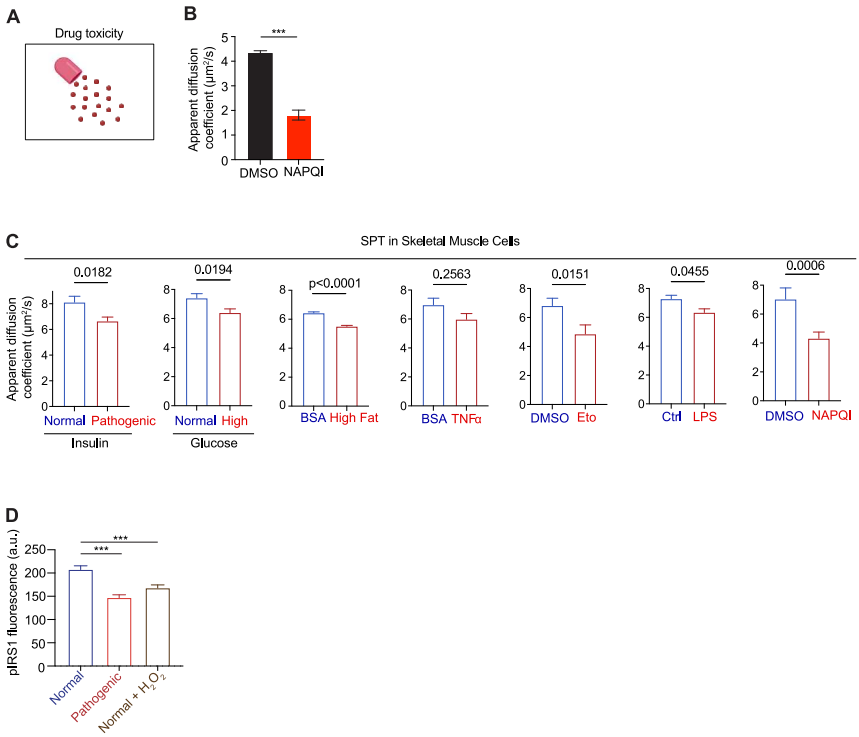

Figure S7. Pathogenic stimuli decrease protein mobility and function, related to Figures 5 and 6

(A) Cartoon depicting drug toxicity.

(B) Apparent diffusion coefficient, as determined by SPT, of the protein mobility biosensor expressed in HepG2 cells treated with (*N*-acetyl-*p*-benzoquinone imine [NAPQI], $n = 408$ protein molecules) and without (DMSO, $n = 4{,}921$ protein molecules) NAPQI. NAPQI is a toxic intermediate in the breakdown of acetaminophen and is one of the main causes of acetaminophen-induced liver injury. Data are plotted as mean ± SEM. Mann-Whitney was used for statistical analysis. *** represents p value < 0.001.

(C) Apparent diffusion coefficient, as determined by SPT, of the protein mobility biosensor expressed in C2C12 skeletal muscle cells treated with the stimuli reported in the figure. Data are plotted as mean + SEM. Mann-Whitney test was used for statistical analysis. Numbers of molecules: normal insulin (327) vs. pathogenic insulin (510); normal glucose (706) vs. high glucose (673); BSA (42,133) vs. high fat (38,486); BSA (294) vs. TNF-α (291); DMSO (186) vs. ETO (91); control (1,015) vs. LPS (777); control (75) vs. NAPQI (156). p values are reported in the figure.

(D) Quantification of phosphorylated IRS1 (pIRS1) levels by immunofluorescence in HepG2 cells treated with normal insulin (normal, 48 cytoplasmic regions), pathogenic insulin (pathogenic, 48 cytoplasmic regions) or normal insulin and H_2O_2 (normal + H_2O_2, 39 cytoplasmic regions). Results are represented as mean + SEM. t test was used for statistical analysis. *** represents p value < 0.001.